DEVELOPMENT OF MODIFIED TiO_2 NANOSTRUCTURES FOR PHOTOCATALYSIS

UNIVERSITY of the
WESTERN CAPE

Faculty of Natural Science

Department of Chemistry

By

Nzaliseko Mashiya

Supervisor: Prof. Lindiwe Khotseng

Co-supervisor: Prof. Emmanuel Iwuoha

DECLARATION

I hereby declare that I am the original author of "Development of modified TiO_2 nanostructures for photocatalysis" is my own work.

To the best of the researcher's knowledge, this study has not been published or presented at any other examination office in any university, and that all sources I have used and quoted have been indicated and acknowledged by complete references.

Full name: Nzaliseko Mashiya

Place: University of the Western Cape

Date: 7 December 2017

Signature:……

DEDICATION

I would like to dedicate my master's degree to my son, **Lethabo Uthandolwenkosi Mbuthuma**. May you grow to be a God fearing man!

ACKNOWLEDGEMENTS

I take this opportunity to thank the **Lord** of Israel, for giving the strength and the courage to complete my studies through difficult times. I would like to appreciate my supervisor, **Prof. Khotseng** for her guidance and patience she has shown towards my project. I would also like to thank my co-supervisor, **Prof. Iwuoha** for his time and assistance.

A special thank you to my parents and family for the encouragement and support, friends for being with me in difficult times: **Nkazimlo Feketshane, Noniko Nqakala** and Penny Mathumba.

To the love of my life , **Lebohang Mbuthuma**. Thank you for always believing in me.

Thank you to all the members of the Electrocatalysis Research Laboratory for sharing wisdom with me.

I would like to thank the University of Western Cape and the Chemistry Department, for believing in me and giving me the opportunity to conduct my research at the institution.

I would also like to thank the National Research Foundation for financial assistance throughout the course of this project.

ABSTRACT

TiO_2 has been broadly used as a standard photocatalyst due to its high stability, low cost, relatively low toxicity, and excellent photocatalytic performance in comparison to other semiconductor materials. However, the large band gap of TiO_2 limits its use as a photocalyst due to the high energy required for excitation of the electrons in the UV region. Research on the reduction of TiO_2 band gap to the visible region of the spectrum has been explored with little success. Therefore, this study focusses on shifting the band gap of TiO_2 catalyst from the UV region to the visible region by doping with graphene and nitrogen-doped graphene to form TiO_2-G and TiO_2-NG nanocomposites, respectively. The N-doped graphene support was prepared by doping the graphene oxide with nitrogen through Hydrothermal process, followed by the reduction of the materials.

Fourier Tranform Infrared (FTIR) spectroscopy confirmed the successful doping of graphene to N-graphene by the appearance of C-N and N-H vibrational modes on the spectra. The XRD results show the fingerprint patterns of TiO_2 and N-graphene, which confirms the successful preparation of the nanocomposites. Morphological studies of the nanocomposites using transmission electron microscopy (TEM) show the TiO_2 nanowires dispersed on graphene related supports. The optical band gap of TiO2 from UV-Vis spectroscopy was found to be 3.2eV, which decreased to 2.7eV and 2.5eV upon incorporation of grapheme and N-graphene, respectively. These results prove the success in the achievement of the aim in this study. When electrochemical studies were further conducted on the materials, TiO_2-NG was found to possess better electrochemical properties with fast electron kinetics observed on the impendance spectroscopy results. The results obtained justified use of TiO_2-NG photocatalyst the optimal material for organic mineralisation in Advanced Oxidation Processes (AOPs).

TABLE OF CONTENTS

CONTENT **PAGE**

LIST OF FIGURES

LIST OF TABLES

LIST OF ABBREVIATIONS

TiO_2	Titanium dioxide
XRD	X-Ray Diffraction
CO_2	Carbon dioxide
FTIR	Fourier-transform infrared spectroscopy
SEM	Scanning Electron Microscope
TEM	Transmission Electron Microscope
CV	Cyclic Voltammetry
UV-Vis	UV-Visible Spectrophotometer
AOP	Advanced Oxidation Processes
POPs	Persistent Organic Pollutants
DDT	Dichlorodiphenyltrichloroethane
HCB	Hexachlorobenzene
PCBs	Polychlorinated biphenyl
PCDDs	Polychlorinated dibenzo-*p*-dioxins
PCDFs	Polychlorinated dibenzofurans

CHAPTER ONE

SYNOPSIS

This chapter gives an overview of the water crisis that we are currently facing in the world, and the health challenges it possess to humans and the nature. The chapter emphasises the need for an improved water system treatment method, as current methods are not efficient in degrading organic pollutants. The problem statement, aims and objectives of the research are presented, as well as the research approach. And finally, a presentation of the thesis outline concludes the chapter.

1.1 Background and Motivation

The total amount of water on earth is constant; it cannot be increased or decreased, but unevenly distributed across earth (1). Water is one of the most important resources available for life on earth. The National Aeronautics and Space Administration (NASA) states, every living organism on earth relies on water for survival, from the smallest microorganism to the largest mammal (2). Water is distributed unevenly across the continents of the earth, exposing some countries to limited available fresh water. A report by the World Wildlife Fund (WWF) shows that Africa is the second driest continent, after Australia. It is estimated that more than 300 million people in Africa live in water scarce environments, with the amount of freshwater available for each person being about one-quarter of what it was in 1950 (3).

The situation is worsening as a consequence of rapid urbanization, population growth, agriculture activities and the lack of adequate capacity to manage freshwater resources. By the year 2025, 18 African countries are expected to experience water stress, effects which are already evident in South Africa. In March 2018, the Western Cape's dam levels were standing at an average of 32 percent with 10 percent being unusable due to its poor quality (4, 5). There have been claims that community members in Cape Town were exposed to unsafe water in the year 2017, even though the mayoral committee member for informal settlements Xanthea Limberg assured residents that water quality is closely monitored according to the stringent SA National Standards requirements (6).

Professor Neil Armitage, head of department at Urban Water Management, University of Cape Town, said although levels are low, the treatment works ensure water remains safe for drinking. However, he confirms that it is true that the city's drinking water is often slightly coloured brown as a result of the turn-over of the water in the reservoirs due to seasonal changes. The water inverts itself as the surface water cools down and sinks, while the cooler water near the bottom of the reservoirs rises to the surface carrying waster matter from the sediments (6).

Human and natural activities have decreased the quality of fresh water through an increase in pollution in water systems, which range from domestic effluent waste to pollution caused by water erosions. Water quality is the measurement of water which is safe and appealing to all life on earth; the water should be free of disease-causing organisms and stable in terms of corrosion and water hardness (7). The effects of polluted water are disastrous on the aquatic ecosystems, agriculture and human health. Researchers have reported incidents of mass poising in pregnant women which have adverse effects of development disorders, due to exposure to certain Persistent Organic Pollutants (POPs). Studies on the effects of POPs on wildlife have indicated embryo alterations in birds and reproductive impairments and malformations in mammals (8).

Under the Stockholm Convention, countries around the world have agreed to eliminate the production of twelve key POPs, as they have unforeseen effects on the environment. Due to their persistence and low volatility, they can be transported across the world in low concentrations through water and air movements, affecting human and environmental health globally (9). Organic pollutants originate from domestic sewage, urban run-offs, industrial effluents and agriculture wastewater. These pollutants include pesticides, fertilizers, hydrocarbons, phenols, plasticizers, biphenyls, detergents, oils, greases, pharmaceuticals, proteins and carbohydrates (10).

The negative environmental impacts related to organic pollution have shifted the interest of the research into seeking an efficient method for the removal of toxic organic compounds from water systems. Traditional treatment methods have proven to be effective for many pollutants, however such methods have limitations when mineralizing organic pollutants, which necessitate the development of an innovative and more efficient water treatment process. Advanced oxidation processes (AOPs) represent an alternative water treatment option to air stripping, granular activated carbon adsorption (GAC), and resin sorption. Air stripping and sorption are phase-

transfer processes in which organic contaminants are physically transferred to a gas phase and solid phase, respectively. For these methods, the actual destruction of pollutants requires additional processes, such as thermal or catalytic oxidation. In contrast, AOP destroy primary organic contaminants directly in water through chemical reactions and offers a higher degree of process ability to degrade pollutants at concentration levels that can be challenging for conventional methods (11, 12).

AOP processes assists in the photocatalysis degradation of organic environmental pollutants in the presence of a semiconductor catalyst. Photocatalysis is classified into two categories of homogeneous and heterogeneous process. Homogeneous photocatalysis processes are used with metal complexes as catalysts with the higher oxidation state of the metal ion complexes generating hydroxyl radicals. The radicals react with organic matter, destructing the toxic matters. On the other hand heterogeneous makes use of semiconducting materials, such as TiO_2, ZnO, CeO_2 and SnO_2. Theses semiconductors are used photocatalysts due to their favorable combination of electronic structures, which are characterized by a filled valence band and an empty conduction band, charge transport characteristics, excited states lifetime and light adsorption properties (13, 14).

As an environmentally friendly process, AOPs have considerable advantages over some existing technology; it mineralizes organic pollutants into CO_2 and H_2O using TiO_2 as the suitable photocatalyst, rather than transferring them to another phase, it is also able to destroy pollutants without the use of hazardous oxidants. It is stable in a wide range of pH and it is able to couple with other water treatment for better productivity. Despite the advantages of AOPs, several limitations are present in their usage, these include harmful intermediates that may be formed, pre-treatment of wastewater may be required for minimal cleaning and maintenance of a UV reactor, due to energy requirements cost is higher and it has major challenges of catalyst deactivation, slow kinetics, unpredictable mechanism and low photo-efficiency. With all the drawbacks considered AOPs are still more effective than other wastewater treatment techniques (13, 14).

1.1 Problem statement

The quality of drinking water is a powerful environmental determinant of health. Conventional water treatment methods, such as chlorination, have disadvantages such as handling of hazardous chemicals and producing by-products. Titanium dioxide is a good photocatalyst for the degradation of organic pollutants, however it has many drawbacks. The challenges faced by the application of TiO_2 as a photocatalyst are as a result of its narrow photocatalytic region (UV-Vis), which is excited at a wavelength of energy less than 400 nm. Furthermore TiO_2 absorbs less than 5% of incident solar irradiation light, this is due to the large band gap of anatase, which is about 3.2 eV. In addition to the challenges, TiO_2 has slow photocatalytic rates caused by the low adsorption of organic pollutants on its surface. Since photocatalytic degradation occurs mainly on the surface of TiO_2, the adsorptivity has to be increased for effective application of TiO_2 in water treatment. Graphene provides improved electronic and photonic properties, which makes it an ultimate candidate material for enhancing the photo-reactivity of TiO_2.

1.2 Aims and Objectives

The aim of the research was to modify the wavelength of TiO_2 by preparing nanocomposites of Graphene-TiO_2 to enhance the photocatalytic degradation of organic pollutants. Achievement of the aim allows for understanding of the physical and chemical nature of the nanocomposite and how they improve the purification of wastewater.

The objective of this study was to investigate the influence of the support material on the photocatalyst whilst simultaneously determining the support material that will enhance the activity of the catalyst between graphene and nitrogen doped graphene in the applications photocatalysis.

The aim was achieved through the following objectives:

- Synthesis of reduced graphene oxide using the modified Hummer's method.
- Synthesis of reduced N-graphene oxide using the modified Hummer's method.
- Synthesis of TiO_2 nanowires using hydrothermal approach and the microwave process.
- Synthesis of TiO_2 nanowires supported on reduced n-graphene oxide nanowires.

- Physical, chemical and electrochemical characterisation of the synthesised nanocomposites.

1.3 Research Questions

The questions that are addressed by this research are:

- Will N-graphene serve as a great support to increase the band gap of TiO_2 for photocatalytic degradation than graphene?
- Will the supported TiO_2 nanowires be effective for photocatalytic activity?
- Will TiO_2 nanowires perform better than TiO_2 nanoparticles in the advanced Oxidation process?
- Does the integration of TiO_2 with graphene and N-graphene improve the effectiveness of photocatalysis?

1.4 Research Approach

The research project focused on the synthesis, characterisation of TiO_2 nanowires supported on graphene for photocatalytic degradation of organic pollutants. The study focuses on the production of OH radicals to remove traceable organic contaminates. The aims and objectives of this study will be achieved by preparing nitrogen doped graphene using the modified hummer's method and the microwave process. The TiO_2 nanowires will be prepared using the hydrothermal method and the microwave process, various characterisation techniques will be used to study the physical and chemical properties of the prepared materials, these include electrochemical characterization to study their behaviour (cyclic voltammetry, electrochemical impedance spectroscopy and chronopotentiometry) and UV, XRD, SEM and TEM to confirm the success of the formation of the nanocomposites while understanding the morphological structures of the materials and their crystallinity properties.

Thesis Outline

The current study consists of four more chapters presented as follows:

Chapter Two: This chapter presents the literature review on photocatalysis as a treatment method for removal of organic compounds using an advanced oxidation process, examples of persistent organic pollutants as well as the application and limitations of the treatment method are underlined.

Chapter Three: This chapter outlines the experimental approaches, analytical techniques and sampling methods used in this research work.

Chapter Four: The results obtained from characterization and application of Titania supported on graphene nanocomposites during photocatalysis are discussed in this chapter.

Chapter Five: This chapter states the conclusions and recommendations of this study.

CHAPTER TWO

LITERATURE REVIEW

2 INTRODUCTION

This chapter covers the literature review on persistent organic pollutants and different treatment methods used for water purification. It focuses on the review of the photocatalysis of organic pollutants, with TiO_2 as the photocatalyst. The properties of the graphene support in enhancing the photocatalytic productivity of TiO_2 are also reviewed, alongside its composites.

2.1 Water Pollution

The term ‘pollution’ is often used, but seldom defined. A search in literature reveals that it is often used synonymously with the term ‘contamination’. The United States Environmental Protection Agency (US EPA) defines pollution as the presence of a substance in the environment that prevents the functioning of natural processes and produces undesirable environmental and health effects. The US EPA also gives a definition of the term contamination as the introduction of microorganisms, chemicals, toxic substances, wastes and wastewater in a concentration that makes the medium unfit for its intended use (15, 16).

Chemical water pollution is considered to be the most harmful type of pollution to nature, this includes pollutants from inorganic and organic sources. Inorganic pollutants are pollutants that are naturally found in the environment but end up in water systems due to human activities; these include inorganic salts, trace elements, metal compounds and mineral acids. Organic pollution occurs when there are dissolved concentrations of organic substances from pathogens, nutrients, synthetic organic compounds and oil in water systems. Pollutants enter water systems through point sources and nonpoint sources (17, 18).

Point source pollutants are, compared to nonpoint source pollutants, characteristically easier to control, more readily identifiable and measurable, while they are more toxic. Nonpoint sources of pollution are the consequence of agricultural activities such as irrigation and drainage, runoff and erosion. Point sources amongst others include hazardous spills, underground storage tanks,

and municipal waste outfalls. Compared to point source pollution, nonpoint source pollution is more difficult, related to monitoring and enforcement of mitigating controls, due to the heterogeneity of soil and water systems at large scales. Characteristically, nonpoint source pollutants are difficult to trace to a source, they enter the environment over an extensive area, they can be related to certain uncontrollable meteorological events and existing geographic conditions and have the potential for maintaining a relatively long active presence on the global ecosystem, which may result in long term chronic effects on human health and cause soil degradation (17, 19).

2.1.1 Persistent Organic Pollutants

The term persistent organic pollutants refers to a broad range of anthropogenic compounds present in the environment, these compounds resist photolytic, chemical and biological degradation. They are characterized by low water solubility and high lipid solubility, which result in the occurrence of POPs all over the world, even in regions where they have never been used before. POPs have been found on a global scale in soils, in the fat of fish, terrestrial animals, as well as in human breast milk. These organic pollutants persist in the environment, accumulate through the food chain and cause adverse effects to human health and the environment. (20,21)

Laboratory and field-based studies have recorded human health effects such as allergies, hypersensitivity, nervous system damage, reproductive and immune dysfunction, from exposure to the organic pollutants. Hormone system dysfunction with exposure to POPs includes damage to the reproductive system, sex- linked disorders and shortened lactation periods for nursing mothers. Many POPs are considered human carcinogens by the International Agency for Research on Cancer (IARC). With the evidence of long-range transport of these substances, the international community has called for urgent global actions to reduce and eliminate the releases of these chemicals through the Stockholm Convention (21, 22, 23).

The Stockholm Convention on POPs commits to take measures to reduce and eliminate emission of POPs as well as their by-products. The Stockholm Convention on POPs is a global ratified agreement with the aim to protect humans and the environment from adverse effects from POPs. South Africa has used and in many cases produced these chemicals and our environment and population have and are being exposed to their effects. In line with the county's commitment to

sustainable development, South Africa has joined the international communities' efforts to phase out these chemicals by becoming a part in the Stockholm Convention (24).

Under the Convention twelve chlorinated chemical substances have been severely restricted following a strict criteria. The criteria involves monitoring the persistence of the chemical, the chemical must have half-life that is greater than 2 months in water and more than 6 months in soil or sediments. The bioconcentration factor in aquatic species should be greater than 5,000, which indicate potential for bioaccumulation. There must be measured levels of the chemical in locations distant from the sources of its release; for chemicals that migrate through the air, its half-time should be greater than 2 days. Adverse effects to human health and the environment must be monitored to justify the consideration of the chemical within the scope of the Convention. The twelve POPs restricted by the Stockholm Convention includes dioxins, furans, polychlorinated biphenyls (PCBs), hexachlorobenzene (HCB) and several organochlorines used as pesticides (22, 23, 24).

2.1.1.1 Twelve Persistent Organic Pollutants

a) Aldrin and Dieldrin

Aldrin and Dieldrin are highly effective insecticides for soil-dwelling pests and for the protection of wooden structures against termites and wood borers. Aldrin and fieldrin were first formulated from a waste product of synthetic rubber, clyclopen-tadiene. Aldrin and dieldrin were designated as persistent organic pollutants in 1997 by the Governing Council of the United Nations Environment Programme .Although the use of aldrin and dieldrin has been severely restricted in many parts of the world, these insecticides are still used in termite control in some countries (25,26).

The reduction in use of these insecticides since the 1970s has decreased the residues in food in many countries below the danger levels. The concentration of aldrin and dieldrin in aquatic environments and drinking-water is not more than 10 mg/litre. Higher levels are attributed to contamination from industrial effluents and soil erosion during agricultural use. Dieldrin has been detected at very low concentrations in ambient air, on dust particles and in rainwater. In non-agricultural areas, concentrations of 0.06–1.6 ng/m^3 have been reported (26, 27, 28).

In soil, aldrin is removed by oxidation to dieldrin and by evaporation. In temperate climates, only 75% is oxidized within a year after application. The further disappearance of dieldrin is very slow under these conditions; the half-life is approximately 5 years. Under tropical conditions, both oxidation and further disappearance of dieldrin are rapid, 90% disappearing within 1 month, primarily by volatilization (27, 28).

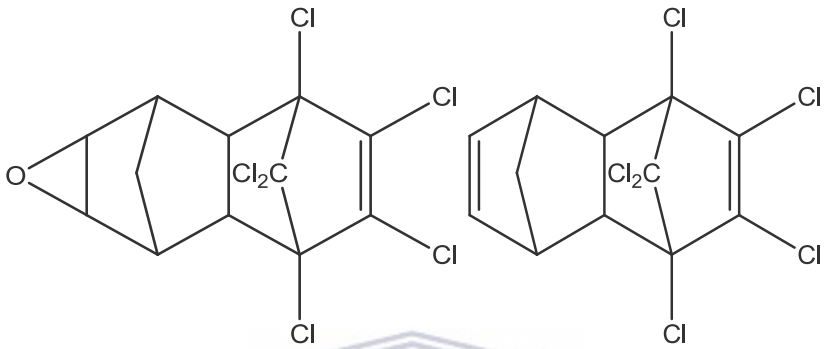

Figure 2.1: Chemical structure of Adlrin and Dieldrin (27).

b) Chlordane

Chlordane is a versatile, broad-spectrum insecticide used mainly for non-agricultural purposes. It is also used on corn, potatoes and on livestock. When used for termite control, it is applied to the soil by subsurface injection. The use of chlordane has been increasingly restricted in many countries. Chlordane is very resistant to chemical and biological degradation. It is highly immobile and migrates very poorly. In spite of its very low mobility in soil, chlordane may be a low-level source of contamination in groundwater when applied by subsurface injection. Once in water bodies, it is not removed by photodegradation, hydrolysis or biodegradation (29, 30).

Chlordane levels range from less than 0.1 to 60 ng/m^3 in urban air and from 0.01 to 1 ng/m^3 in rural air. Chlordane contaminates indoor air when used for termite control, levels of chlordane exceeding 1 μg/m^3 have been measured in the air. Chlordane is rarely detected in drinking-water; when found, it is mainly at levels below 0.1 μg/l . Levels of chlordane in drinking-water and groundwater that are higher than its solubility have been reported. Chlordane has been found in meat, eggs and milk. Some chlordane metabolites have been found in human milk. Food is considered to be the major source of exposure of the general population to chlordane (29, 30).

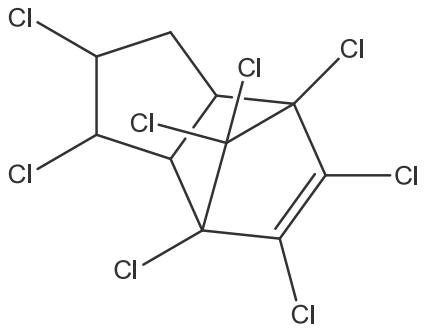

Figure 2.2: Chemical structure of Chlordane (29).

c) Dichlorodiphenyltrichloroethane

Dichlorodiphenyltrichloroethane (DDT) is a non-synthetic contact insecticide which was widely used to control insects on agricultural crops that carry diseases such as typhus, malaria and dengue fever. However, the use of this compound has been banned in many countries since 1970s because of its chemical characteristics such as accumulation and bio-concentration in lipid systems of animal species which may result in occurrence of potential adverse effects on animals and eventually humans. The physical and chemical properties of DDT and its metabolites enable these compounds to be taken up readily by organisms from the surrounding medium and from food. High lipid solubility and low water solubility lead to the retention of DDT and its stable metabolites in fatty tissue (31, 32).

DDT and its metabolite are toxic to a range of wildlife animals including birds and aquatic animals, these compounds causes egg shell thinning of certain bird species leading to declines in their populations. Despite these circumstances, DDT is still used in the certain areas of tropics and subtropics for the control of malaria and other insect-transmitted diseases causing high death rates. In 2006, World Health Organization (WHO) permitted the use of DDT in those areas to reduce the rate of deaths caused by malaria (31, 32).

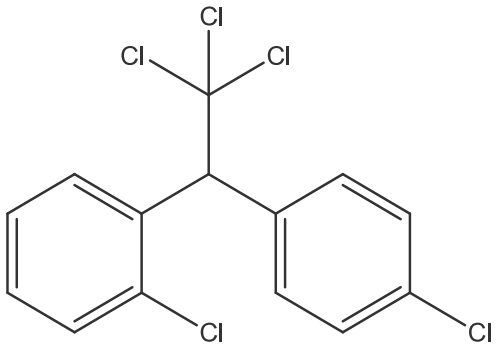

Figure 2.3: Chemical structure of Dichlorodiphenyltrichloroethane (31).

d) Endrin

Endrin is a foliar insecticide that acts against a wide range of agricultural pests. It has a broad spectrum which is particularly effective against Lepidoptera. It is used mainly on cotton and against pests of rice, sugar-cane, maize and other crops, while also being used as a rodenticide. Endrin is highly toxic to fish, when exposed to high levels of endrin in water their eggs hatch early and die from the exposure (33).

The mechanisms by which endrin is removed from the environment include photodecomposition and bacterial degradation. In the presence of sunlight, the ketone δ-ketoendrin is the main product formed. Microbial degradation of endrin depends on the presence of an appropriate microbial species and suitable soil conditions, the degradation occurs under anaerobic conditions. Biodegradation is aided by fungi and bacteria, and the major transformation product is the δ-ketoendrin (33).

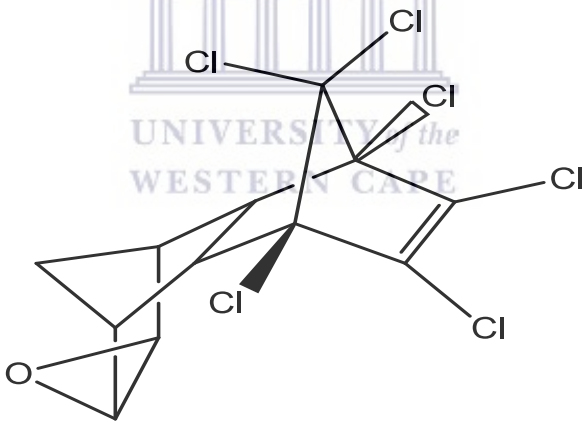

Figure 2.4: Chemical structure of Endrin (33).

e) Heptachlor

Heptachlor is a chlorinated dicyclopentadiene insecticide that is persistent in the environment and accumulates in the food-chain. It is applied as a soil treatment and as a seed treatment method. It is used to control ants, cutworms, maggots, termites, thrips, weevils, wireworms and other insect pests in both cultivated and uncultivated soils. Heptachlor also controls household insects and pests domestic animals. Although its use has been severely restricted in many countries since the 1980s, it is still detected as a contaminant in some food sources. This is due to

its persistence, but it also suggests the illegal use of this pesticide in the recent past or present (34, 35)

Heptachlor released into the environment can be transformed by abiotic processes, such as the transformation by photochemically produced hydroxyl radicals, and it is transformed in the presence of water to compounds such as 1-hydroxychlordene or heptachlor epoxide in moist soils. In addition, it can be removed from aquatic systems by evaporation and has a limited potential to leach from soil into groundwater due to its elevated soil sorption coefficient. It is not readily biodegraded, but it is transformed biologically by bacteria, fungi, plants and animals, to the stable heptachlor epoxide (34, 35).

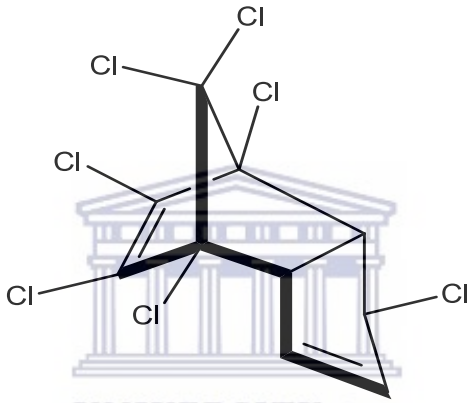

Figure 2.5: Chemical structure of Heptachlor (34).

f) Hexachlorobenzene

Hexachlorobenzene (HCB) had many uses in agriculture; the major agricultural application for HCB used to be as a seed dressing for crops such as wheat, barley, oats and rye to prevent growth of fungi. The use of HCB in such applications was discontinued in many countries in the 1970s owing to concerns about adverse effects on the environment and human health. However, HCB is still used for this purpose in some countries. At present, its main significance appears to be as a by-product of several chemical processes or an impurity in some pesticides (36, 37).

HCB is distributed throughout the environment due to its mobility and resistance to degradation. The bioaccumulative properties of HCB result from the combination of its physicochemical properties and its slow elimination due to limited metabolism related to its high chemical stability (36, 37).

Total intake of HCB from ambient air, drinking-water and foods is estimated to range from approximately 0.0004 to 0.003 μg/kg of body weight per day for the general population, the principal route of exposure being through the diet (92%). The estimated contributions from air and drinking-water are much smaller; 7% and 1%, respectively. The results of most studies of temporal trends of HCB levels in human adipose tissue or milk indicate that general population exposures have declined since the 1970s (36, 37).

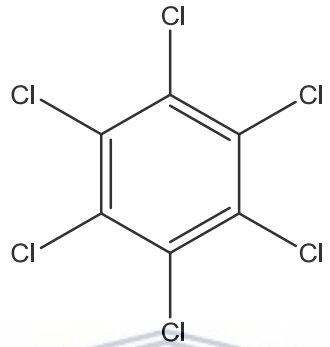

Figure 2.6: Chemical structure of Hexachlorobenzene (36).

g) Mirex

Mirex is a very persistent compound in the environment that is highly resistant to both chemical and biological degradation. The primary process for the degradation of mirex is photolysis in water or on soil surfaces, with photomirex being the major transformation product of photolysis. In soil, anaerobic biodegradation is a major removal mechanism where mirex is slowly dechlorinated to the lo-monohydro derivative. Aerobic biodegradation on soil is a very slow and minor degradation process (38, 39).

Adsorption and volatilization are the more important environmental fate processes for mirex, which strongly binds to organic matter in water, sediment, and soil. When bound to organic-rich soil, mirex is highly immobile; however, when adsorbed to particulate matter in water it can be transported great distances before partitioning out to sediment. Atmospheric transport of mirex has been reported based on its detection in remote areas without anthropogenic sources. Given the lipophilic nature of this compound of high octanol-water partition coefficient, mirex is both bioaccumulated and biomagnified in aquatic and terrestrial food chains (38, 39).

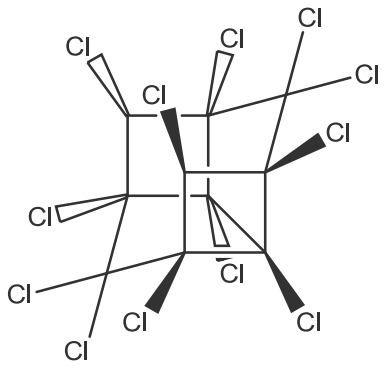

Figure 2.7: Chemical structure of Mirex (38).

h) Toxaphene

Toxaphene was used as pesticides to control insect pests on cotton and other crops, it was also used in controlling insect pests on livestock and killing unwanted fish in lakes. When toxaphene is released to the environment it can enter the air by evaporation, the soil by sticking to the soil particles and water from runoff after rain. Toxaphene does not dissolve well in water, it is more likely to be found in air and soil. Toxaphene levels may be high in some predatory fish and mammals because toxaphene accumulates in fatty tissues of animals (40, 41).

Toxaphene is a reproducible mixture of polychlorinated camphenes and comprises more than 180 components. The major part of technical toxaphene consists of chlorinated bornanes. Toxaphene is poorly soluble in water and moderately volatile. It has a log K_{ow} of 3.2 - 6.6, and adsorbs strongly to suspended sediments, with a log K_{oc} of 3.2 - 5.3. Toxaphene has a high bioaccumulation potential. Toxaphene is persistent, degradation by hydrolysis and photolysis is negligible, and biodegradation is slow. The persistent character combined with a moderate volatility and poor water solubility result in long-range atmospheric transport being a major dispersion mechanism for toxaphene. Volatilisation in warmer regions and deposition in colder regions may occur (40, 41).

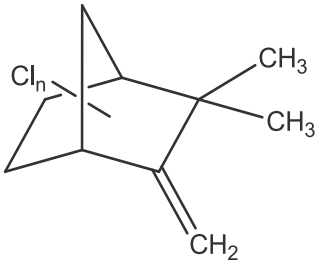

Figure 2.8: Chemical structure of Toxaphene (40).

i) Polychlorinated biphenyl

Polychlorinated biphenyl (PCBs) are synthetic chlorinated hydrocarbon compounds that have been produced commercially since 1929. They have been used in plasticizers, surface coatings, inks, adhesives, flame retardants, pesticide extenders, paints, and microencapsulation of dyes for carbonless duplicating paper. They have also been used in dielectric fluids in transformers and capacitor because they resist both acids and alkalis and are relatively heat-stable. Further environmental contamination may occur from the disposal of old electrical equipment containing PCBs. The pyrolysis of PCB mixtures produces hydrogen chloride and polychlorinated dibenzofurans (PCDFs), and pyrolysis of mixtures containing chlorobenzenes also produces polychlorinated dibenzodioxins (PCDDs). Many countries have severely restricted or banned the production of PCBs (42, 43).

Highly chlorinated PCB substances adsorb strongly to soil and sediment and are generally persistent in the environment. The various substances in soil and sediment have half-lives that extend from months to years. Adsorption of PCBs generally increases with the extent of chlorination of the substances and with the organic carbon and clay contents of the soil or sediment. Volatilization and biodegradation are two very slow processes that are the major pathways of PCB removal from water and soil (42,43).

PCBs accumulate in the food-chain. They are rapidly absorbed from the gastrointestinal tract and distribute to and accumulate in the liver and adipose tissue. They also cross the placenta, are excreted in milk, and accumulate in the fetus/infant. PCBs are metabolized by hydroxylation and subsequent conjugation. The rates of metabolism and subsequent excretion vary markedly between different substances (42, 43).

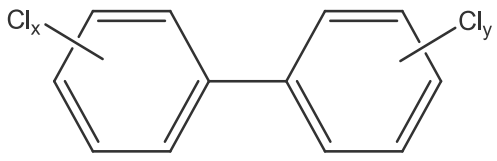

Figure 2.9: Chemical structure of Polychlororinated biphenyls (42).

j) Polychlorinated dibenzo-*p*-dioxins and Polychlorinated dibenzofurans

Polychlorinated dibenzo-*p*-dioxins (PCDDs) and Polychlorinated dibenzofurans (PCDFs) are not commercially produced but are formed as trace amounts of undesired impurities in the manufacture of other chemicals, such as chlorinated phenols and their derivatives, chlorinated diphenyl ethers and polychlorinated biphenyls (PCBs). Earlier use of pentachlorophenol is considered to be a major source of PCDDs and PCDFs in many industrialized countries. PCDDs and PCDFs are also formed in combustion (44, 45).

Chlorine bleaching of pulp and paper has also been an important source and low concentrations of PCDDs and PCDFs. Chlorine-alkali plants using graphite electrodes have been identified as a point source, and car exhausts, mainly exhausts from leaded petrol in which chlorinated solvents have been used as so-called "scavengers", also produce these compounds. Although a variety of sources of PCDDs and PCDFs have been identified, including sewage sludge and garden composts, in which they are formed naturally, there may well be a substantial fraction that originates from unidentified sources. There is no known technical use for PCDDs and PCDFs (44, 45).

WHO concluded that intake of PCDDs and PCDFs through drinking water is negligible (32). The limited data available indicated TEQ levels of 0.003 pg/litre, which could result in a daily TEQ intake of less than 0.005 pg/person, assuming an average daily water intake of 1.5 litres/day (44, 45, 46).

It is generally agreed that the general population currently receives its major exposure to PCDDs and PCDFs through the intake of food. Since PCDDs and PCDFs are lipophilic and accumulate in the food-chain, food of animal origin is the most important source. In general, plants contain only low levels of PCDDs and PCDFs, commonly close to the detection levels for these chemicals (44, 45, 46).

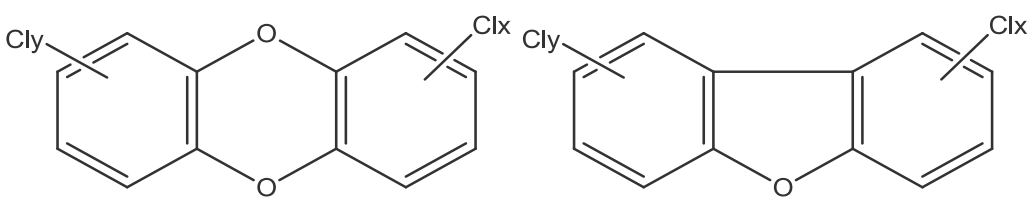

Figure 2.10: Chemical structure of PCDDs and PCDFs (44).

2.2 TREATMENT METHODS

Large amounts of POPs are contributing to environmental pollution around the world. Bioremediation is one of the methods commonly used for POPs treatment. Bioremediation is a relatively efficient and cost effective method that involves the usage of microorganism in treating POPs. It is selected as an option for treating POPs because of the ubiquitous nature of microorganism, ability to work in extreme conditions, effective catalytic mechanism and wide diversity. However, there are some limitations in using bioremediation such as poor capabilities of microbial, lesser bioavailability of contaminants on temporal and spatial scales, and lack of bench-mark values for efficacy testing of bioremediation (47 , 48).

The continuous release of POPs into the environment has raised a need to come out with effective treatment method. Coagulation and flocculation process is widely used for treating POPs in wastewater due to its simple operation. Coagulation and flocculation processes are very effective for removing high concentration of organic pollutants. Coagulant destabilizes the colloidal particles in coagulation process. Then it is followed by flocculation process which increase the unstable particle size into larger flocs and encourage flocs formation. This process enables the removal of colloid particles and suspended solids from the solution. Aluminium sulphate (Alum) is a commonly used inorganic salt for treating wastewater. Alum is chosen for treating organic contaminants due to the low cost involved and easily available. However, alum is not environmental friendly as it produces large amount of sludge that is toxic. Advanced oxidation processes have proven to be the most promising treatment method available for persistent organic pollutants (49, 50).

2.2.1 ADVANCED OXIDATION PROCESS

Advanced oxidation processes have been defined as water treatment processes that involve an input of energy into the water system to produce highly reactive radical intermediates, which then attacks and destroys the target compounds. Most advanced oxidation processes for water and wastewater treatment are based on the generation of hydroxyl radicals to initiate an oxidation reaction. (AOPs). The suitability of AOPs for aqueous pollutant degradation was recognized in the early 1970s and much research and development work has been undertaken to commercialize some of these processes. **Figure 2.11** shows the different types of AOPs. (51)

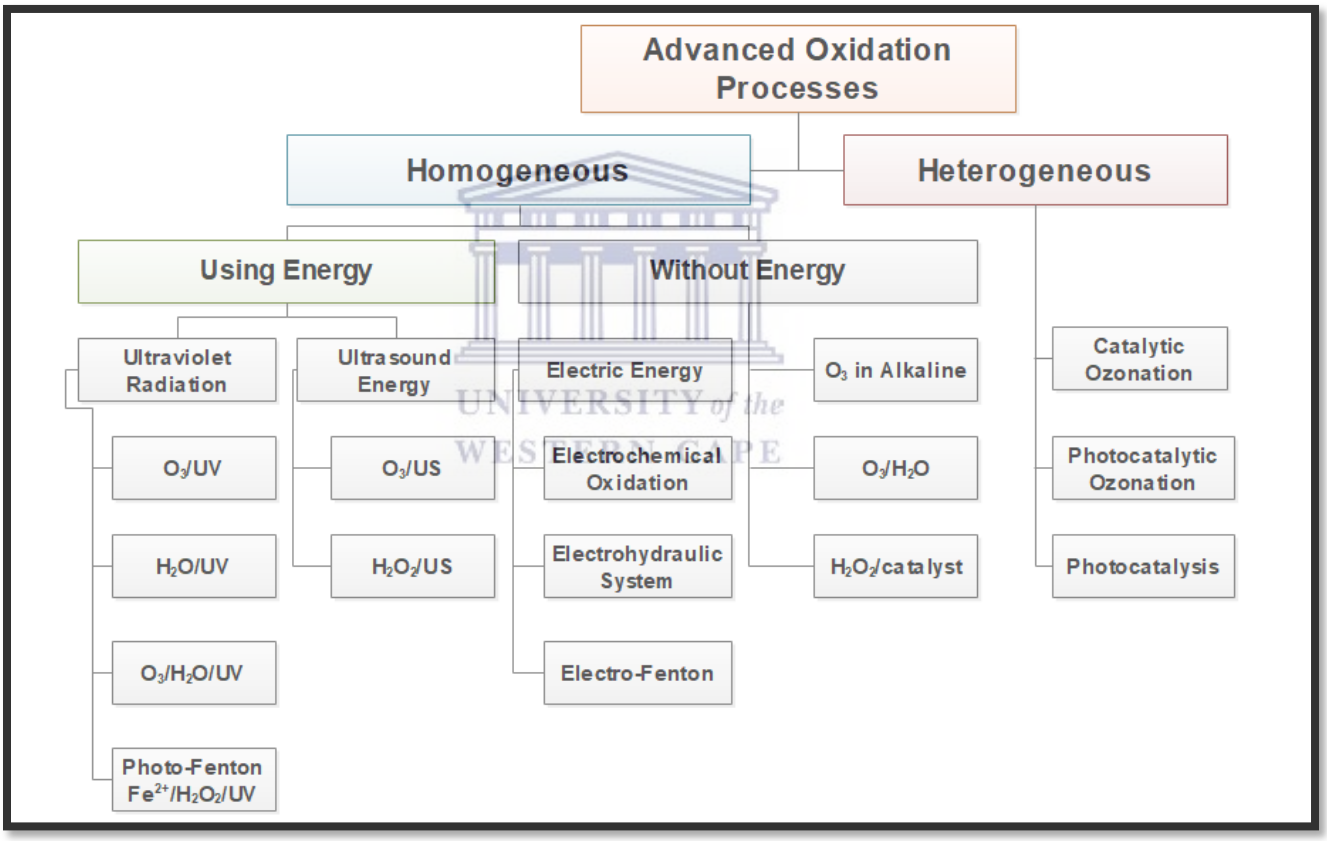

Figure2.11: Various advanced oxidation processes based on water treatment technology (52).

2.2.1.1 UV/O_3 PROCESS

The ultraviolet/Ozone process (UV/O_3) UV/O_3 is a homogeneous advanced oxidation process that utilizes energy. There are three dominant reactions during the ultraviolet (UV)/Ozone (O_3) treatment processes which effectively decompose organic pollutants, namely: photolysis, ozonation, and hydroxyl radical reactions. The generation of hydroxyl radicals is an essential, transitional reaction that ultimately destroys organic pollutants during the oxidation process. The advanced oxidation process with UV radiation and ozone is initiated by the photolysis of ozone. This process is preceded by the generation of two hydroxyl radicals, which, if they do not react, recombine to produce the hydrogen peroxide, as shown in **Equations (2.1), (2.2)** and **(2.3)**.The UV/O_3 process produces hydroxyl radicals, hydrogen peroxide and oxidizes the pollutants (52,53).

$$O_{3(g)} + hv \rightarrow O_{2(g)} + O^{\cdot}_{(aq)} \quad (2.1)$$

$$O_{3(g)} + H_2O_{(l)} \rightarrow 2OH^{\cdot}_{(aq)} \rightarrow H_2O_{2(aq)} \quad (2.2)$$

$$O^{\cdot}_{(aq)} + H_2O_{(l)} \rightarrow H_2O_{2(aq)} \quad (2.3)$$

2.2.1.2 H_2O_2 OXIDATION PROCESS

The photolysis of H_2O_2 and Fenton's reaction are the most commonly used ways for generation of hydroxyl radicals from hydrogen peroxide. The primary process of H_2O_2 photolysis in the 200-300 nm regions is dissociation of H_2O_2 to hydroxyl radicals with a quantum yield of two OH· radicals formed per quantum of radiation absorbed, as expressed by **Equations (2.4), (2.5)** and **(2.6)** (52,53, 54).

$$H_2O_2 + hv \rightarrow 2OH\cdot \quad (2.4)$$

$$OH\cdot + H_2O_2 \rightarrow H_2O + 2OH\cdot \quad (2.5)$$

$$\frac{1}{2}O_2\cdot + 2H_2O_2 \rightarrow O_2 + H_2O + 2OH\cdot \quad (2.6)$$

The Fenton-type catalysed generation of hydroxyl radicals is based on the decomposition of hydrogen peroxide by ferrous ions, which are shown in **Equation (2.7)**. This method is very effective for generating hydroxyl radicals, but involves consumption of one molecule of Fe^{2+} for each hydroxyl radical produced. The decomposition of hydrogen peroxide is also catalysed by ferric ions. In this process, H_2O_2 is decomposed to H_2O and O_2 and a steady-state concentration of ferrous ions is maintained during peroxide decomposition:

$$Fe^{2+} + H_2O_2 \rightarrow Fe^{3+} + OH^- + OH\cdot \quad (2.6)$$

$$Fe^{3+} + H_2O_2 \overset{-H^+}{\longleftrightarrow} Fe(OOH)^{2+} \leftrightarrow Fe^{2+} + HO_2\cdot \quad (2.7)$$

$$Fe^{3+} + HO_2\cdot \rightarrow Fe^{2+} + H^+ + O_2 \quad (2.8)$$

The ferric system, known as the Fenton-like reagent, is attractive, because degradation of organics can be catalytic over iron. However, the initial rate of destruction of organic pollutants by Fe (III)/H_2O_2 is much slower than that of the Fe (II)/H_2O_2 due to the lower reactivity of ferric ions toward hydrogen peroxide. The oxidizing power of the Fenton-type systems can be greatly enhanced by irradiation with UV-visible light due to the photo-reduction of hydroxylated ferric ion aqueous solution, as shown in **Equation 2.10** (52, 53, 54).

$$Fe^{3+} + OH^{-} \leftrightarrow Fe(OH)^{2+} \quad (2.9)$$

$$Fe(OH)^{2+} + h\nu \rightarrow Fe^{2+} + OH\cdot \quad (2.10)$$

The combined process, as shown in **Equation(2.7), (2.9)** and **(2.10)**, is known as the photo-Fenton reaction, and results in increased production of OH· radicals and more importantly, iron is cycled between +2 and +3 oxidation states, so that Fe(II) is not depleted, and OH· is limited only by the availability of light and H_2O_2 (52,53, 54).

2.2.1.3 H_2O_2/UV PROCESS

The H_2O_2/UV system involves the formation of hydroxyl radicals by hydrogen peroxide photolysis, as shown by Equation (2.17) below (52, 53, 54).

$$H_2O_2 \overset{h\nu}{\leftrightarrow} 2OH\cdot_{(aq)} \quad (\lambda=400nm) \quad (2.11)$$

This equation presents the advantages of working with peroxide, since it provides a cheap and sure source of radicals and eliminates the problem of the handling of chlorine. The major drawback of this process is that the strongly absorbing substances can compete with hydrogen peroxide for radiation. A solution that is cloudy and containing compounds that can absorb UV radiation, can present problems in this method. (52, 53, 54)

2.2.1.4 O_3/H_2O_2 PROCESS

Addition of hydrogen peroxide to ozone offers another way to accelerate the decomposition of ozone, leading to the formation of hydroxyl radicals. The reaction of this process is illustrated in Equation (2.12).

$$H_2O_{2(aq)} + 2O_{3(aq)} \rightarrow 2OH\cdot_{(aq)} + 3O_{2(g)} \quad (2.12)$$

This process does not depend on the UV radiation absorption to activate the ozone or hydrogen peroxide molecules and can be applied to turbid water without problems (52, 53, 54).

2.2.1.5 FENTON'S REACTION PROCESS

The Fenton reaction is one of the most severe oxidizing reactions available. The reaction involves hydrogen peroxide and a ferrous iron catalyst. The H_2O_2 is broken down into a hydroxide ion and hydroxyl free radical. The OH radical is the primary oxidizing species and can be used to oxidize and break apart organic molecules (52, 53, 54).

$$Fe^{2+} + H_2O_2 \rightarrow Fe^{3+} + OH^- + OH\cdot \quad (2.13)$$

Under these conditions, it is considered that the following reaction also occurs:

$$Fe^{3+} + H_2O_2 \rightarrow 2Fe^{2+} + 2H^+ + O_2 \quad (2.14)$$

The reaction above proceeds via the following intermediate steps:

$$Fe^{3+} + H_2O_2 \rightarrow [FeO_2H]^{2+} + H^+ \quad (2.15)$$

$$[FeO_2H]^{2+} \rightarrow HO_2\cdot + Fe^{2+} \quad (2.16)$$

$$Fe^{3+} + HO_2\cdot \rightarrow Fe^{2+} + H^+ + O_2 \quad (2.17)$$

$$2Fe^{2+} + 2H_2O_2 \rightarrow 2Fe^{2+} + 2OH^- + 2OH\cdot \quad (2.18)$$

$$2Fe^{3+} + H_2O_2 \rightarrow 2Fe^{2+} + 2H^+ + O_2 \quad (2.19)$$

$$3H_2O_2 \rightarrow OH\cdot + 2H_2O + O_2 \quad (2.20)$$

Hydrogen peroxide is thus decomposed using Fe^{2+}/Fe^{3+} as a catalyst. There is evidence for the production of the hydroxyl radical (OH·) as an intermediate to the oxygen and hydrogen evolution, looking at the different chemistry reactions of Advanced Oxidation Process (AOP), as summarized in Figure 2.3. The hydroxyl radical (OH·) is a highly reactive, short-lived species that can rapidly oxidize most organic compounds in water (52, 53,54).

2.3 PRINCIPLES OF PHOTOCATALYSIS

The term photocatalysis describe a process where light is used to activate a particular substance. The definition of photocatalysis is "A catalytic reaction involving light absorption by substrate." where the photocatalyst modifies the rate of the chemical reaction without itself being involved in the transformation. The principle of photocatalysis is based on the activation of a semiconductor material by the action of radiation with an appropriate wavelength. (55, 56).

A good photocatalyst should be photoactive, able to utilize visible and near UV light, should be biologically and chemically inert, photostable, inexpensive, and nontoxic in nature. The redox potential of the photogenerated valence band (VB) hole must be sufficiently positive for a semiconductor to be photochemically active so that it can generate •OH radicals that can subsequently oxidize the organic pollutants. The redox potential of the photogenerated conductance band electron must be sufficiently negative to be able to reduce absorbed oxygen to a superoxide (55, 56).

When a photocatalyst is irradiated with a light of suitable wavelength, an electron is excited to the conduction band (CB), leaving behind a positive hole in the valence band (VB). The excited electron reacts with electron acceptors such as O_2 present on the semiconductor surface or dissolved in water, reducing it to superoxide radical anion $O^{2-\bullet}$.On the other hand, the hole can oxidize the organic molecule to form R+, or react with −OH or H_2O, oxidizing them to •OH radicals.(**Figure 2.2**) (57,58).

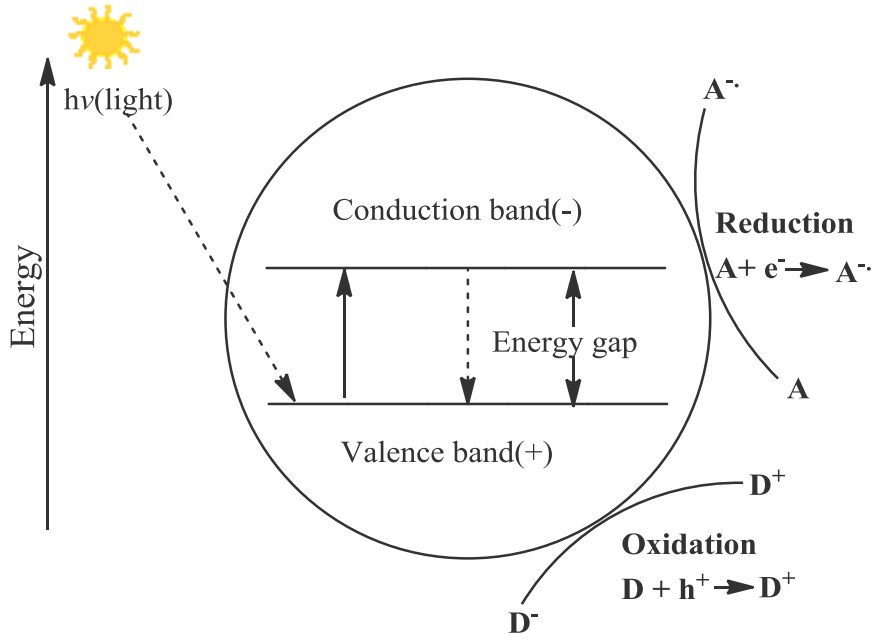

Figure 2.12 Mechanism of Photocatalysis (57).

Photocatalytic reactions proceed with oxygen molecules in air, the oxidation of water is the important process in photocatalytic oxidation, the reduction of oxygen would be the important process in photocatalytic reduction, but taking into account that the surface of TiO_2 photocatalysts is covered with adsorbed water molecules in reaction environments and that photocatalysts are often used to decompose pollutants in water (57,58).

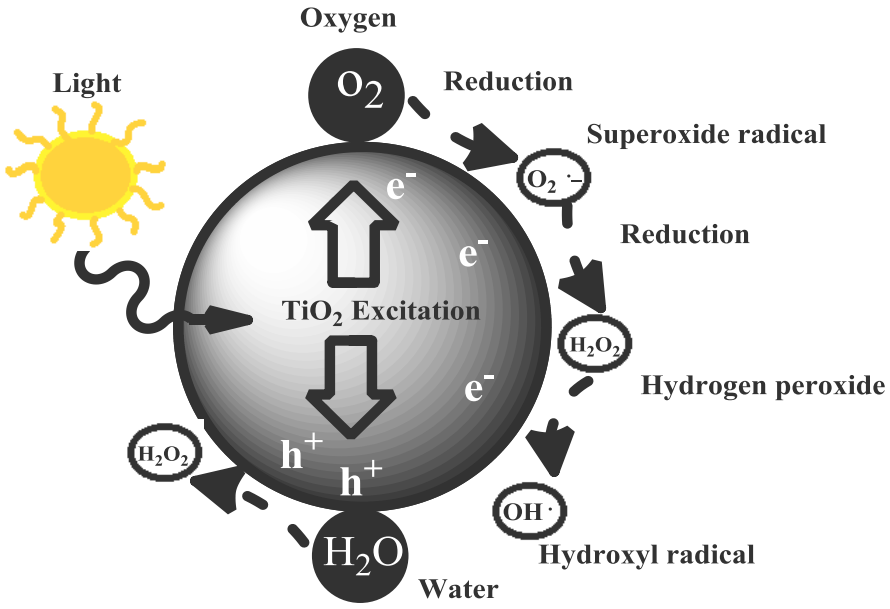

Figure 2.13 One-electron reduction steps of oxygen to OH radical and two-electron oxidation step
of water to H_2O_2 (56).

Figure 2.13 illustrates the reduction steps of oxygen to OH radical and the oxidation steps of water to H_2O_2. Equation 2.1 shows when oxygen is reduced by an electron to become a superoxide radical ($O_2^{\bullet-}$), which further reacts to form hydrogen peroxide (H_2O_2). The reduction of H_2O_2 produces hydroxyl radical ($OH^{\bullet}$).

$$\boldsymbol{O_2 + e^- \rightarrow O_2^{\bullet-}} \quad (2.1)$$

$$\boldsymbol{O_2^{\bullet-} + 2H^+ + e^- \rightarrow H_2O_2} \quad (2.2)$$

$$\boldsymbol{H_2O_2 + H^+ + e^- \rightarrow OH^{\bullet} + H_2O} \quad (2.3)$$

As shown in **Figure 2.3**, when O_2 is reduced by one electron (Equation (2.1)), it becomes a superoxide radical ($O2^{\bullet-}$) that is further reduced by one electron (Eq. (2.2)) to form hydrogen peroxide (H_2O_2). The latter reaction is largely pH dependent because the amount of $HO_2^{\bullet}$, whose p*K*a is 4.8, which changes largely when the pH is neutral. One-electron reduction of H_2O_2 (Eq. (1.3)) produces hydroxyl radical ($OH^{\bullet}$) (56).

2.4 EXAMPLES OF PHOTOCATALYSTS

A number of semiconductors have been used successfully for different applications. These are binary, tertiary and quaternary semiconductors. A binary semiconductor consist of two elements such as GaP or MnO, while a tertiary semiconductor consist of three elements and a quaternary semiconductor consist of four elements.

One of the important properties of TiO_2 nanostructures is its photocatalytic activity. In addition to TiO_2, there is a wide range of metal oxides and sulfides that have been successfully tested in photocatalytic reactions. Among these are ZnO, WO_3, WS_2, Fe_2O_3, V_2O_5, CeO_2 , CdS and ZnS (57). Positions and width of energy bands of some of these semiconductors are presented in Figure 4 and compared to those of TiO_2. Interaction of these semiconductors with photons that possess energy equal or higher than the band gap may cause separation of conduction and valence bands as illustrated in Figure 5. This event is known as electron–hole pair generation. For TiO_2, this energy can be supplied by photons with energy in the near ultraviolet range. This property promotes TiO_2 as a promising candidate in photocatalysis where solar light can be used as the energy source (57,58).

Table 2.1: The band gaps of different binary, tertiary and, quaternary semiconductors (57).

Binary Photocatalysts	**Band Gap(eV)**	**Ternary Photocatalysts**	**Band Gap(eV)**	**Quartenary Photocatalysts**	**Band Gap(eV)**
WSe_2	1.40	**Cu_2InSe_2**	1.00	**$Cu_2ZnSnSe_4$**	1.00
CdTe	1.49	**Cu_2SnS_3**	1.16	**Cu_2ZnSnS_4**	1.50
CdSe	1.74	**$CuInS_2$**	1.55	**$Li_4CuMo_2O_8$**	1.54-1.65
GaP	2.26	**La_2CuO_4**	2.00	**Bi_2AlVO_7**	2.06
TiO_2	3.02-3.20	**$BaTiO_3$**	3.00	**Bi_2lnTaO_7**	2.81
MnO	3.60	**$SrTiO_3$**	3.40	**$FeZn_3Cu_3O_{6.5}$**	2.70

2.5 TiO_2 AS SEMICONDUCTOR

TiO_2 can be used as effective photocatalysts in combating against the problem of environmental pollution. The major advantage of photocatalysis is the fact that there is no further requirement for any secondary disposal methods as the organic contaminants are converted to carbon dioxide, water, inorganic ions. Among the semiconductors, titanium dioxide is the most widely used semiconductor catalyst in photo induced processes. TiO_2 shares advantages of being photocatalytically stable, relatively easy to produce and use, being able to efficiently catalyse reactions, while having a disadvantage of being active only in the ultraviolet region but not the visible light region (57,58).

2.6 STRUCTURAL AND CRYSTALLOGRAPHIC PROPERTIES

Titanium dioxide has a molecular weight of 79.87 g/mol and represents the naturally occurring oxide with chemical formula TiO_2. Titanium dioxide is extracted from a variety of naturally occurring ores. However, most of the titanium dioxide in industry is produced from titanium mineral concentrates by the chloride and sulfate process. The primary Titanium particles are typically between 200–300 nm in diameter, although larger aggregates and agglomerates are also formed. Primary particles are single crystals that are bound by crystal planes. Aggregates are sintered primary particles that are connected by crystal faces. Agglomerates are multiple primary particles and aggregates that are held together by van der Waal's forces (72).

TiO_2 exists in three polymorphic phases: rutile, a tetragonal crystal structure with a density of 4.25 g/cm^3; anatase, a tetragonal crystal structure with a density of 3.894 g/cm^3 and brookite, a orthorhombic crystal structure with a density of 4.12 g/cm^3. Of these phases, anatase and rutile are the most commonly encountered. Rutile is the thermodynamically stable form of TiO_2 at all temperatures and at normal pressures, while anatase is highly photocatalytically active.In all three polymorphs, titanium is coordinated octahedrally by oxygen, but the position of the octahedral differs between polymorphs (72).

Figure 2.14 Phase transition of the titanium dioxide.

The structure of rutile is the densest and its unit cell is the smallest. Anatase has four formula units per unit cell with *a* = 0.375 nm and *c* = 0.951 nm; rutile has two with *a* = 0.458 nm and *c* =

0.295 nm, and brookite has eight with a = 0.916 nm, b = 0.543 nm and c = 0.513 nm. Rutile TiO_2 has 32 atoms and anatase TiO_2 has 96 atoms in the lattice structure. **Table 2.2** illustrates the information of the three polymorphs (72).

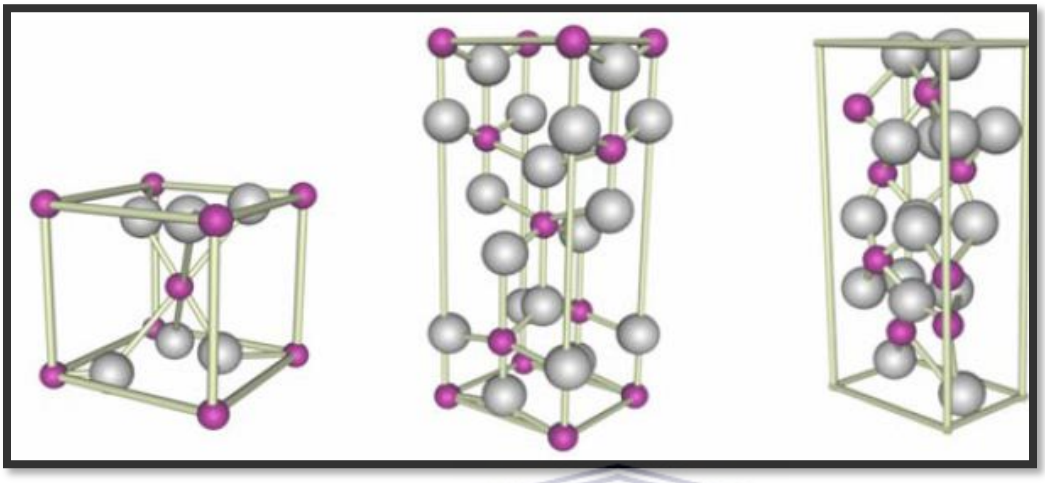

(a) (b) (c)

Figure 2.15 Unit cells of (a) rutile, (b) anatase and (c) brookite. Grey and red spheres represent oxygen and titanium, respectively (72).

In the Unit cell diagrams the grey spheres represent oxygen and the red spheres represent titanium. In their structures, the basic building block consists of a titanium atom surrounded by six oxygen atoms in a distorted octahedral configuration. In all the three TiO_2 structures, the stacking of the octahedra results in three–fold coordinated oxygen atoms (72).

The fundamental structural unit in these three TiO_2 crystals forms from TiO_6 octahedron units and has different modes of arrangement. In the rutile form, TiO_6 octahedra links by sharing an edge along the c axis to create chains. These chains are then interlinked by sharing corner oxygen atoms to form a three dimensional framework. On the contrary, in anatase the three dimensional framework is generated by edge shared bonding among TiO_6 octahedrons. This means that octahedra in anatase share four edges and are arranged in zigzag chains. In brookite, the octahedra share both edges and corners forming an orthorhombic structure. Crystals of titanium dioxide can exist in one of three forms: rutile,anatase or brookite (72,73).

Table 2.2: Crystallographic properties of rutile, anatase and brookite (74).

Crystal Structure	Density (kg/m^3)	Systems	Space group	Cell parameters(nm)		
				A	B	C
Rutile	4240	Tetragonal	D^{14}_{4h} - P4/mnm	0.4584		0.2953
Anatase	3830	Tetragonal	D^{19}_{4a} - 14_1/amd	0.3758		0.9514
Brookite	4170	Rhombohedral	D^{15}_{2h} – Pbca	0.9166	0.5436	0.5135

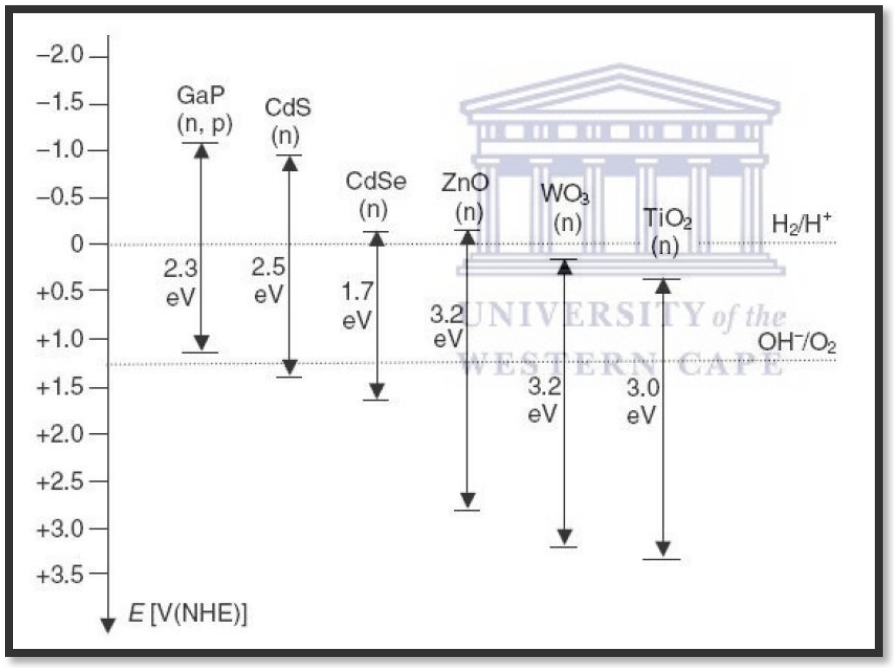

Figure 2.16: Position and width of energy band of TiO_2 and several other illuminated semiconductors with respect to the electrochemical scale (72).

In addition to the wide energy band gap, TiO_2 exhibits many other interesting properties such as transparency to visible light, high refractive index and a low absorption coefficient. Anatase and rutile, the two principal polymorphs of TiO_2, are associated with energy band gap of 3.2 and 3.1 eV, respectively. It has been reported that the photodegradation rate is much more rapid in anatase than in the rutile. This reaction rate is mainly affected by the crystalline state and textural properties such as surface area and particle size. However, these factors often conflict, since a high degree of crystallinity is generally achieved through a high–temperature thermal treatment

leading to a reduction in the surface area. Thus, optimal conditions for the synthesis of TiO_2 have been resulted of the materials of high photoactivity (72,73).

Since photocatalytic reactions are generally studied in aqueous suspensions, problems arise from the formation of hard agglomerates through the diffusion of reactants and products as well as light absorption. The crystal structure of TiO_2 greatly affects its photocatalytic activity. Amorphous TiO_2 seldom displays photocatalytic activity due to the presence of nonbridging oxygen atoms in the bulk TiO_2. The Ti–O atomic arrangement defects could act as recombination centers of photogenerated electron–hole pairs (72,73)

The photocatalytic performance of TiO_2 depends not only on its bulk energy band structure but, to a large extent, on its surface properties. The high photocatalytic activity can be obtained using the photocatalyst with high surface area per mass. The type and density of surface states of TiO_2 nanostructures are affected by the synthesis process. For instance, a soft mechanical treatment of TiO_2 nanopowder was found to reduce its photocatalytic activity in the reduction of Cr(VI). On the other hand, treatment in H_2 or N_2 plasma was found to enhance the activity within the visible–light range for certain reactions. TiO_2 has typically been crystallized in oxidizing atmospheres such as air and oxygen. The effects of the inert atmospheres such as N_2, Ar and vacuum have been overlooked. The calcination atmosphere has been found to have significant effects on the photocatalytic activity of TiO_2. Calcination in hydrogen or in a vacuum results in a high density of defects and low surface hydroxyl coverage yielding low activity. Calcination in Ar, in contrast, enhances visible–light excitation and high hydroxyl coverage leading to higher activity. TiO_2 nanostructures are successfully used for the photocatalytic remediation of a variety of organic pollutants such as hydrocarbons and chlorinated hydrocarbons, for example: CCl_4, $CHCl_3$, C_2HCl_3, phenols, chlorinated phenols, surfactants, pesticides, dyes as well as reductive removal of heavy metals such as Pt^{4+}, Pd^{2+}, Au^{3+}, Rh^{3+} and Cr^{3+} from aqueous solutions.TiO_2 nanostructures have also been affective in the destruction of biological organisms such as bacteria, viruses and molds (73,74).

2.7 DOPING

TiO_2 has been modified in order to improve catalytic activity. Different forms of modification has been done including doping TiO_2 with metal or non-metals and by modifying the surface with organic molecule. Doping is a process of adding a very small amount of a foreign substance to a very pure semiconductor. Doping of a semiconductor is an important approach in band gap modification as it changes some important properties of a semiconductor such as structural, morphological, electrical, and optical properties which influence the absorbance of light, redox potential and charge-carrier mobility(57,63).

Doping in semiconductors results in a bathochromic shift, which decreases the band gap enabling the semiconductor to harness more photons from the visible light region. A number of properties of a semiconductor are affected by the process of doping. The major ones are as follows: Narrowing of the band gap, addition of impurity energy level, formation of oxygen vacancies, optical properties, crystallinity, surface morphology, surface area, porosity, and wettability (57,63).

Metal and nonmetal dopants provide new energy levels to reduce the band gap of a photocatalyst. It is due to the creation of new bands below the conduction band (CB) or above the valence band (VB) by a metal or nonmetal, respectively Figure 7.1). Thus, the doping process leads to the formation of new energy levels (reduction of band gap) and as a consequence, less energy ($h\nu$) is required from the VB. It also improves trapping of electron and avoids electron–hole recombination during irradiation (57).

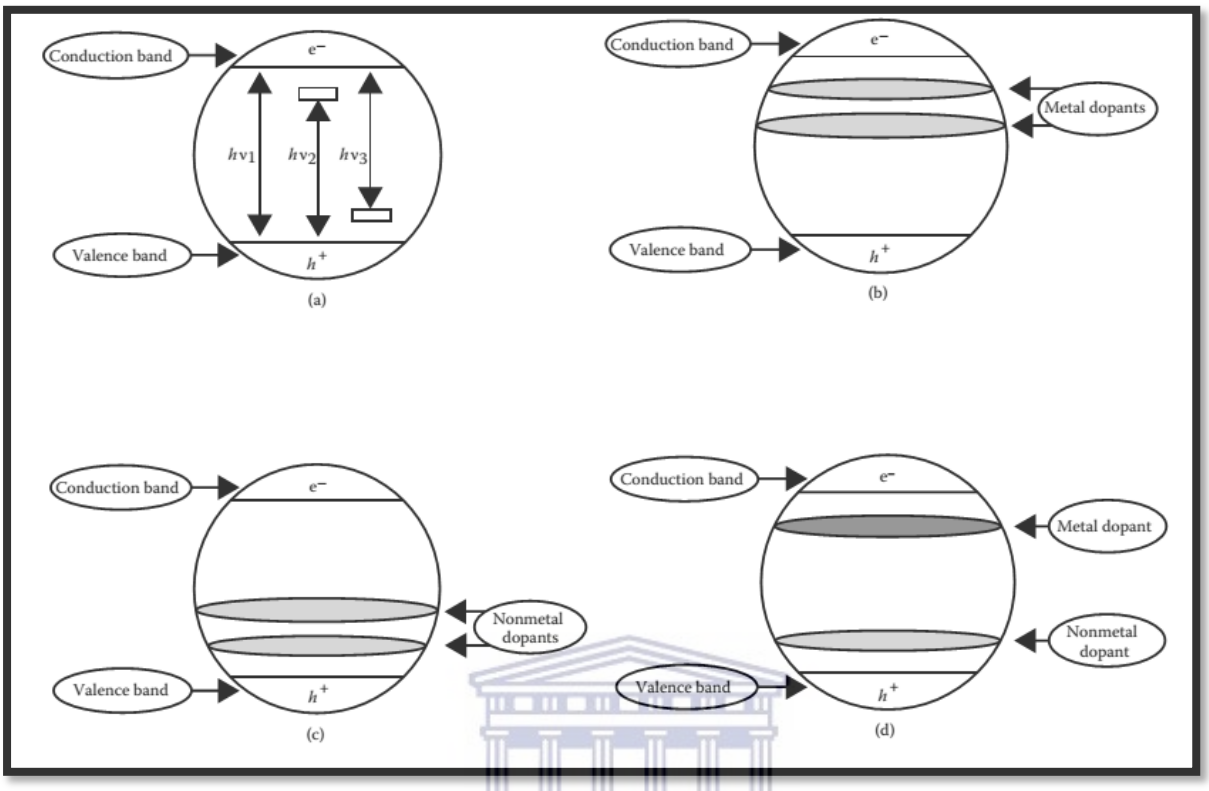

Figure 2.17 Band structure of (a) bare photocatalyst and with (b) metal dopant, (c) non-metal dopant, and (d) metal–nonmetal codopant. *hν*1, *hν*2, and *hν*3 represent the band gap for pure, metal-doped, and nonmetal-doped semiconductors, respectively (57).

2.7.1 METAL DOPING

Most of the metal oxides have a limited range of light absorption and an inefficient charge separation, which leads to a high recombination rate with concomitant diminishing of their photocatalytic activity and limitation of future applications. Therefore, introducing a metal ion as a dopant leads to development of new visible light–induced photocatalysts with improved physicochemical properties. Thus, metal dopants improve the morphology, electronic, magnetic properties, and photocatalytic performance of photocatalytic semiconductors. A large number of studies have been carried out on various metal dopants such as vanadium, chromium cobalt, copper , iron , manganese, zinc and palladium, to enhance activity of metal oxides under the sunlight for different applications (57,64).

The performance of a photocatalyst increases due to shifting the absorption spectra to a lower energy region and limiting the recombination rate of the photogenerated electron and hole. Metal ions get incorporated in the semiconductor lattice on metal doping, which effectively enhances the photocatalytic performance of metal oxides by broadening the absorption range in the visible region of the solar spectrum and by modifying the redox potential of the photoexcited species. In titania, modification in the presence of a dopant does not always exhibit positive results, and sometimes it may lead to adverse results. Mostly doping of metal ions increases the activity of a photocatalyst, but none of them shows stable activity after a certain period of time because of the instability of the dopant against photocorrosion (57,65).

2.7.2 NON-METAL DOPING

Investigation of the substitutional doping of Nitrogen for Oxygen have been carried out, the interaction of N 2p state of nitrogen dopant with O 2p state in anatase TiO2 have been monitored, due to their very close energy levels. Thus, nitrogen doping leds to narrowing of the band gap and also increases photocatalytic activity of a semiconductor in visible light. There are three different main opinions regarding the modification mechanism of TiO2 doped with nonmetals. These include band gap narrowing, impurity energy levels and oxygen vacancies. An additional benefit of doping is the increase in electron trapping, which inhibits electron–hole recombination during irradiation and results in enhanced photoactivity(57, 65).

Addition of impurities in the energy levels above the VB has been reported, when doping titanium dioxide with nitrogen. These levels are formed due to substitution of the oxygen site by a nitrogen atom. Irradiation with UV light excited electrons in both the VB and the impurity energy level, but irradiation with visible light excited electrons present only in impurity level. Zhao and Liu (2008) discussed some modifications in the mechanism of activity of N-doped TiO2. The experimental results showed that TiO2 doped with substitutional nitrogen had shallow acceptor states above the valence state. On the contrary, TiO2 doped with interstitial nitrogen has isolated impurity states in the middle of the band. The oxygen-deficient sites formed in the grain boundaries were essential to emerge visible activity, and N-doped TiO2 in a part of the oxygen-deficient sites were important as blockers of the redox reaction(57,65).

2.7.3 CO-DOPING

The combination of different donor and acceptor dopants leads to the narrowing of the band gap that results in the bathochromic shift (red shift). Thus, due to the synergistic effect of dopants, codoping shifts the absorption edge successfully from the UV region to visible light region, that is, it helps in broadening of the absorption band. The process of adding donor–acceptor dopants is known as codoping. It helps to resolve some problems such as the solubility limit, carrier recombination, low carrier mobility, and nonresponse to the visible light in a host material. Some of the adverse features of photocatalysts such as wide band gap, being colorless (or light colored) in most cases, high recombination rate, and so on, are responsible for their lower photoactivity in the visible region of solar spectrum. As a major portion of solar spectrum consists of the visible region, it is of utmost importance to modify the photocatalyst so that it could be used in the visible region along with the UV region of solar spectrum(57,66).

Doping of a semiconductor has proved to be an effective way to overcome this problem of the bare photocatalyst. This doping process has a major influence on certain properties such as structural, morphological, electrical, and optical properties of a semiconductor. Thus, doping of various metal oxides and mixed oxides can be used as one of the major strategies to reduce the large band gap of semiconductor materials and make them effective in the visible light range. Modified photocatalysts have wide applications in the field of environmental remediation such as pollutant degradation, solar fuel generation, decolourization and removal of synthetic dyes (57,66).

2.8 GRAPHENE-BASED COMPOSITES

Graphene has attracted much attention among the more recently discovered carbonaceous materials with a unique sp2 hybrid carbon network. Carbonaceous nanomaterials have unique structures and properties that can add attractive features to some photocatalysts. Generally, enhancement in photocatalytic activity is ascribed to the suppressed recombination of photogenerated electron–hole pairs, extended excitation wavelength, and increased surfaceadsorbed reactant. Researches have reported recent progress in the development of TiO2/nanocarbon photocatalysts covering activated carbon, fullerenes, CNTs, and GR. It shows

wide applications in fields such as nanoelectronics, sensors, catalysts, and energy conversion (57, 58).

Graphene based architectures are highly desirable in the field of photocatalysis as they have promising energy and environmental applications. Single layer graphene sheets not only provide high-quality two-dimensional (2D) photocatalyst support, but also a 2D circuit board, with an attractive potential to connect their perfect electrical and redox properties. Graphene oxide (GO) suspended in ethanol undergoes reduction as it accepts electrons from the UV-irradiated TiO_2 suspensions. This reduction is accompanied by changes in the absorption of the GO, as evident from shifts in the colour of the suspension from brown to black. A direct interaction between TiO_2 particles and GR sheets hinders the collapse of exfoliated sheets of GR. Solid films cast on a borosilicate glass gap separated by gold-sputtered terminations show an order of magnitude decrease in lateral resistance following reduction with the TiO_2 photocatalyst. The photocatalytic methodology not only provides an on-demand UV-assisted reduction technique, but it also opens up new avenues to obtain photoactive GR-semiconductor composites (57,58,59).

Charge separation was observed upon the UV irradiation of a deaerated suspension of TiO_2 colloids. The holes are scavenged to produce ethoxy radicals in the presence of ethanol, thus leaving the electrons to accumulate within TiO_2 particles. The accumulated electrons serve to interact with the GO sheets in order to reduce certain functional groups. **Figure 2.3** TiO_2-G nanocomposite and its response under UV excitation. The colour of the nanopartlicles changes with GO before and after UV irradiation(57,58,59).

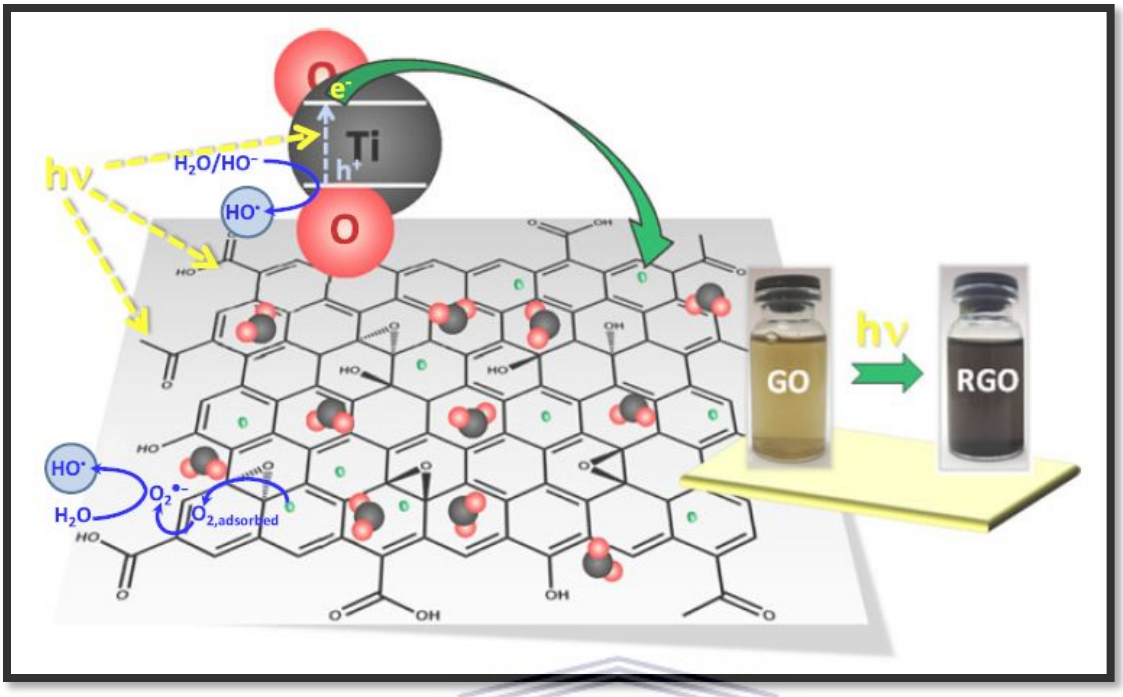

FIGURE 2.18 TiO_2–G nanocomposite with generation of HO radicals from adsorbed oxygen and water (57)**.**

2.9 PHOTOCATALYSIS PROPERTIES OF GRAPHENE AND ITS DERIVATIVES

To rationally implement properties of graphene and its derivatives in designing composites for photocatalysts, a deep understanding on their properties influencing photocatalytic reactions is necessary. In this section, several key photocatalysis-related properties of graphene and its derivatives we will highlight, when designing graphene-based composite photocatalysts (67,69).

The fundamental properties of graphene are essentially dependent on their unique structure, surface, and interface features, such as atomic arrangements, surface chemistry, electronic structures, charge transport, molecular adsorption, and activation abilities for specific reactants. These properties include excellent electrical conductivities, strong capability in accepting electrons, work function, and surface physical and chemical properties. Importantly, the surface and electrical properties of graphene can be also changed through appropriate chemical modification and by controlling its structural order (67,69).

2.10 Nitrogen Doping

Nitrogen doping has been an effective way to modify the properties of graphene and render its potential use for various applications. Three common C – N bonding configurations are normally obtained when doping nitrogen into the graphene lattice; pyridinic N, pyrrolic N, and graphitic N. Attempts have also been made to introduce nitrogen into graphene sheets in order to modify their electronic properties. The formation of the C–N bond occurs mostly at the edges of graphene where chemical reactivity is high (68).

2.11 CRYSTAL STRUCTURE PROPERTIES OF GRAPHENE

The wide applications of graphene in photocatalysis are attributed to its extraordinary electronic properties as a result to its high quality crystal lattice structure. In graphene, the valence orbitals of a carbon atom with primarily *sp*2 hybridization are composed of three planar δ orbitals which are separated by an angle of 120° to each other and one remaining 2*p* orbital (2*pz*) oriented along the axis perpendicular to the graphene plane. Giving graphene the hexagonal honeycomb lattice structure (67, 69).

2.12 THE SEMI-METAL PROPERTIES OF GRAPHENE

The band alignment of two different materials is determined by their respective work functions. The work function is defined as the minimum energy necessary to eject an electron, whose change can be dependent on the Fermi level shift. The contact barriers between graphene and semiconductors could be reduced through efficient controlling of the graphene work function (67, 69).

It is known that the work function of graphene is as large as graphite, about 4.42 eV, and increases with the number of graphene layers. Similarly, the work function of graphene film can be also up-shifted to from 0.5 to 1 eV by metal chloride doping such as $AuCl_3$, $IrCl_3$, $MoCl_3$ and $RhCl_3$. More interestingly, hole doping leads to an increase in the work function by as much as 400 mV. However, the work function of N-doped graphene depends sensitively on the nitrogen doping site. The nitrogen doping at a graphitic site decreases the work function of graphene, while doping at a pyridinic or pyrrolic site increases the work function (67, 69).

It is widely recognized that graphene plays an important role in accepting, storing and subsequently shuttling photo-induced electrons as conductive supports and alternative electron

reservoirs. The conductive graphene can also inhibit the aggregation and growth of semiconductor nanostructures as their support, thus beneficial for the enhancements of surface area and photocatalytic activity (67, 69).

2.13 THE SEMICONDUCTOR PROPERTIES OF GRAPHENE

The functionalization modification of graphene, which include covalent bonds, adsorption, bonds, and lattice incorporation, can govern the electrical properties of graphene through molecular interactions, which make functionalized graphene either an n-type or p-type semiconductor. The electrical properties are typically modulated based on three mechanisms: (a) conversion of carbon's hybridized state, (b) dipole interactions enhanced via quantum capacitance, and (c) orbital hybridization with an interfacing molecule. Several methods have been proposed to open the band gap in graphene, such as chemical functionalization, multilayer graphene, molecular adsorption, confinement, and edge-effects induced bandgap (67, 69).

It is also known that GO with additional oxygenated components is a p-type semiconductor with a small band gap in nature. The GO sheets can be altered from p-type to n-type through replacing those oxygenated components with nitrogen-rich counterparts. Importantly, the band gap of GO can be adjusted through tuning its oxidation level, since its electronic properties strongly depend on the degree of oxidation. For example, GO alone can work as an effective photocatalyst for hydrogen production from water in an aqueous methanol solution under visible-light irradiation. The H_2 evolution activity of GO nanosheets from aqueous methanol solution could be signifiantly enhanced by loading Ni and NiO as co-catalysts. With appropriate tuning of the oxygenation degree, the CB and VB positions of GO can be made suitable for H_2 and O_2, generation, respectively, thus achieving the overall water splitting (67, 69).

2.14 ELECTRICAL CONDUCTIVITY PROPERTIES OF GRAPHENE

The semimetal graphene exhibits outstanding electrical conductivity. Unlike graphite, graphite oxide produced is electrically insulating, which limits its usefulness as conductive additives in nanocomposites. However, the electrical conductivity of graphite oxide can be significantly increased by chemical and thermal reduction. It has been demonstrated that electrical conductivity measurements indicate a 10 000-fold increase in conductivity after chemical reduction of GO to graphene. For comparison, a study was undertaken by Stankovich et al. that measured the room-temperature electrical conductivities of compressed-powder samples of the pristine graphite, GO, and the reduced GO. The results clearly demonstrated that the conductivity data for the reduced GO (≈2 × 102 S m −1) is about 5 orders of magnitude better than that of GO, and close to that of pristine graphite which is about 10 times lower than the conductivity of pristine graphite powder (67, 69).

2.15 CHARGE TRANSPORT PROPERTIES OF GRAPHENE

The charge transport properties of unsuspended graphene samples can inhibited by the low density of defects due to the presence of strong impurity scattering and limited electron mean free path. In 2008, a study at Columbia University demonstrated that a carrier mobility in a single layer of mechanically exfoliated graphene is larger than 200 000 $cm^2\ V^{-1}\ s^{-1}$ which is comparable to that of silver 1.62×106 $cm^2\ V^{-1}\ s^{-1}$. However, the optimized RGO can only achieve the intrinsic mobility values of 5000 $cm^2\ V^{-1}\ s^{-1}$, which is much smaller than that of pristine graphene. Therefor the minimized extrinsic sources of scattering from defects might be also beneficial for the enhancements of both electronic conductivities and carrier mobility, thus greatly enhancing the photocatalytic activities of graphene-based photocatalysts (67, 69).

2.16 ELECTROCHEMICAL PROPERTIES GRAPHENE

Although graphene is intrinsically inert, it has been demonstrated that the heteroatom-doped graphene-based materials and graphene-based hybrid nanostructures exhibit excellent electrocatalytic activity toward H_2 evolution, CO_2 reduction, O_2 reduction, and O_2 evolution. It is implied from previous reports that the modified graphene might be an excellent co-catalyst for the photocatalytic applications. Once the graphene got the photo-excited electrons from the conduction band of the semiconductors, it is naturally expected graphene itself can also serve as an excellent co-catalyst replacing the well-known expensive noble metal co-catalysts, which

include Pt, Au and Ag, because its work function being more negative than the reduction potentials of H_2 evolution, O_2 reduction and some multi-electron transfer reactions of CO_2 to hydrocarbon fuels (67, 69, 70).

The recently published papers demonstrated that the graphene co-catalysts can greatly promote the reaction rates of various photocatalytic reactions. A series of graphene-based co-catalysts for photocatalytic H_2 evolution have been developed. For example, the 1.0 wt% graphene-loaded TiO_2 nanosheets with exposed (001) facets exhibit a 41-fold enhancement of photocatalytic H_2-production activity in aqueous solutions containing methanol, without Pt co-catalyst. In addition, the N-doped, N/S and B/N co-doped graphene nanosheets have been proven to be good co-catalysts for accelerating the O_2-reduction reaction, which is considered as the rate-determining step in solar-driven photocatalytic mineralization of organic pollutants.It is expected that these modified graphene can be widely used as O_2-reduction co-catalysts for photocatalytic degradation (67, 69, 70).

2.17 APPLICATIONS OF GRAPHENE-BASED COMPOSITES

Graphene-based TiO_2 composites have been recently used for the photodegradation of pollutants, while also being applied in many other fields, including solar cells and hydrogen production that are related with the preservation of the environment.

2.17.1 Photodegradation of pollutants and microorganisms

The photoinactivation of Escherichia coli bacteria in aqueous solutions under solar light irradiation was one of the first applications of GO–TiO_2 films, which showed significantly higher efficiencies in comparison to bare anatase TiO_2 films with an enhancement by a factor of ~7.5. The better performance was attributed to the suppression of electron–hole recombination (76).

In literature, some of the target pollutants are dyes, such as methylene blue(MB), methyl orange (MO), and rhodamine B (RB). The degradation of MO under visible light was studied with RGO–TiO_2 composites prepared with different GO contents. The composites with 0.13–0.15 wt% carbon content were more active than P25, the highest conversion being obtained for a composite prepared with 0.14 wt%. GO acted as a sensitizer, enhancing the photocatalytic performance towards wavelengths longer than 510 nm. GO–TiO_2 composites presented relatively high efficiency for the degradation of MO under UV light after several consecutive cycles, but a decrease of the MO conversion was noticed after each cycle and attributed to the

agglomeration of TiO_2 grains formed on both sides of the graphene oxide layers. This agglomeration led to a decrease of the contact area between MO molecules and TiO_2 particles, also resulting in a reduction of the photodegradation efficiency (77).

2.17.2 OTHER APPLICATIONS OF GRAPHENE-BASED COMPOSITES

Hydrogen production from water splitting is another application of interest in this area, since the extension of light absorption to the visible light region for development of solar-driven technologies, and the suppression of electron– holes recombination, are also key factors in this process. G–TiO_2 composites already showed higher production of hydrogen than P25. The highest photocatalytic activity was obtained with G–TiO_2 composites with 5 wt% of graphene and treated in a nitrogen atmosphere, hydrogen production exceeding more than two times that observed for P25, using Na_2S and Na_2SO_3 as sacrificial agents. RGO–P25 composites were also more effective for hydrogen production from methanol aqueous solution than CNT–P25. In addition, this RGO–P25 composite yielded a higher hydrogen production rate from pure water than P25, due to the fast transfer of photogenerated electrons on P25 to RGO, suppressing the recombination of charge carriers. Because the photocatalytic activity of anatase TiO_2 nanosheets is largely enhanced by the presence of (001) facets , RGO–TiO_2 composites were designed following this approach, showing an excellence photocatalytic behaviour for the hydrogen production, using methanol as sacrificial agent. In this case, the optimum graphene content was ca. 1 wt%, the yield of hydrogen being 41 times higher than that shown for bare TiO2 and also higher than RGO–P25 prepared under a similar procedure (79).

Technologies based on dye-sensitized solar cells (DSSC) are also promising and present increasing potential for large scale conversion of sunlight into electrical energy at affordable costs. The photoanodes of DSSCs are typically constructed using thick films of TiO_2 nanoparticles, providing anchoring sites for dye molecules. However, electron transport across disordered TiO_2 nanoparticles is not yet effective enough, and the recombination of the photogenerated electrons can take place, decreasing the efficiency of DSSCs. Graphene-based TiO_2 composites have already been used in the fabrication of DSSC, showing encouraging results .The incorporation of graphene improves conductivity by a factor larger than 2, and increases power conversion by a factor larger than 5, in comparison with TiO_2 alone. The better performance of the G–TiO_2 composite was also attributed to the better dye loading on the G–TiO2 film, compared to the TiO2 film (79).

CHAPTER THREE: METHODS AND MATERIALS

3. INTRODUCTION

This chapter gives a detailed presentation of the experimental methods and chemicals utilized during this research project. The characterization of materials is important for understanding their properties and applications. This chapter also describes the instruments and instrumental set ups utilized for various measurements towards the characterization of the synthesized TiO_2 nanocomposites.

3.1 MATERIALS AND CHEMICALS

The materials and chemicals used in this study and their suppliers are listed in **Table 3.1**, the chemicals were not modified before being used.

Table 3.1: Summary of chemicals used for the synthesis in the project without further purification.

Chemical name	Purity	Supplier
$NaNO_3$	99%	Sigma-Aldrich
Graphite		Sigma-Aldrich
H_2SO_4	98%	Kimix
$KMnO_4$	99%	Kimix
Melamine	99%	Kimix(Aldrich)
Ethanol	99%	Kimix
TiO_2	99.6%	Alfa Aesar
KOH	85%	Alfa Aesar
HCl	32%	B & M Scientific

3.2 METHODS OF SYNTHESIS

This section focuses on the detailed description of the methodology used to synthesize the graphene materials and TiO_2 nanocomposites.

3.2.1 PREPARATION OF N-GRAPHENE OXIDE

Nitrogen doped graphene oxide was synthesized from graphite powder by a modified Hummers method, the modified method involves both oxidation and exfoliation of graphite sheets due to thermal treatment of the solution. In the synthesis graphite flakes (2g) and $NaNO_3$ (2g) were mixed with H_2SO_4 (90mL) in a volumetric flask (1000 mL), the temperature was controlled with an ice bath (0^oC). The mixture was stirred (4 hours) at a constant temperature, $KMnO_4$(12g) was slowly added to the suspension to keep the temperature lower than 15 ^oC. Melamine (2g) was then added into the suspended mixture and was continuously stirred (12 hours) at room temperature. Consequently, deionized water (50mL) was added drop-wise, while the temperature was kept at 90^oC for 1 hour. Subsequently, H_2O_2 (20 mL) was added into the suspension. The material was centrifuged and washed several times with deionized water and ethanol. The N-GO material was dried in an oven (40^oC) for several days.

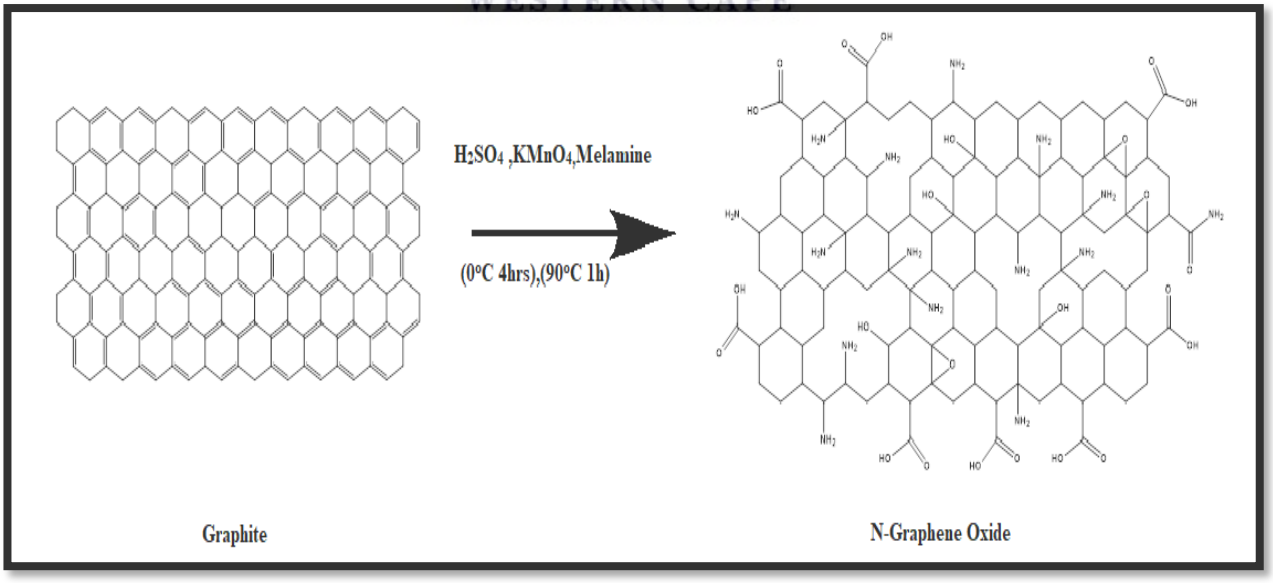

Figure 3.1: Preparation of N-graphene oxide.

3.2.2 PREPARATION OF GRAPHENE OXIDE

Graphene Oxide was synthesized using the modified Hummers method. In the synthesis graphite flakes (2g) and $NaNO_3$ (2g) were mixed with H_2SO_4 (90mL) in a volumetric flask (1000 mL), the temperature was controlled with an ice bath (0^oC). The mixture was stirred (4 hours) at a constant temperature, $KMnO_4$(12g) was slowly added to the suspension to keep the temperature lower than 15 ^oC. Consequently, deionized water (50mL) was added drop-wise, while the temperature was kept at 90^oC for 1 hour. Subsequently, H_2O_2 (20 mL) was added into the suspension. The material was centrifuged and washed several times with deionized water and ethanol. The GO material was dried in an oven (40^oC) for several days.

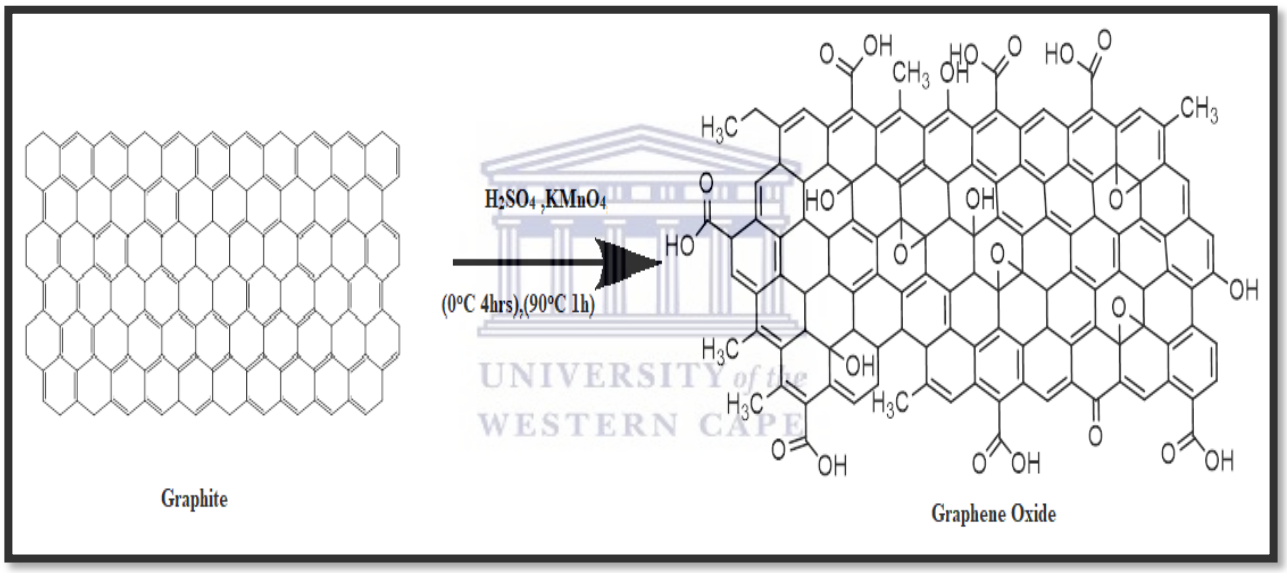

Figure 3.2: Preparation of graphene oxide

3.2.3 PREPARATION OF REDUCED GRAPHENE FROM GRAPHENE OXIDE

1g of graphene oxide was dispersed in 1L water, by means of 30 minutes ultrasonic treatment. As a result, a homogeneous brown GO aqueous suspension was obtained. The pH of the suspension was adjusted to 10 by dropping NH_3H_2O. A mount of hydrazine hydrate was added into suspension and heated at 80°C for 24 hours, and the weight ratio of hydrazine hydrate and GO was controlled to a ratio of 10: 7. The product was obtained and filtered with the qualitative filter paper. A black flocculent substance was gradually precipitated out of the solution. The resulting black product was washed with ethanol and water and dried at 80°C for 24 hours.

3.2.4 PREPARATION OF TIO_2 NANOMATERIALS

The synthesis of titanium dioxide nanoparticles has been extensively investigated, and modern processes have been developed to refine and control the stability as well as the phase formation of the colloidal precursors. However, because the mesoporous TiO_2 particles are randomly connected, this unavoidably leads to the recombination of electron-hole pairs, decreasing efficiency. Subsequently, researchers started to explore the use of TiO_2 nanowires as they possess excellent photocatalytic properties. Different preparation methods TiO_2 nanowires and nanoparticles are discussed in this chapter (58).

3.2.4.1 SYNTHESIS OF TIO_2 NANOWIRES

3.2.4.1.1 MICROWAVE PROCESS

TiO_2 nanowires were prepared from TiO_2 nanoparticles through the microwave heating process, the process was pressure controlled and the reaction times were computerized. TiO_2 nanoparticle powder (2g) was mixed with KOH (10M) and was transferred to a teflon vessels. The samples were treated at the pressure (3.0MPa) with irradiation power (500W) at the duration (60 minutes). The resulting powders were washed with deionized water and air dried (80^{o}C). The obtained titanate nanowires were put in 1M HCl (200 ml) acid-wash treatment and stirred (24 hours). The material was filtered,washed with distilled water and dried(80^{o}C). The product was calcined for 2 hours (700 ^{o}C), white powder anatase nanowires were obtained.

3.2.4.1.2 HYDROTHERMAL PROCESS

Hydrothermal approach was adopted to synthesize crystalline anatase TiO_2 nanowires. In a typical preparation procedure, 3 g TiO_2 were added into 100 mL KOH aqueous solution (10 M) and stirred for 30 min until a homogeneous suspension was gained. A Teflon-lined autoclave (125 mL capacity) was filled with this suspension up to 80% of the total volume. Sealed into a stainless steel tank, the autoclave was kept at 200°C for 24 hours and then cooled down naturally to room temperature. The obtained product was successively washed with dilute HCl aqueous solution, deionized water and methanol for several times until the pH value equaled to 7. After recovered by vacuum filtration, the wet product was baked at 70°C for 6 hours, and eventually the white-colour anatase TiO_2 nanowire powder was obtained.

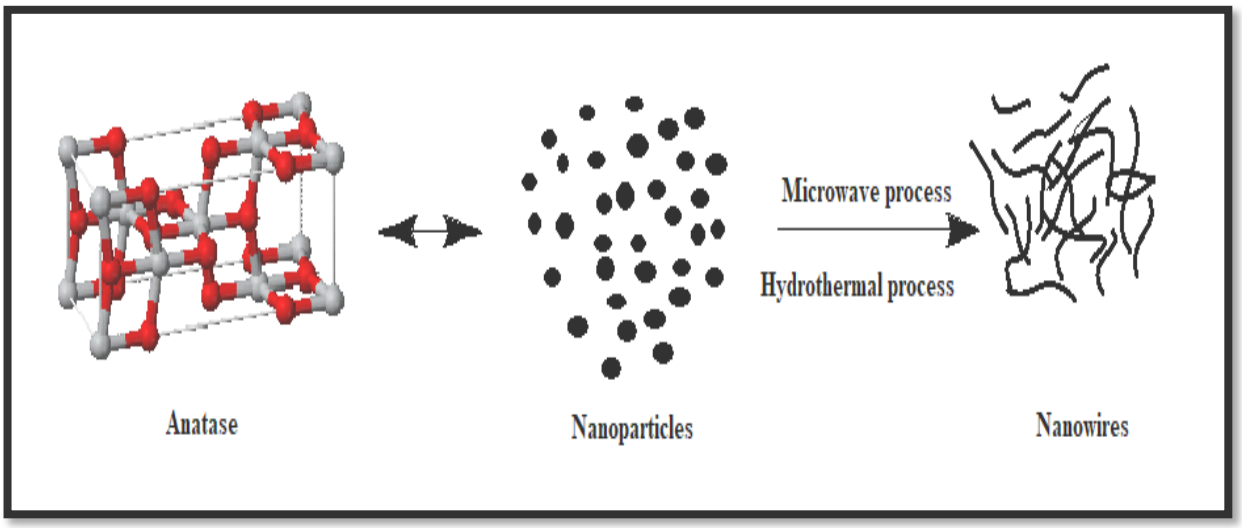

Figure 3.3 Synthesis of TiO_2 nanowires

SYNTHESIS OF TIO_2 SUPPORTED ON REDUCED GRAPHENE OXIDE NANOWIRES

3.2.4.2 MICROWAVE PROCESS

GO was synthesized from graphite powder by the modified Hummers method, TiO_2 nanowires were prepared by the microwave heating process. The G/TiO_2 composites were prepared by the hydrothermal method. GO (20mg) was dissolved in a solution of H_2O (80mL) and ethanol (40 mL) mixture using ultra-sonication treatment (2 hours). TiO_2 (200mg) was added to the obtained GO solution and stirred (2 hours) to obtain a homogenous suspension. The suspension placedin a teflon-sealed autoclave (200mL) and maintained for 3 hours at (120 ^oC). In this process the reduction of GO and deposition of TiO_2 on graphene sheets were stimulated. The obtained composite was recovered by filtration, washed with deionized water and dried for 12 hours (70 ^oC).

3.2.4.3 HYDROTHERMAL PROCESS

Hydrothermal method was employed to synthesize G-TiO_2 nanowire nanocomposite. 30 mg of GO was mixed into a solution of 90 mL deionized water and 30 mL ethanol under sonication for 1 hour to re-exfoliate the GO thoroughly, and 3 g of the prepared TiO_2 nanowires was added to the GO suspension. Then the sonication and stirring was applied alternately for 2 hours with 30 min for each step until a homogeneous suspension was achieved, which showed a uniform light gray color. The suspension was then poured into a Teflon-lined autoclave of 125 mL capacity and maintained at 120°C for 3 hours to synthesize G-TiO_2 nanowire nanocomposite. This process simultaneously reduces GO to RGO by electron donation from ethanol and formed Ti-O-C bonding between TiO_2 and RGO. After cooled down to the room temperature, the suspension was filtered several times with deionized water and the product was dried at ambient condition.

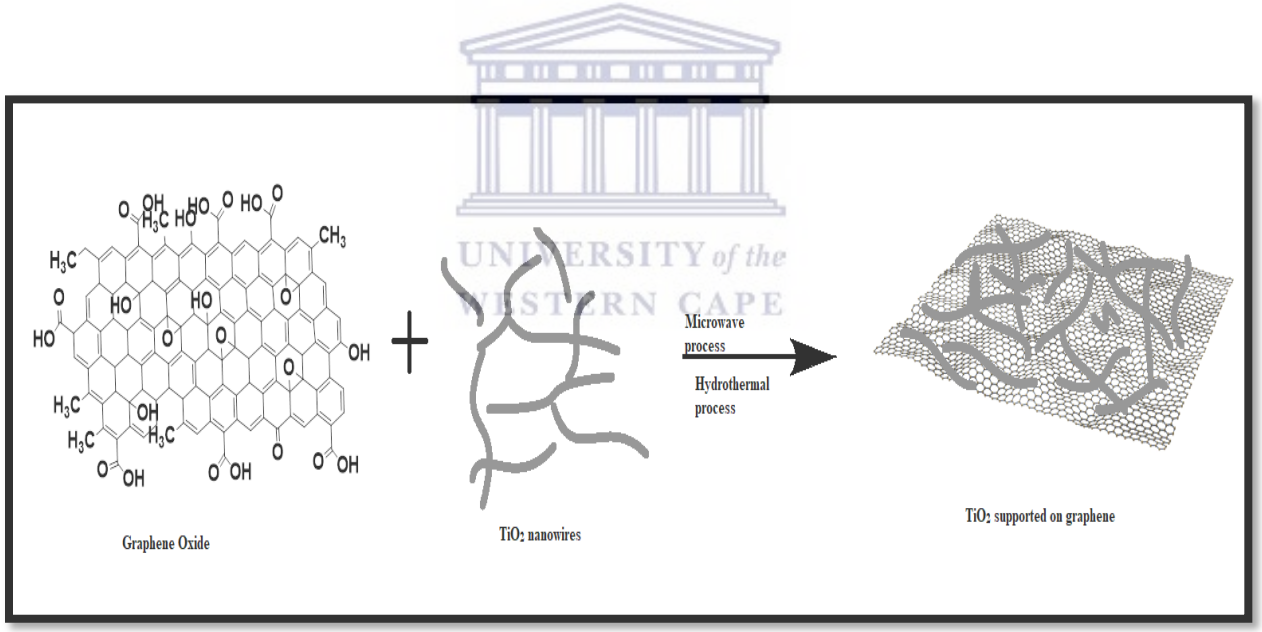

Figure 3.4 Synthesis of TiO_2 supported on reduced graphene oxide nanowires

3.2.6 SYNTHESIS OF TIO_2-NG SUPPORTED ON N-REDUCED GRAPHENE OXIDE NANOWIRES.

3.2.6.1 MICROWAVE PROCESS

N-GO was synthesized from graphite powder by the modified Hummers method, TiO_2 nanowires were prepared by the microwave heating process. The N-G/TiO_2 composites were prepared by the hydrothermal method. N-GO (20mg) was dissolved in a solution of H_2O (80mL) and ethanol (40 mL) mixture using ultra-sonication treatment (2 hours). TiO_2 (200mg) was added to the obtained GO solution and stirred (2 hours) to obtain a homogenous suspension. The suspension placedin a teflon-sealed autoclave (200mL) and maintained for 3 hours at (120 ^oC). In this process the reduction of N-GO and deposition of TiO_2 on graphene sheets were stimulated. The obtained composite was recovered by filtration, washed with deionized water and dried for 12 hours (70 ^oC).

3.2.6.2 HYDROTHERMAL PROCESS

Hydrothermal method was employed to synthesize N-GO/TiO_2 nanowire nanocomposite. 30 mg of N-GO was mixed into a solution of 90 mL deionized water and 30 mL ethanol under sonication for 1 hour to re-exfoliate the graphene oxide thoroughly, and 3 g of the prepared TiO_2 nanowires was added to the N-GO suspension. Then the sonication and stirring was applied alternately for 2 hours with 30 min for each step until a homogeneous suspension was achieved, which showed a uniform light gray color. The suspension was then poured into a Teflon-lined autoclave of 125 mL capacity and maintained at 120°C for 3 hours to synthesize N-GO/TiO_2 nanowire nanocomposite. This process simultaneously reduces N-GO to N-RGO by electron donation from ethanol and formed Ti-O-C bonding between TiO_2 and N-RGO. After cooled down to the room temperature, the suspension was filtered several times with deionized water and the product was dried at ambient condition.

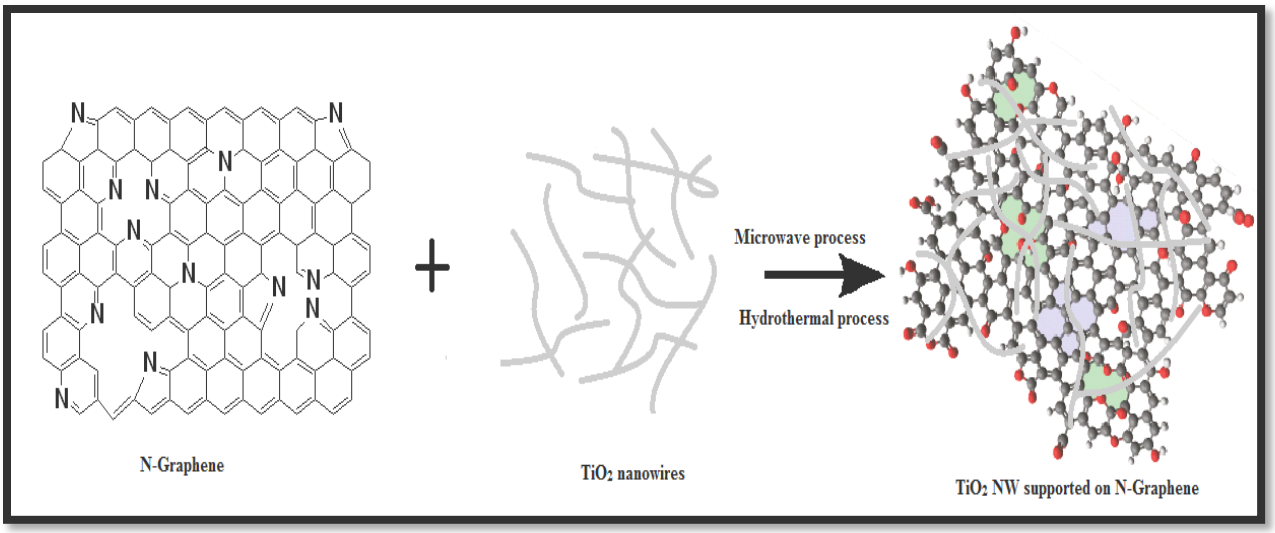

Figure 3.5 Synthesis of TiO_2 supported on reduced graphene oxide nanowires

3.3 CHARACTERISATION TECHNIQUES

Various techniques were used to characterize the synthesized materials. The objective was to study the physical and optical properties of the synthesised nanocomposites. The techniques that were used in the analysis are: Transmission Electron Microscopy (TEM), Scanning Electron Microscopy (SEM-EDS), Fourier Transform Infrared Spectroscopy (FTIR), Ultraviolet and Visible Spectroscopy (UV-Vis) and X-ray Diffraction (XRD), Raman spectroscopy and electrochemical methods (Cyclic Voltammetry, Electrochemical Impedance Spectroscopy, Chronopotentiometry).

3.3.1 HR-Transmission Electron Microscopy

HR-Transmission Electron Microscopy is an effective direct observation method to view the atomic and molecular arrangement. TEM is an effective probe to study the size and shape of nanoparticles. The crystallinity and size of the particles can also be determined from TEM analysis.

3.3.1.1 Principle

In this form of microscopy, a beam of electrons transmits through an extremely thin specimen, and then interacts with the specimen when passing through it [96]**.** The sample must be thin enough to transmit sufficient electrons such that enough intensity falls on the screen to give an image (79).

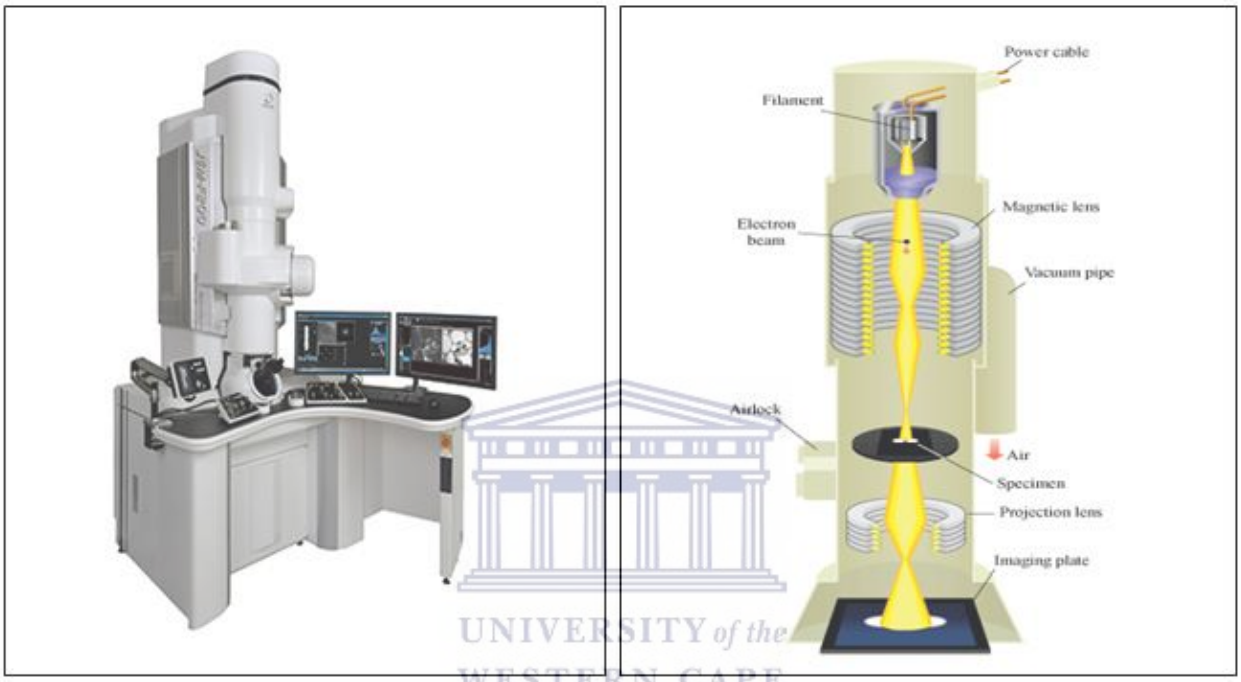

Figure 3.5 HRTEM instrument

3.3.1.2 Instrumentation

TEM contains four parts: electron source, electromagnetic lens system, sample holder and imaging system.The electron beam coming from the source is tightly focused by the electromagnetic lenses and the metal apertures. The system only allows electrons within a small energy range to pass through, so the electrons in the electron beam will have a well - defined energy. This beam falls on the sample placed in the holder. The electron beam passes through the sample. The transmitted beam replicates the patterns on the sample. This transmitted beam is projected onto a phosphor screen. In the present work, TEM images were recorded by JEOL JEM 2100F transmission electron microscope at an accelerating voltage of 200 kV. To obtain the images, the powder samples were dispersed in ethanol and it was ultrasonicated for 20 minutes. A drop of dispersion was coated onto the copper grid and TEM images were obtained (79).

3.3.1.3 Sample Preparation

HRTEM samples were prepared by dispersion of the sample materials using a spatula in a 5 ml ethanol solution. The suspension was then sonicated for 15-20 minutes. The resultant suspension was deposited on a copper grid covered by carbon film using a 10 µl micropipette to drop the suspension onto the copper grid. The ethanol was allowed to evaporate at room temperature. The specimen is required to be extremely thin (less than 100 nm), in order to allow the electrons to pass through and create an image. Samples were then mounted in a sample holder, which was introduced directly to the shaft of the microscope (HRTEM-TF 20 Model) for analysis. Experimental parameters are given as follows:

Accelerating Voltage:

- 200 KeV
- Current: 20 µA
- Objective aperture: 2
- Exposure time: 2.1seconds

3.3.2 Scanning Electron Microscopy

3.3.2.1 Principle

The scanning electron microscope (SEM) is a very useful imaging technique that utilized a beam of electrons to acquire high magnification images of specimens. The SEM maps the reflected electrons and allows imaging of thick (~ mm) samples. SEM images are formed by rastering (scanning) a beam across the sample and forming the image point - by – point (79).

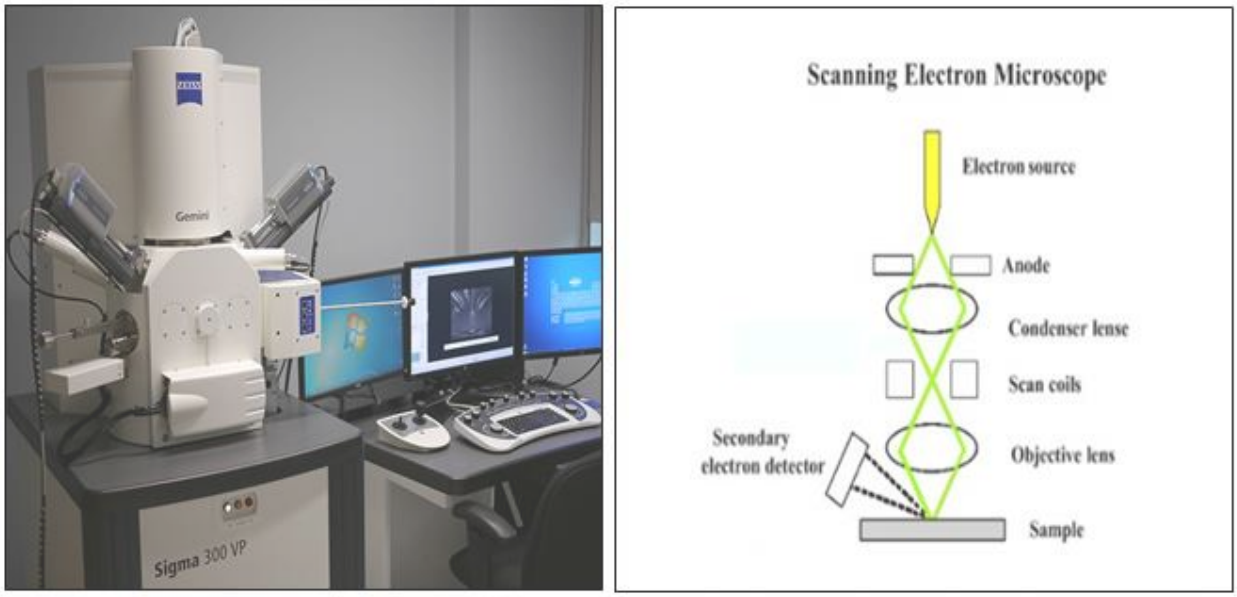

Figure 3.6 SEM instrument

3.3.2.2 Instrumentation

The SEM is an instrument that produces a largely magnified image by using electrons instead of light to form an image. A beam of electrons is produced at the top of the microscope by an electron gun. The electron beam follows a vertical path through the microscope, which is held within a vacuum. The beam travels through electromagnetic fields and lenses, which focus the beam down toward the sample. Once the beam hits the sample, electrons and X - rays are ejected from the sample. Detectors collect these X - rays, backscattered electrons and secondary electrons and convert them into a signal that is sent to a screen similar to a television screen, this produces the final image (79).

The Scanning electron microscope was used to study the surface morphology and the elemental composition of the nanomaterials, using a beam of electrons which interact on the surface of the samples. This technique creates images of the samples by scanning the nanomaterials. The samples were coated with carbon to make the surfaces electrically conductive. Scanning electron microscopy (SEM) images were analysed at an accelerating voltage of 2 kV using a TESCAN Vega TC instrument, equipped with X-ray detector for energy dispersive X-ray analysis (EDS) operated at 5 kV (79).

3.3.2.3 Sample Preparation

HRSEM samples were prepared by placing double-sided conductive carbon tape on an aluminium specimen stub. A very small amount of the sample was deposited on the specimen stub and flattened with a spatula, then gently tapped to remove the excess and loose sample.

In this study HRSEM Auriga was used with the experimental parameters listed below as:

- Working distance: 10 nm
- Accelerating Voltage: 5 KeV
- Tilt Angle: 0 degrees

Energy dispersive spectroscopy (EDS) detector which is connected to the HRSEM was used in this study to investigate the elemental composition of the samples synthesized.

3.3.3 Fourier Transform Infrared Spectroscopy

The infrared spectroscopy (IR) is one of the powerful tools for identification of compounds by matching spectrum of unknown compound with reference spectrum, identification of functional groups in unknown substances. The IR region of the electromagnetic spectrum is considered to cover the range from 50 to 12,500 cm^{-1} approximately.The functional groups present in the nanomaterials were determined and analysed with FTIR spectroscopy (80).

3.3.3.1 Principle

When infrared light is passed through a sample of organic compound, some frequencies are absorbed, while other frequencies are transmitted without being absorbed. The transitions involved in the infrared absorption are associated with the vibrational changes in the molecule. Different functional groups have different vibrational frequencies and hence the presence of these bonds in a molecule can be detected by identifying this characteristic frequency as an absorption band in the infrared spectrum. The plot between transmittance against frequency is called infrared spectrum (80).

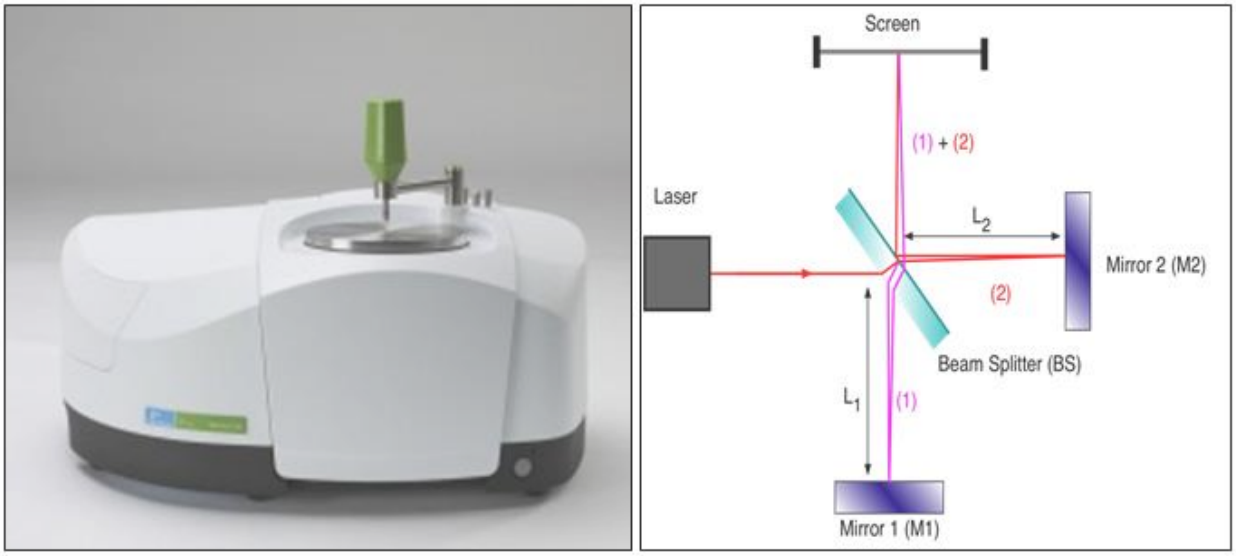

Figure 3.7 FTIR instrument

3.3.3.2 Instrumentation

There are three basic spectrometer components in an FT system: radiation source, interferometer and detector. The IR radiation from a broadband source is first directed into an interferometer, where it is divided and then recombined after the split beams travel different optical paths to generate constructive and destructive interference. Next, the resulting beam passes through the sample compartment and reaches to the detector. The sample to be analyzed should be ground into KBr matrix or dissolved in a suitable solvent. Water should be removed from sample if possible. In case of solid samples, it is mixed with solid, then ground and pressed. Fourier Transform Infrared measurements (FTIR) were performed using Perkin Elmer FTIR spectrophotometer by standard KBr pellet technique (80).

3.3.3.3 Sample Preparation

The samples were prepared by mixing the nanomaterials with KBr, a small amount of the samples were placed on a ATR sampling accessory and pressed. The samples were analyzed at a wavelength range of 400 cm^{-1} to 4000 cm^{-1}.

3.3.4 Ultraviolet and Visible Spectroscopy

This refers to absorption spectroscopy in the ultra-violet and visible spectral region. In this region of the electromagnetic spectrum, molecules undergo electronic transition. When sample molecules are exposed to light having an energy that matches a possible electronic transition within the molecule, some of the light energy will be absorbed as the electron is promoted to a higher energy orbital. An optical spectrometer records the wavelengths at which absorption occurs, together with the degree of absorption at each wavelength. The resulting spectrum is presented as a graph of absorbance versus wavelength. The optical properties of materials can be studied with the help of UV - Vis spectra (81).

3.3.4.1 Principle

The absorbance of light by molecules in the solution is based on the Beer - Lambert law, $A=\log\frac{Io}{I}$ = □ x b x c,where, *I0* is the intensity of the reference beam and *I* is the intensity of the sample beam, □ is the molar absorbtivity with units ofL mol^{-1} cm - 1, *b* = path length of the sample in centimeters and *c* = concentration given solution expressed in mol L^{-1} (81).

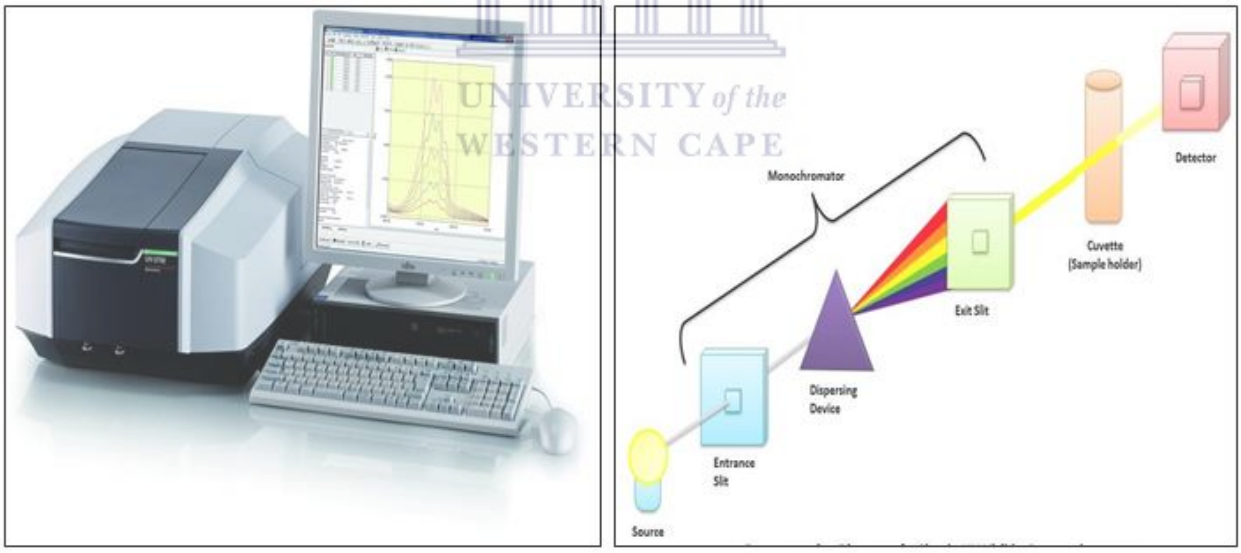

Figure 3.8 UV-Vis Spectroscopy instrument

3.3.4.2 Instrumentation

The main components of the UV-Vis spectrometers are a light source, double beams,a monochromator, a detector and a recording device. The source is usually a tungsten filament lamp for visible and deuterium discharge lamp for UV measurements. The light coming out of the source is split into two beams. The sample and reference cells are rectangular quartz containers; they contain the solution to be tested and pure solvent, respectively. The spectrometer records the ratio between the reference and sample beam intensities. The recorder plots the

absorbance against the wavelength. The sample is prepared into a paste and then dissolved into the solvent to make a dilute sample solution. This sample solution is filled up to mark line of the sample cell (81).

3.3.4.2 Sample Preparation

Diffuse reflectance spectra of the synthesized nanomaterials were obtained using UV-Vis spectrophotometry, in a wavelength of 200 nm to 800 nm. In this analysis ethanol was used as reference, with 0.05g of the samples mixed with the reference. This technique was used to determine the absorbance, reflectance and the band gap of the materials. The respective band gap of each sample was calculate from the KubelkaMunk equation.

$$K = \frac{(1-R)^2}{2R} \quad (3.1)$$

Where R is the reflectance, while K is proportional to the extinction coefficient. The graph of $[Khv]^2$ $(eV)^2$ was plotted against hv (eV), in order to determine the band gap of each nanocomposite.

3.3.5 X-ray Diffraction

X - ray diffraction technique is used for the determination of structure and crystallainity and material identification. XRD is an apt method to examine whether a resultant material has amorphous or crystalline nature. Crystalline phases can be identified by just comparing the interplanar distance '*d*' values obtained from XRD data with the fundamental data in Joint Committee on Powder Diffraction Standards (JCPDS).

3.3.5.1 Principle

X - ray diffraction is based on constructive interference of monochromatic X - rays from a crystalline sample. The X - rays, generated by a cathode ray tube are filtered to produce monochromatic radiation, collimated and directed towards the sample. X - ray primarily interact with electrons in atoms, collide and some photons from the incident beam are deflected away from original. The X - rays interfere constructively and destructively producing a diffraction pattern on the detector. The incident X - ray radiation produces a Bragg peak if their reflections from the various planes interfered constructively (82).

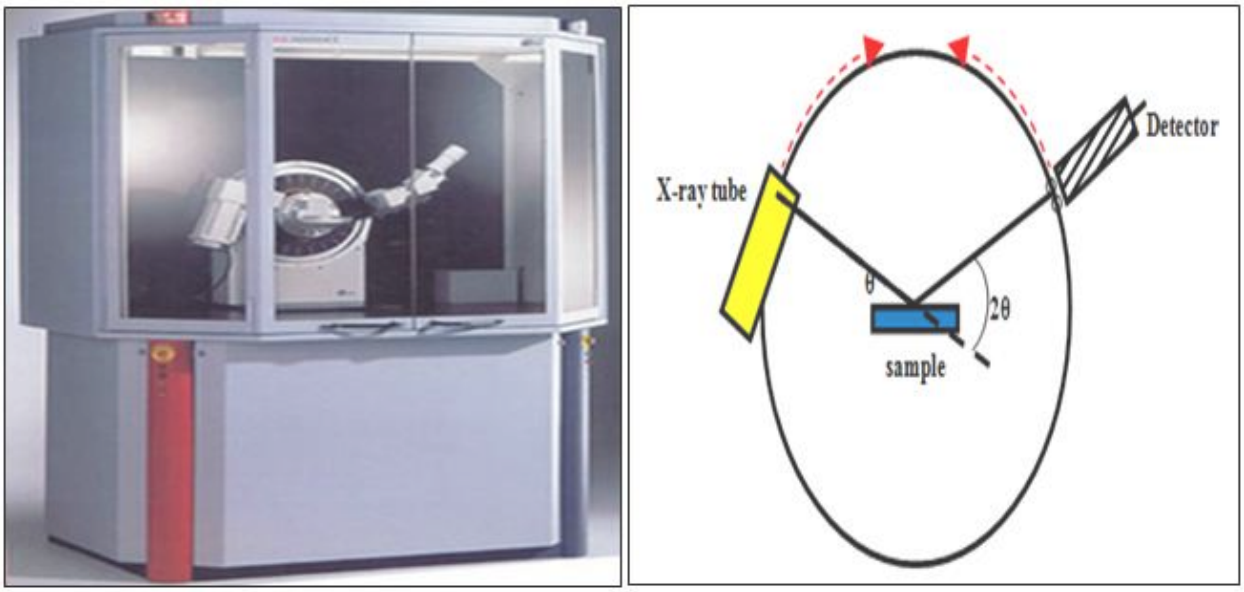

Figure 3.9 XRD instrument

3.3.5.2 Instrumentation

A typical powder X - ray diffractometer consists of a source of radiation, a monochromator to choose the wavelength, slits to adjust the shape of the beam, a sample and a detector. A goniometer is used for fine adjustment of the sample and the detector positions. The goniometer mechanism supports the sample and detector, allowing precise movement. The specific wavelengths are characteristic of the target material (Cu, Fe, Mo, Cr). Monochromators and filters are used to absorb the unwanted emission with wavelength K_β, while allowing the desired wavelength, K_α to pass through. The X - ray radiation most commonly used is that emitted by copper, whose characteristic wavelength for the K_α radiation is equal to 1.5418 Å. The filtered X- rays are collimated and directed onto the sample (82).

When the incident beam strikes a powder sample, diffraction occurs in every possible orientation of 2Θ. The diffracted beam may be detected by using a moveable detector such as a Geiger counter, which is connected to a chart recorder. The counter is set to scan over a range of 2Θ values at a constant angular velocity. Routinely, a 2Θ range of 5 to 70 degrees is sufficient to cover the most useful part of the powder pattern. A detector records and processes this X - ray signal and converts the signal to a count rate which is then fed to a device such as a printer or computer monitor. The sample must be ground to fine powder before loading it in the glass sample holder. Sample should completely occupy the square glass well (82).

The XRD measurememts were carried out using an X'Pert Philips instrument, coupled with Cu Kα radiation polychromatic beam. The instrument operates at 40kV and 40 mA with a wavelength of 1.5401510 nm. The powder nanomaterial were mounted on a sample holder and scanned at a range of $0^o \leq 2\theta \leq 90^o$.

3.3.5.3 Sample Preparation

In the XRD analysis, dry samples were mounted in plastic sample holders and the surface was flattened to allow maximum X-ray exposure. Experimental parameters for XRD analysis are given as follows:

- X-ray Diffractometer: Bruker AXS D8 Advance from Ithemba labs.
- Tube: Copper
- Detector: Sodium Iodide
- Monochromator: Graphite
- Electron Intensity: 40 kV
- X-ray Source: CuKα (λ= 1.5418Å)
- Current: 40 mA
- Scan Range: 10o **<** 2θ **<** 100

3.3.6 Raman Spectroscopy

Raman spectroscopy is a method of determining modes of molecular vibrations. It is predominantly applicable to qualitative and quantitative analyses of covalently bonded molecules used to distinguish between different phases of the same material and can provide information on strain and periodicity in modulated structures. It is used extensively to characterize semiconductor surfaces(82).

3.3.6.1 Principle

Raman signal occurs due to the change in polarizability of a molecule. This is a measure of the deformability of a bond in an electric field. The Raman effect is not an absorption effect like infrared, but depends on the polarizability of the vibrating group (82).

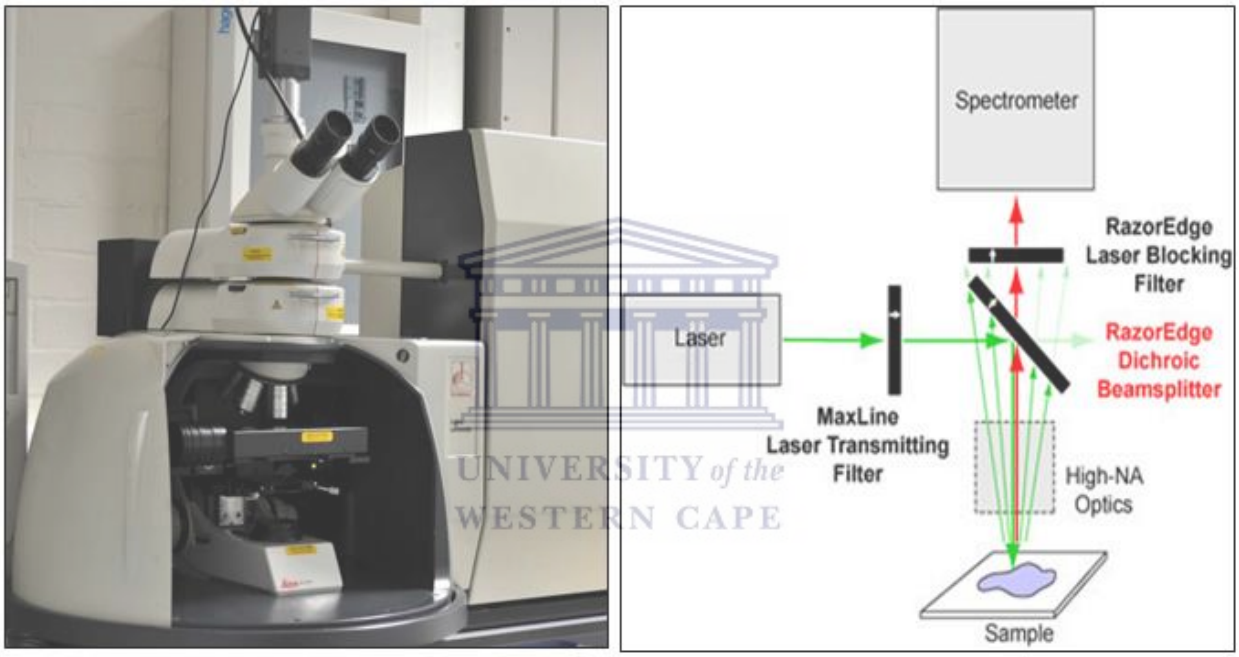

Figure 3.10 Ramanan instrument

3.3.6.2 Instrumentation

A Raman system typically consists of four major components: Excitation source laser, Sample illumination system, light collection optics, Wavelength selector, Detector. The sample is normally illuminated with a laser beam in the ultraviolet (UV), visible (Vis) or near infrared (NIR) range. Scattered light is collected with a lens and is sent through interference filter or spectrophotometer to obtain Raman spectrum of a sample. Raman spectra are obtained from bulk solids, liquids, tablets, polymers, paper. Sample preparations, such as grinding can also lead to changes in solid states, for example hydration state, polymorphism and hydrogen bonding which sometimes have an impact on the final detection method (82).

3.3.6.3 Sample Preparation

The samples were ground to fine powder, and then placed on a glass plate. The spectra were recorded over a range of 50 to 3270 cm-1 using an operating spectral resolution of 2.0 cm^{-1}. The spectra were averaged with 20 scans, at an exposure time of 4 s.

3.3.7 Electrochemical Techniques

3.3.7.1 Cyclic Voltammetry

Cyclic voltammetry (CV) is a type of potential-controlled electrochemical technique, which can be used to examine the electrodes surface reactions, the behaviour of the electrochemically-active species, and to investigate the quality of electrocatalysts. Cyclic voltammetry provides information on the thermodynamics of redox processes and kinetics of heterogeneous electron transfer reactions. It plays an integral role in the comprehensive characterization of nanophase electrocatalysts (84).

3.3.7.1 Principle

In cyclic voltammetry the potential of the working electrode is swept linearly with time and between two potential ends. By adjusting the potential of the working electrode, electrons are transferred between the electrode and the molecules in the electrolyte, which records the current response of the working electrode when the potential is swept back and forth between two selected potentials (84).

Figure 3.11 CV instrument

3.3.7.1.2 Instrumentantation

The experiments were conducted in a three electrode cell, connected to a Metrohm Autolab. The three electrodes are the GCRD electrode tip as the working electrode, Pt wire as the counter electrode and Ag/AgCl as the reference electrode. 0.1 M HClO4 was used as the electrolyte of choice as perchloric acid which is known for its low anion adsorption on Pt and is also expected to simulate the perfluorosulfonic acid (PFSA) membranes more closely than sulphuric or phosphoric acid [94]. The potential was applied with an Autolab potentiostat PGSTAT 30 (name of the Autolab model) and the experiments were controlled with General Purpose Electro-chemical System (GPES) software. All experiments were carried out at room temperature (23. 2^{o} C). Prior to measurements, the electrolyte was purged with nitrogen gas for 45 minutes to remove dissolved oxygen, and the surface of the electrode was then conditioned by scanning the potential between -0.2 and 0.9 V for 20 cycles at 100 mV/s vs. Ag/AgCl. This conditioning of the working electrode is done to remove any impurities on the surface of the electrode as well as to attain stable voltammograms. After conditioning the working electrode, the electrolyte was purged again with nitrogen gas for 30 minutes to ensure that it was saturated with nitrogen before scanning the potential between -0.2 and 0.9 V for three cycles at 20mV/s vs. Ag/AgCl; the three cycles were then used to study the electrochemical behaviour of the prepared nanomaterials (84).

Cyclic voltammetry technique was used to determine information about the electron transfer kinetics, thermodynamics as well as the consequences of elctron transfter.The electrochemical reaction of interest takes place at the working electrode. The faradiac current at the working electrode is transduced to a potential output. The CV response is plotted as current versus potential. During the forward sweep the oxidized form is reduced, while on the reverse sweep the reduced form near the electrode is re-oxidized (84).

3.3.7.2 Impedance

Electrochemical Impedance Spectroscopy (EIS) is a technique which has been utilised by many institutions for over a century for purposes such as corrosion analysis adsorption properties of molecules (interfacial behaviour) and also used to monitor the functioning of batteries and fuel cells amongst many other applications. The technique is based upon complex mathematical transforms first described in the late 19th century by Oliver Heaviside to yield real values of impedance in temporal space. As a respected mathematician, Heaviside is also credited with the invention of terminologies such as impedance,admittance and conductance. Critically, he defined

the ‘operational impedance’ as the “complex ratio of the voltage and current in an AC circuit”, which is denoted as:

$$Z(j\omega)\frac{V(j\omega)}{I(j\omega)}$$

Where, Z is the impedance, V is the voltage, I is the current, j is the imaginary component and ω is the frequency. The subsequent development of impedance in relation to diffusional electrochemical systems was first reported by Warburg in 18991 and the principles have been implemented increasingly to the present day to the point where EIS has now branched away from universities and into industry for quality control purposes (paints, emulsions, corrosion). In fact, almost any process which changes the conductivity of a system can be recognised by EIS, hence a multitude of properties can be elucidated using the technique (85).

3.3.7.2.1 Principle

In principle, impedance is the opposition force to electrical current in a circuit and is measured in the same units as resistance, Ω. However resistance differs from impedance because resistance obeys Ohm's law, and is observed in DC circuits where the resistance is technically the impedance with zero phase angle, since the current is not alternating. The concept of resistance can only be applied in an AC circuit if certain criteria are met: (i) the AC voltage and current must be in phase with each other; (ii) the resistance is frequency-independent; and (iii) the resistance can be applied to all currents and voltages. Unfortunately in the vast majority of cases the phase angle is not equal to zero, as capacitative and/or inductive effects are observed at almost all frequencies (vide infra), hence a more general principle must be used to account for frequency dependence; the concept of impedance essentially allows a quantitative representation of the opposition force to electrical current in these cases (as in AC circuits) (85).

3.3.7.2.2 Instrumentation

In the majority of EIS experiments, a fixed sinusoidal voltage is applied by a potentiostat across a three electrode cell containing a solution of electrolyte harbouring the molecule under investigation. The amplitude and load of the fixed sinusoidal voltage should be dependent upon the type of molecular system under investigation; biological molecules tend to be subject to smaller voltages than non-biological ones as the structures of the biological molecules are easily denatured this way (85).

EIS requires manipulation of complex numbers to deduce true values for the impedance. This is achieved by the software in which the user selects to obtain impedance spectra.The data can be presented in a variety of ways, for instance real and imaginary impedance components are plotted against one another in Nyquist plots which have to be interpreted properly to deduce

solution resistances, charge transfer resistances and Warburg impedance as well as time constants, whereas in Bode plots, the impedance and phase angle is plotted against frequency which can be helpful find capacitative or inductive effects of electrochemical systems (85).

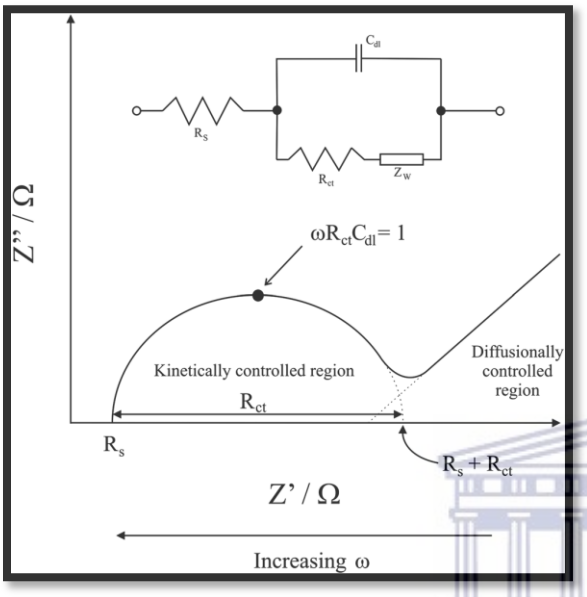

Figure 3.12: Simple Randles equivalent circuit for an electrochemical cell (85).

3.3.7.3 Chronopotentiometry

The term chronopotentiometry refers to an electrochemical technique in which a controlled current, usually a constant current, is caused to flow between two electrodes; the potential of one electrode is monitored as a function of time with respect to a suitable reference electrode. The solution is usually, but not necessarily, unstirred and contains an excess of a supporting electrolyte so that diffusion is the principal mechanism of mass transport. The current in chronopotentiometry is sufficiently large that the current efficiency for the reduction of the species of interest falls below 100%, usually within a few seconds.(86).

3.3.7.3.1 Principle

In chronopotentiometry, a current pulse is applied to the working electrode and its resulting potential is measured against a reference electrode as a function of time. At the moment when the current is first applied, the measured potential is abruptly changed due to the iR loss, and after that it gradually changes, because of a concentration overpotential that is developed, as the

concentration of the reactant is exhausted at the electrode surface. If the current is larger than the limiting current, the required flux for the current cannot be provided by the diffusion process and, therefore, the electrode potential rapidly rises until it reaches the electrode potential of the next available reaction, and so on (86).

3.3.7.3.2 Technique

The different types of chronopotentiometric techniques are depicted in **Figure 3.6**. In constant current chronopotentiometry, the constant anodic/cathodic current applied to the electrode causes the electroactive species to be oxidized/reduced at a constant rate. The electrode potential accordingly varies with time as the concentration ratio of reactant to product changes at the electrode surface. This process is sometimes used for titrating the reactant around the electrode, resulting in a potentiometric titration curve. After the concentration of the reactant drops to zero at the electrode surface, the reactant might be insufficiently supplied to the surface to accept all of the electrons being forced by the application of a constant current. The electrode potential will then sharply change to more anodic/cathodic values. The shape of the curve is governed by the reversibility of the electrode reaction (86).

The applied current can be varied with time, rather than being kept constant. For example, the current can be linearly increased or decreased and can be reversed after some time. If the current is suddenly changed from an anodic to cathodic one, the product formed by the anodic reaction (i.e., anodic product) starts to be reduced. Then, the potential moves in the cathodic direction as the concentration of the cathodic product increases. On the other hand, the current is repeatedly reversed in cyclic chronopotentiometry (86).

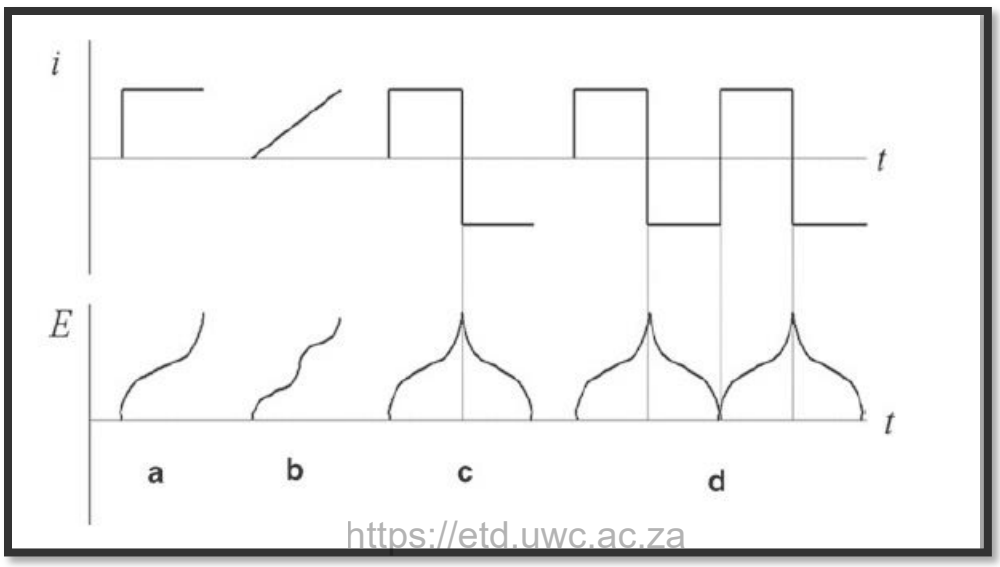

Figure 3.13 Different types of chronopotentiometric experiments. (a) Constant current chronopotentiometry. (b) Chronopotentiometry with linearly rising current. (c) Current reversal chronopotentiometry. (d) Cyclic chronopentiometry(86).

CHAPTER FOUR

RESULTS AND DISCUSSION

4 INTRODUCTION

The characterization of materials is important for understanding their properties and applications. This chapter discusses the results obtained from the instrumental testing of the synthesized TiO_2 nanocomposites. The techniques adopted to characterize the nanoparticles are: X - ray diffraction, UV-Visible spectroscopy, Fourier transform infrared spectroscopy, Raman spectroscopy, Scanning electron microscopy, Transmission electron microscopy, Cyclic Voltammetry, Impedance spectroscopy and Chronopotentiometry.

4.1 CHARACTERIZATION OF GRAPHENE MATERIALS

The prepared graphene materials include: Graphene oxide, reduced graphene oxide, nitrogen doped graphene oxide and nitrogen doped reduced graphene oxide. The materials are characterised using FTIR, XRD, Raman, UV-Vis, Cyclic Voltammetry and Impedance Spectroscopy .

4.1.1 FTIR ANALYSIS

The infrared spectroscopy (IR) is one of the powerful tools for identification of compounds by matching spectrum of unknown compound with reference spectrum, identification of functional groups in unknown substances. The resulting spectrum represents the molecular absorption and transmission, creating a molecular fingerprint characteristic of the sample of interest. This technique holds great reliability because no two samples can have the same fingerprint (81).

4.1.1.1 FTIR OF GRAPHENE NANOMATERIALS

FTIR spectra analysis was performed to investigate the structure and functional groups of the graphite, graphene oxide, graphene and nitrogen doped graphene materials, as shown in **Figure 4.1** and **4.2**.

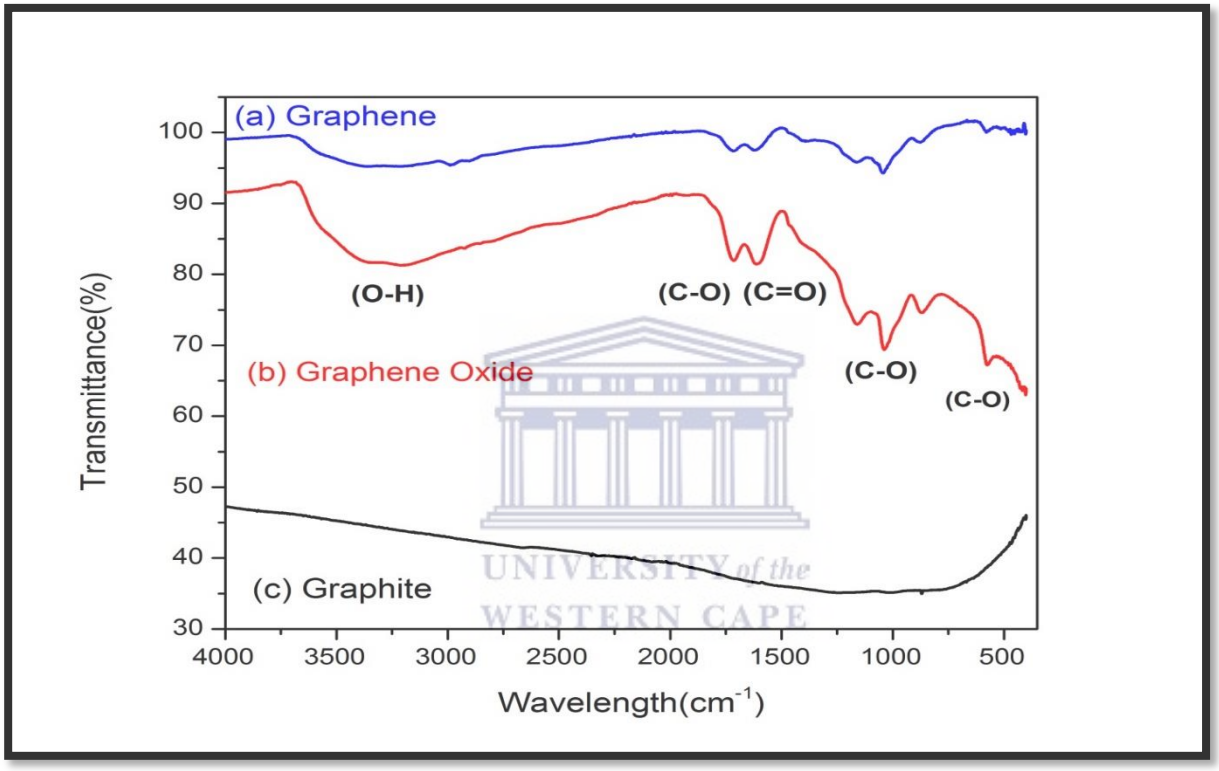

Figure 4.1: FT-IR spectrum of graphene, graphene oxide and graphite.

The FT-IR spectrum of GO shown above confirms the introduction of oxygen containing groups such as functional hydroxyl, epoxy and carboxylic groups upon oxidation of graphite. The band about 1688 cm^{-1} is attributed to stretching vibration modes of C=O in carboxylic acid and carbonyl groups. The strong band at 1060 cm^{-1} is assigned to C–O groups. The strong peak around 3450 cm^{-1} is attributed to the O–H stretching vibrations of the C–OH groups and water. The Strong peak at 3450 cm -1 in graphene was found to have decreased in transmittance, which supports the reduction process.

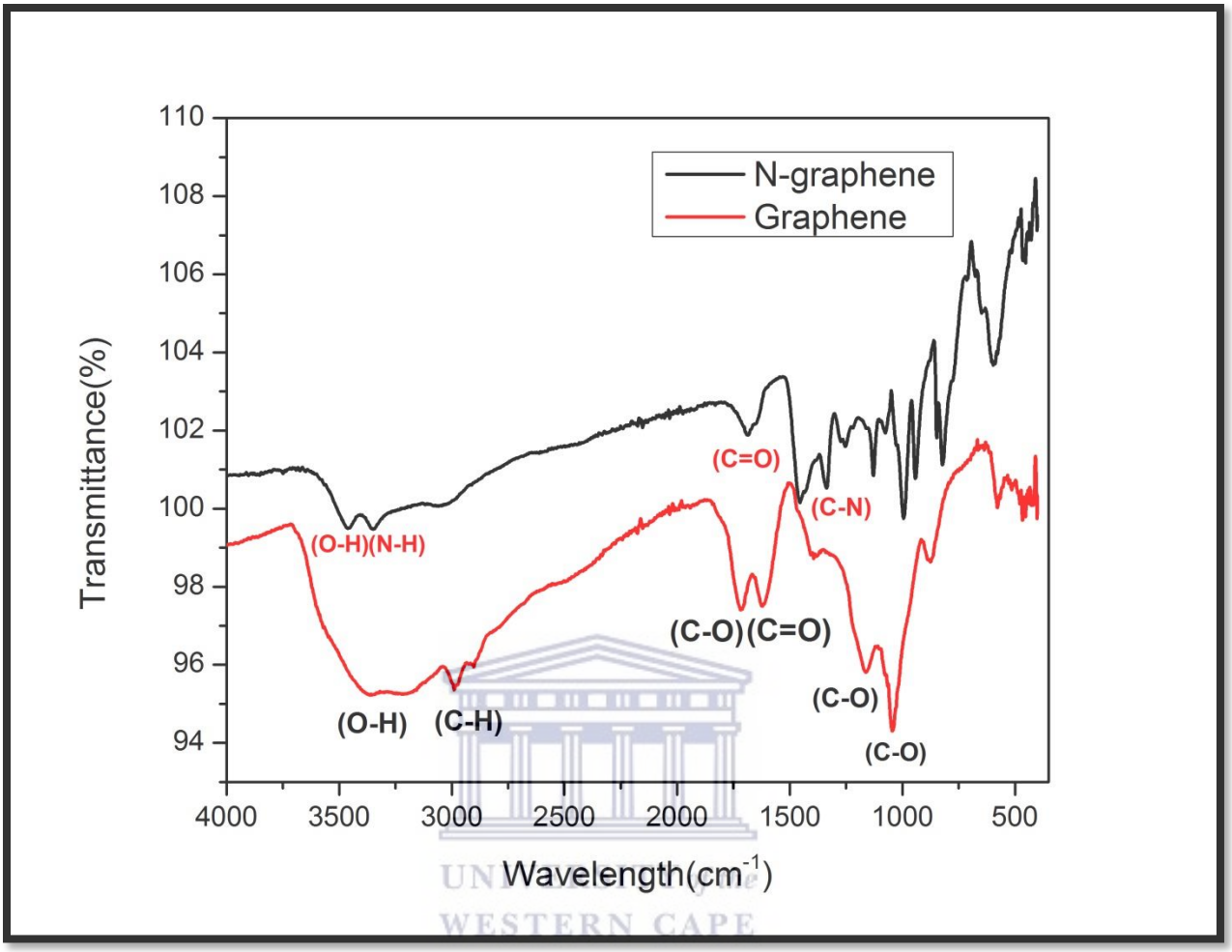

Figure 4.2: FT-IR spectrum of graphene and nitrogen doped graphene.

Figure 4.2 represent the spectra of nitrogen doped graphene and graphene, the presence of nitrogen can be attributed by the N-H and C-N bond at 3560 cm^{-1} and 1750 cm^{-1} respectively, in the nitrogen doped graphene spectrum. The reduction of the O-H group is greatest at the N-graphene as indicated by the transmittance difference of the two O-H groups in the spectrums.

4.1.2 RAMAN ANALYSIS

Raman spectroscopy is a method of determining modes of molecular vibrations. It is predominantly applicable to qualitative and quantitative analyses of covalently bonded molecules, which are used to distinguish between different phases of the same material and can provide information on strain and periodicity in modulated structures. It is used extensively to characterize semiconductor surfaces. Raman signal occurs due to the change in polarizability of a molecule. This is a measure of the deformability of a bond in an electric field (89).

4.1.2.1 GRAPHENE AND GRAPHENE OXIDE NANOMATERIALS

Raman spectra can be used to characterize single layer and multiple layer graphene samples. The D* Raman scattering mode at about 2820 cm^{-1} can be used to identify the change in electronic structure between single and multiple layer samples of graphene. As the sheet thickness increases, the narrow and symmetric peak becomes asymmetric on the high-energy side (86). Typical Raman spectra of graphene samples are shown in **Figure 4.3**.

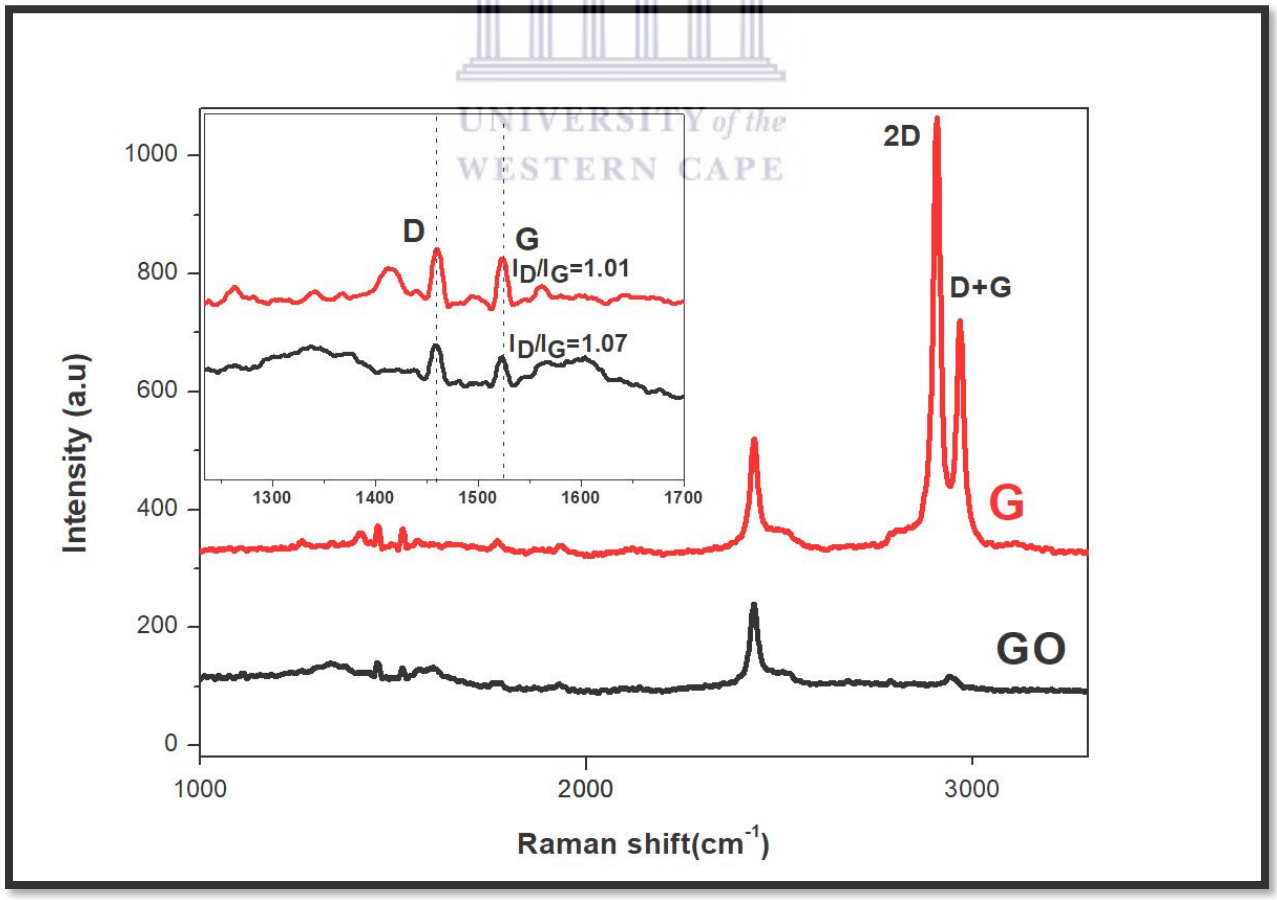

Figure 4.3: Raman spectrum of graphene and graphene oxide.

Raman spectroscopy was used to characterize the structures of graphene by comparing G and D bands. The G band corresponds to the E_2g mode with characteristics of sp2 bonding, while the D band is attributed to the defects and disordered nature of graphene sheets. **Figure 4.3** shows the comparison of Raman spectra for graphene oxide and graphene. The Raman spectrum of GO shows two absorption bands at 1444 cm^{-1} and 1529 cm^{-1} corresponding to D and G bands, respectively. An upshift of the G mode from 1529 cm^{-1} can be used to detect charge doping or compressive strain. The difference in the G-band frequency of the graphene samples is attributed to the relative strength of fold induced electron renormalization. During reduction, the characteristic D band of G shifted to a higher number. The ID/IG ratio was used to measure structural disorder during the reduction of GO to rGO , which was slightly increased from 1.01 to 1.07. As a result, the formation of defects occurs in as a result of the removal of oxide functional groups attached to the GO surface (88).

4.1.3 XRD ANALYSIS

X - ray diffraction technique is the most common and efficient method for the determination of structure and crystallinity and material identification. XRD is used to examine whether a resultant material has amorphous or crystalline nature. Crystalline phases can be identified by just comparing the inter-planar distance‘d’ values obtained from XRD data with the fundamental data in Joint Committee on Powder Diffraction Standards (JCPDS).

4.1.3.1 XRD OF GRAPHENE NANOMATERIALS

The synthesised few-layer graphene oxide, reduced graphene, nitrogen doped graphene oxide and nitrogen doped reduced graphene oxide, were structurally and chemically investigated by the X-ray diffraction (XRD) technique, **Figure 4.4** shows the diffraction pattern of graphite and **Figure 4.5** shows the diffraction pattern of graphene oxide and graphene, while **Figure 4.6** shows the diffraction pattern of graphene and N-graphene.

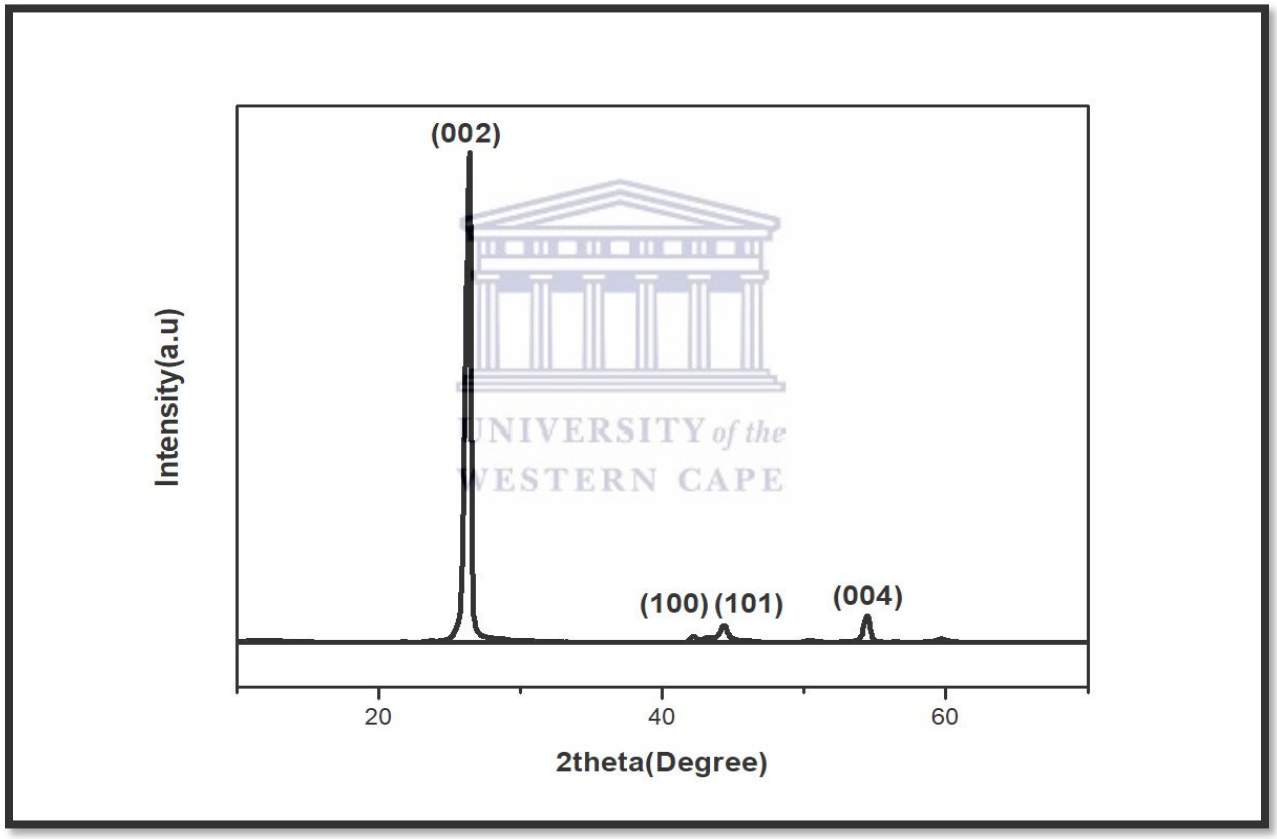

Figure 4.4: The diffraction pattern of graphite.

The diffraction pattern of graphite pattern exhibits several peaks located at 2θ angle of 26.12 degree, 42.06 degree, 44.05degree and 54.27 degree respectively, corresponding to the crystal phase of (002), (100), (101) and (004) respectively. All the peaks in the XRD correspond to the graphite phase according to the JCPDS: 01-075-1621.

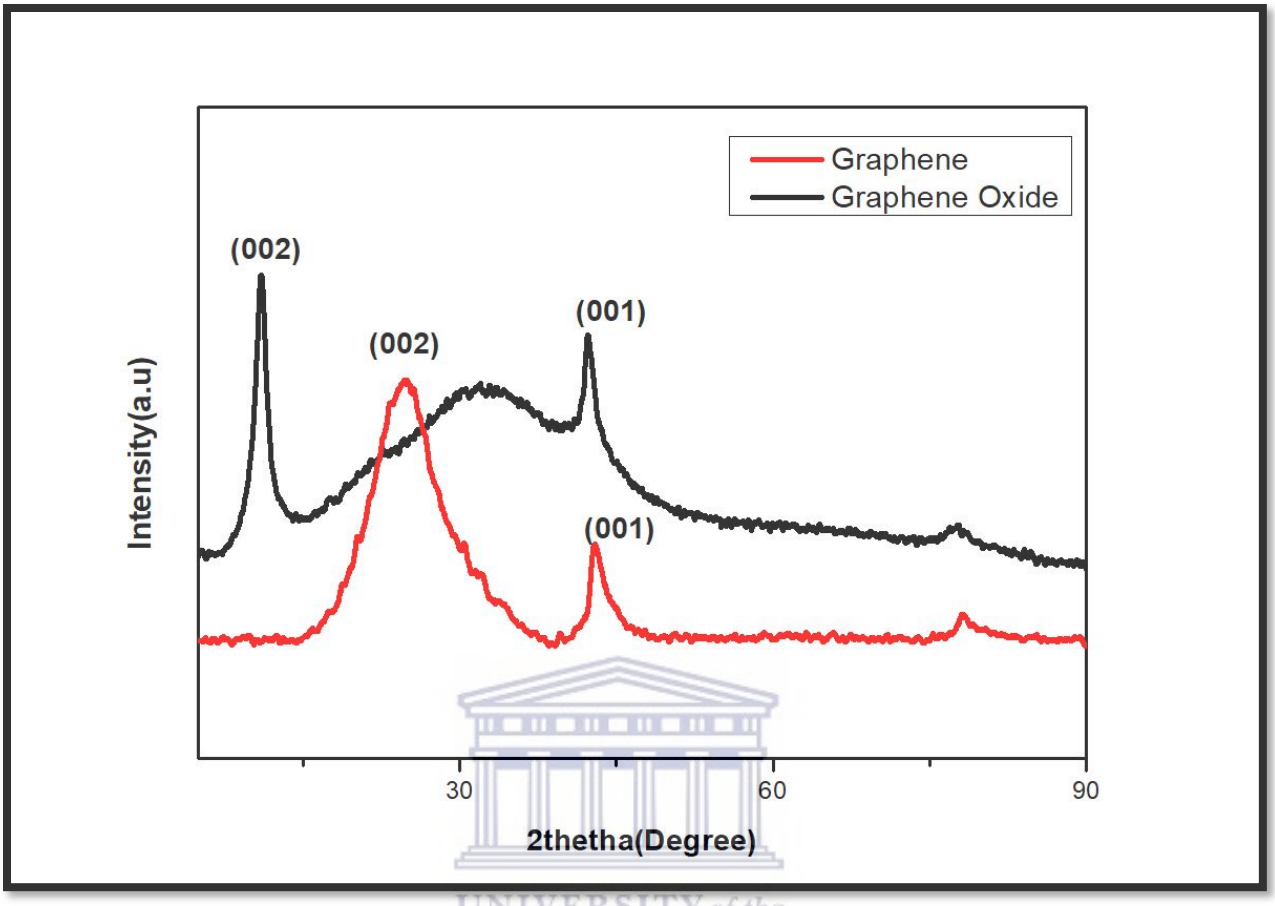

Figure 4.5 The diffraction pattern of graphene oxide and graphene.

The broad band for graphene oxide obtained at 10.67 degree corresponding to an interlayer distance of 0.41 nm and has been assigned to the (002) reflection plane, which confirms the formation of graphene oxide by the oxidation of natural graphite using modified Hummer's method. The diffraction peak at 42.21 degree corresponds to the (001) orientation which could be due to the incomplete oxidation of graphite materials. Graphene oxide has a higher interlayer distance due to the introduction of oxygen functional groups and water molecules between the graphene layers. The reduction of graphene oxide to reduced graphene oxide is also confirmed by the XRD analysis (83).

It is evident from the XRD analysis that the sharp peak observed at 10.67 degree disappeared and shifted to 24.54 (002) plane, thereby confirming the reduction of graphene oxide. The shift in the diffraction peaks from graphene oxide to reduced graphene oxide decreases the interlayer distance of graphene layers, which may due to the removal of oxygen functional groups, resulting in restacking of the reduced graphene oxide sheets. (85)

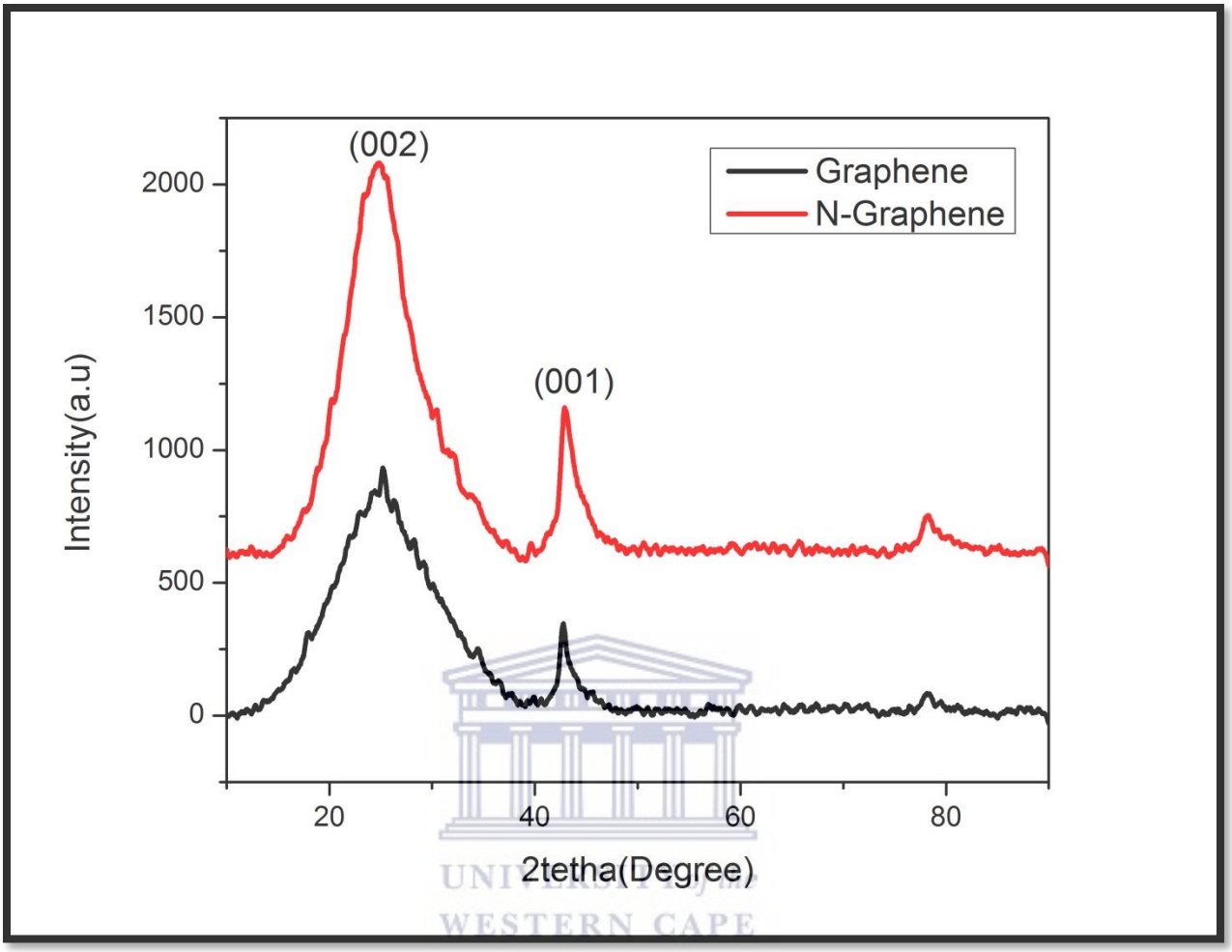

Figure 4.6: XRD pattern of graphene and nitrogen doped graphene.

Figure 4.6 shows the XRD spectrum of graphene and nitrogen doped graphene. The graphs share similar diffraction patterns, where the (002) and the (001) faces are approximately at 24 and 43 degree respectively. The graph of N-graphene shares greater intensity compared to that of graphene.

4.1.4 UV –VIS SPECTROSCOPY ANALYSIS

UV-vis Spectroscopy refers to absorption spectroscopy in the ultra-violet and visible spectral region. In this region of the electromagnetic spectrum, molecules undergo electronic transition. When sample molecules are exposed to light having an energy that matches a possible electronic transition within the molecule, some of the light energy will be absorbed as the electron is promoted to a higher energy orbital.

4.1.4.1 UV SPECTRUM OF GRAPHENE NANOCOMPOSITES

The UV-Vis spectrums of graphene nanocomposites were determined, **Figure 4.7** shows the absorbance spectrum of graphene oxide and graphene, while **Figure 4.8** shows the absorbance spectrum of graphene and N-graphene.

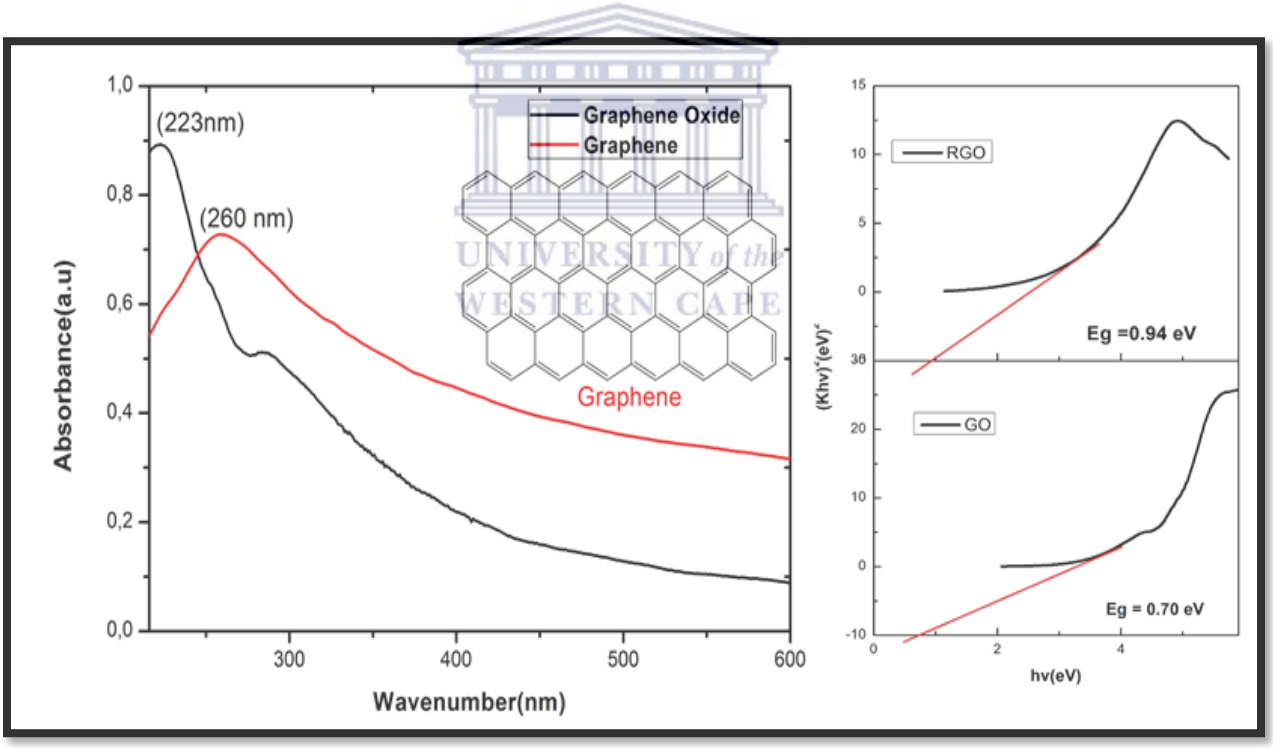

Figure 4.7: UV spectrum of graphene oxide and graphene.

The absorption spectrum of graphene oxide (GO) and graphene are shown in **Figure 4.7.** Two kinds of characteristic features were observed in the spectra of GO, that confirms the identity of the molecule. The first is a shoulder at wavelength 280 nm, corresponding to an n-π^* transition of the C=O bond. Another characteristic feature is the absorption peak that appears at 223 nm, and this corresponds to a π-π^* transitions of the sp^2 carbon double bonds. A red-shift occurs during

the reduction of graphene oxide to graphene, which shifts the sp^2 carbon double bonds to a longer wavelength of 260nm. This increases the π conjugation, as the π conjugation increases less energy is required for the transition, which corresponds to the observed shift of the absorption from graphene oxide to graphene. The band gap of GO is reported to be 0.70 eV, however reduction of graphene oxide to graphene increased the band gap to 0.94 eV.

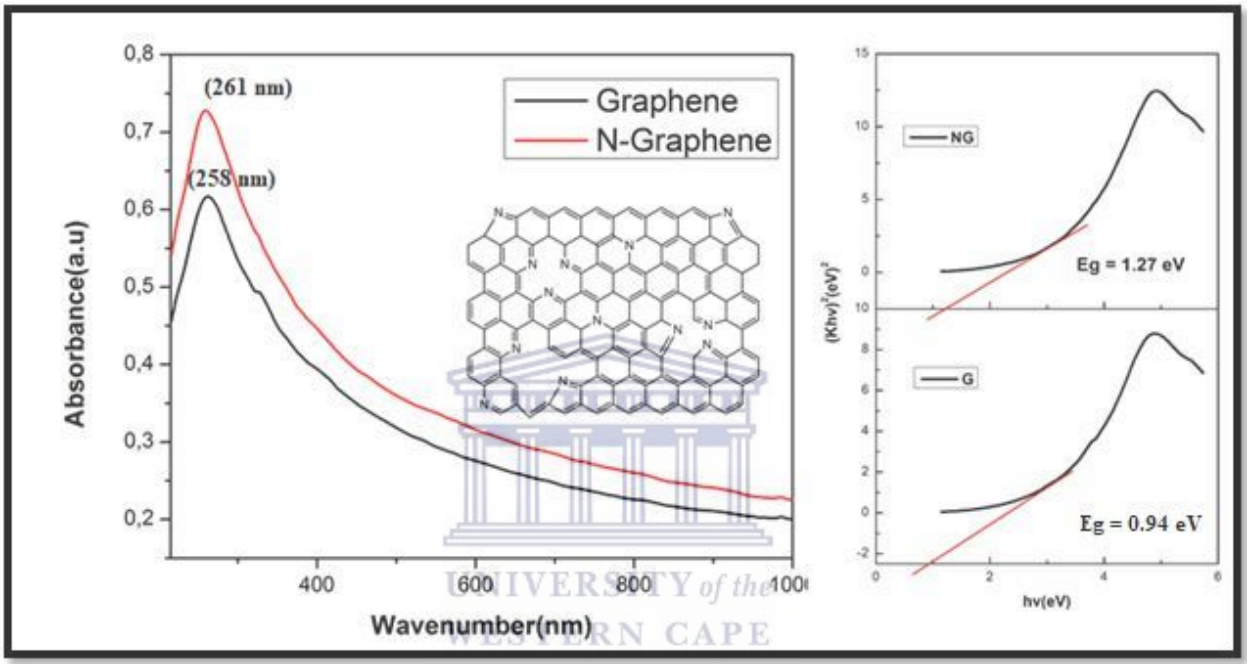

Figure 4.8 shows the UV spectrum of graphene and nitrogen doped graphene.

The nanomaterials went through a red-shift when being reduced from graphene oxide and N-graphene oxide, where the absorption occurred in the wavelength of 270 and was greatest for nitrogen doped graphene. N-graphene experienced a greater absorbance compared to graphene as illustrated in **Figure 4.8**.

4.1.5 Electrochemical Analysis

4.1.5.1 CYCLIC VOLTAMMETRY ANALYSIS

The electrochemical properties of GO, RGO and N-G materials were investigated by preparing the graphene samples as electrode materials and characterizing them using Cyclic Voltammetry. **Figure 4.9** gives the curves of the three electrodes at a scan rate of 30 mV/s and a potential window of 0.4 V to - 0.8 V.

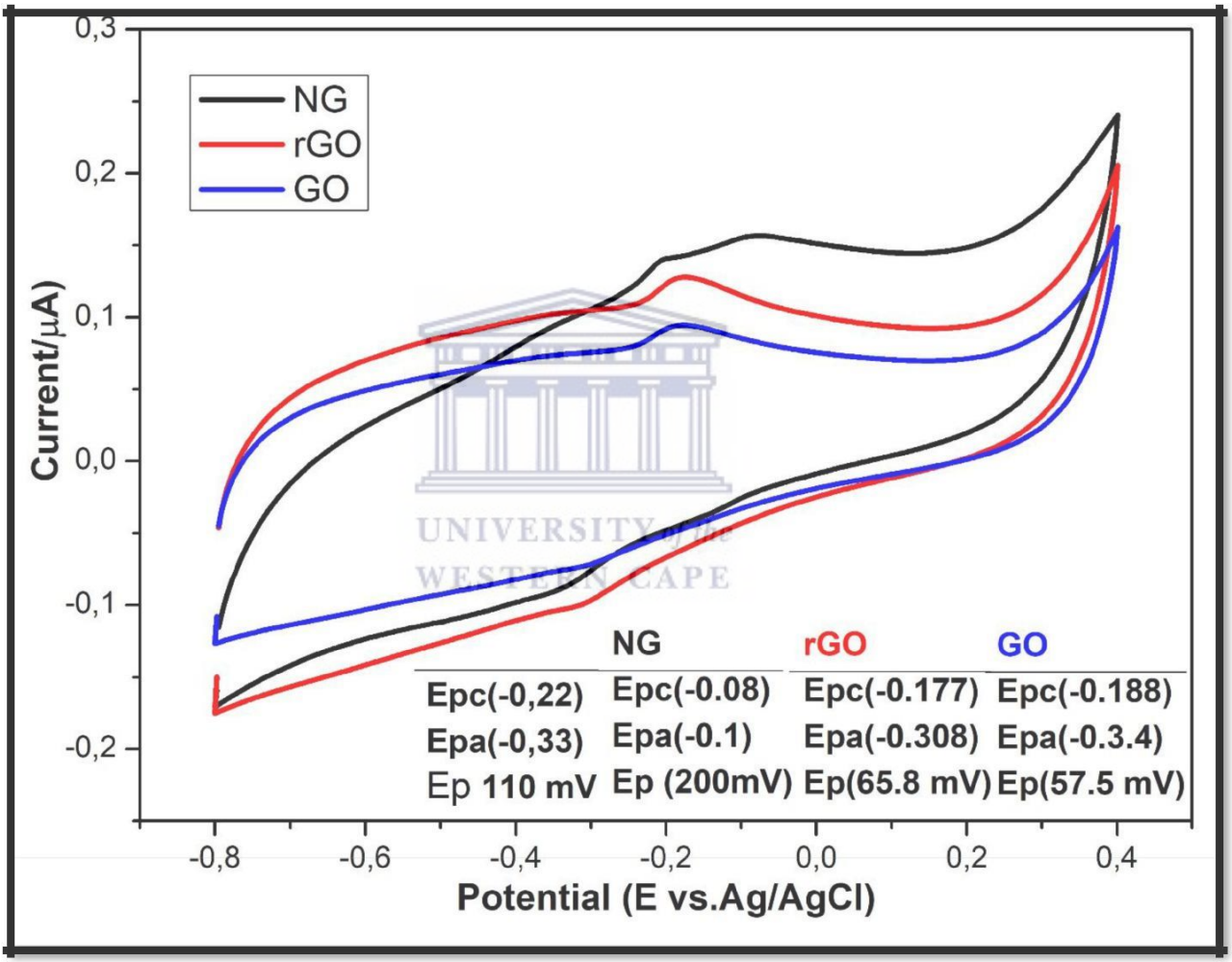

Figure 4.9: Cyclic voltammograms of GO, rGO, and N-G in K_3[Fe(CN)6] at 30 mV/s.

It was observed that the cyclic voltammograms of both rGO and GO show a 1-electron reversible reaction with the oxidation peak centred at a potential of -0.1 V and the reduction peak at a potential of -0.3 V. This implies that reduction of GO has no effect on the electrochemical properties of graphene, rGO. However, doping graphene with nitrogen decreases the rate of electron flow in the system, hence the appearance of a 2-electron reversible reaction with the oxidation peaks at -0.2 mV and -0.08 mV and the reduction peak potentials at – 0.1 mV and -0.2 mV. The decrease in the rate of electron flow can be attributed to the increase in band gap of N-doped graphene compared to graphene oxide and graphene. The separations between anodic and cathodic peak were (110 mV, 200 mV), (65.5 mV) and (57.5 mV) for N-graphene, graphene and GO respectively. N-graphene is observed to have the largest separation between the anodic and cathodic peak due to slow electron kinetics.

4.1.6 IMPEDANCE SPECTROSCOPY ANALYSIS

Electrochemical impedance spectroscopy (EIS) is an effective approach for probing detailed information about interfacial properties of surface-modified electrodes. The Nyquist plot of EIS commonly includes a semicircular portion at a lower frequencies that corresponded to the electron-transfer limited process and a linear portion at higher frequencies with attributing to the diffusion process.

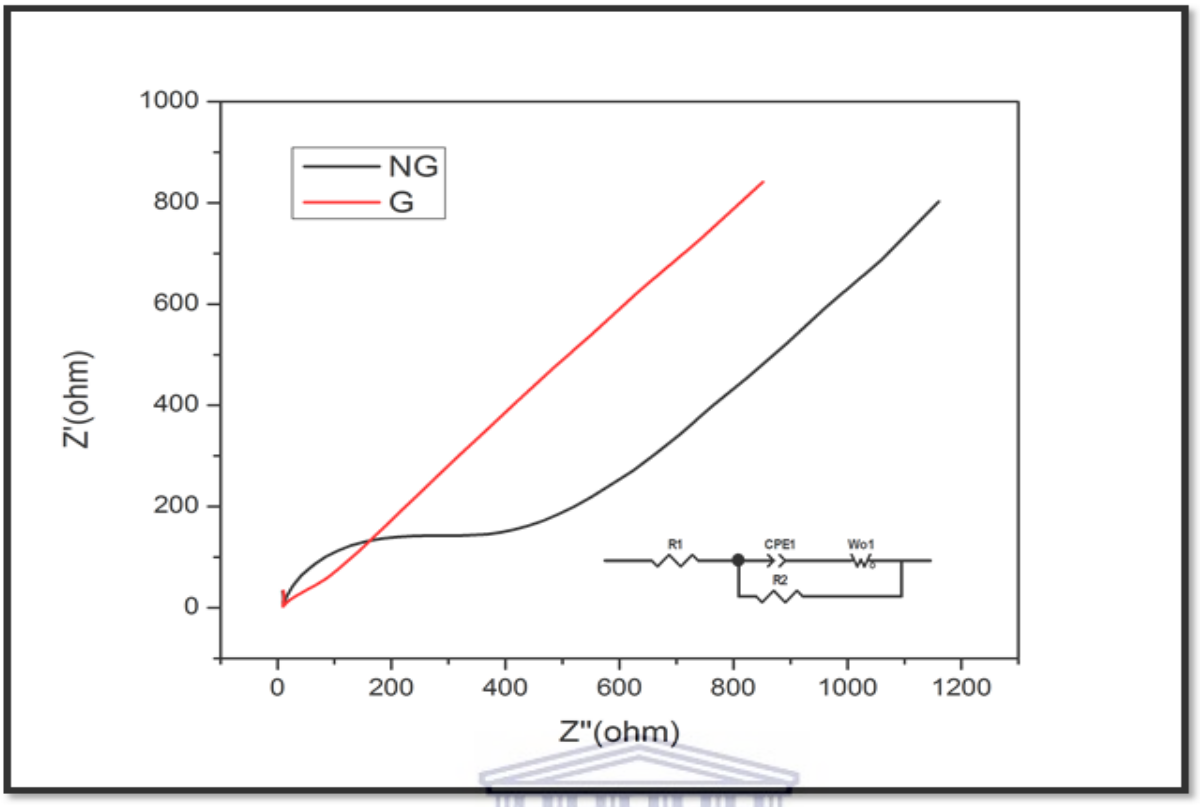

Figure 4.10: Nyquist plots of the impedance data of graphene and N-graphene at a potential of 0,2 V.

In **Figure 4.10**, the Nyquist plots were used to analyse the electrochemical impedance spectroscopy (EIS) data and presented with the equivalent circuit inset. The semi-circles observed at high frequencies on the Nyquist plots of both G and NG represents the charge transfer resistance on the materials. The increase in the charge transfer resistance in NG suggests a slower electron flow in the system due to increased band gap reported on the UV-vis results. The electrochemical properties of N-doped graphene were observed to be better than that of graphene, due to a decreased electron-hole recombination in the system.

4.2 CHARACTERIZATION OF TIO_2 MATERIALS

The prepared TiO_2 materials include: TiO_2 nanowires, TiO_2 nanowires supported on graphene and TiO_2 nanowires supported on nitrogen doped graphene. The materials are characterised using FTIR, XRD, Raman, UV-Vis, Cyclic Voltammetry, Impedance Spectroscopy and Chronoamperometry.

4.2.1 FTIR OF TIO_2 NANOCOMPOSITES

FTIR spectra analysis was performed to investigate the structure and functional groups of the TiO_2, TiO_2-G and TiO_2-NG materials, as shown in **Figure 4.7**.

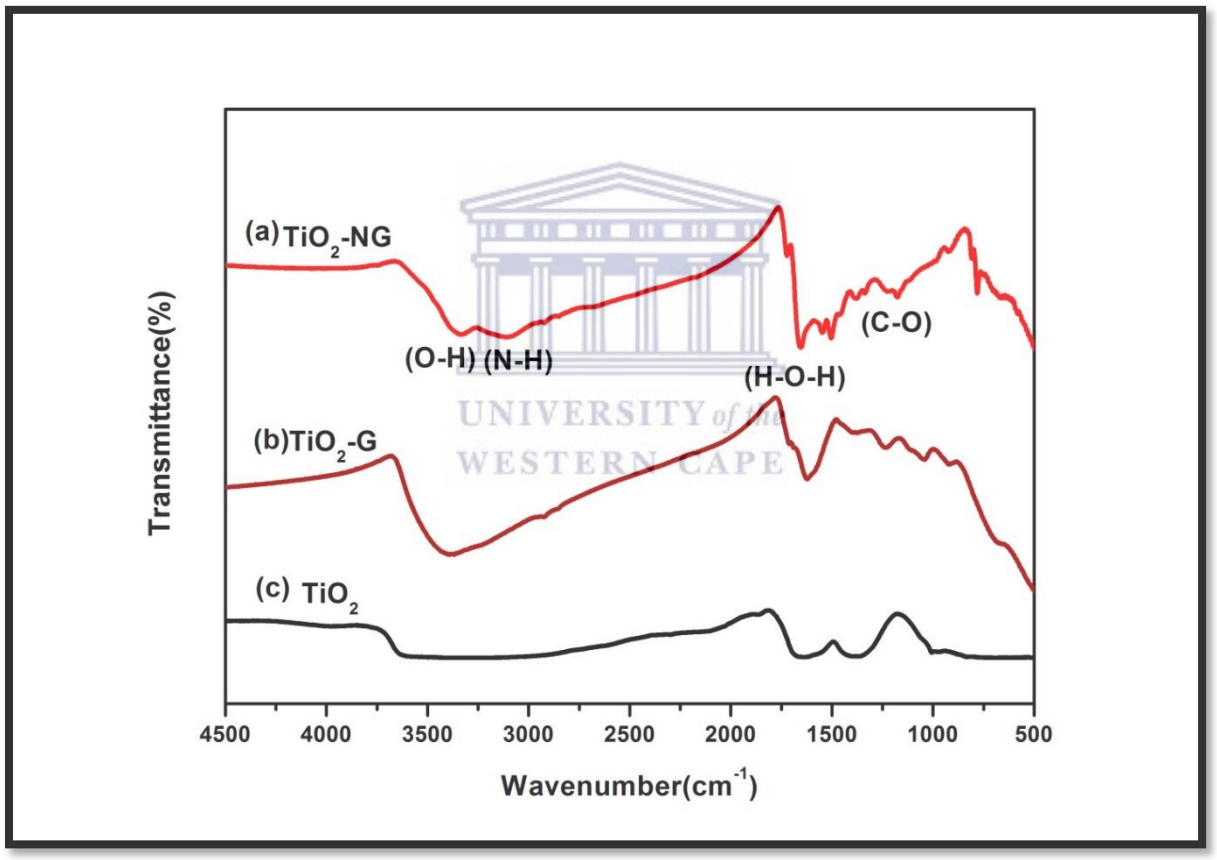

Figure 4.11: FTIR spectrum of TiO_2 nanocomposites, (a) TiO_2-NG, (b) TiO_2-G and (c) TiO_2

In **Figure 4.11**, the broad band at 3421 cm^{-1} belongs to the bending and stretching modes of O-H groups on the surface of the catalyst and the surface adsorbed water. The broad absorption at wavelength of 660 cm^{-1} that is visible for TiO_2-G and TiO_2-nG is attributed to the vibration of Ti-O-Ti bonds in TiO_2. This reveals that the TiO_2 nanowires are strongly bonded to the graphene sheets. The absorption band, appearing at 1560 cm^{-1} in the TiO_2-G composite spectrums exhibits the skeletal vibration of the graphene sheets that is similar to the graphene spectrum in **Figure 4.1**. The C-OH stretching vibration peak at 3421 cm^{-1} of graphene (**Figure 4.1**) shifted to a

higher wavenumber of 3460 cm^{-1} in TiO_2-G composites (**Figure 4.11**), which is attributed to the Ti-O-C bond formation.

4.2.2 XRD ANALYSIS OF TIO_2 NANOWIRES.

The synthesised TiO_2 nanocomposites were structurally and chemically investigated by the X-ray diffraction (XRD) technique, **Figure 4.10** shows the diffraction pattern of TiO_2 and **Figure 4.11** shows the diffraction pattern of TiO_2-G and TiO_2-NG.

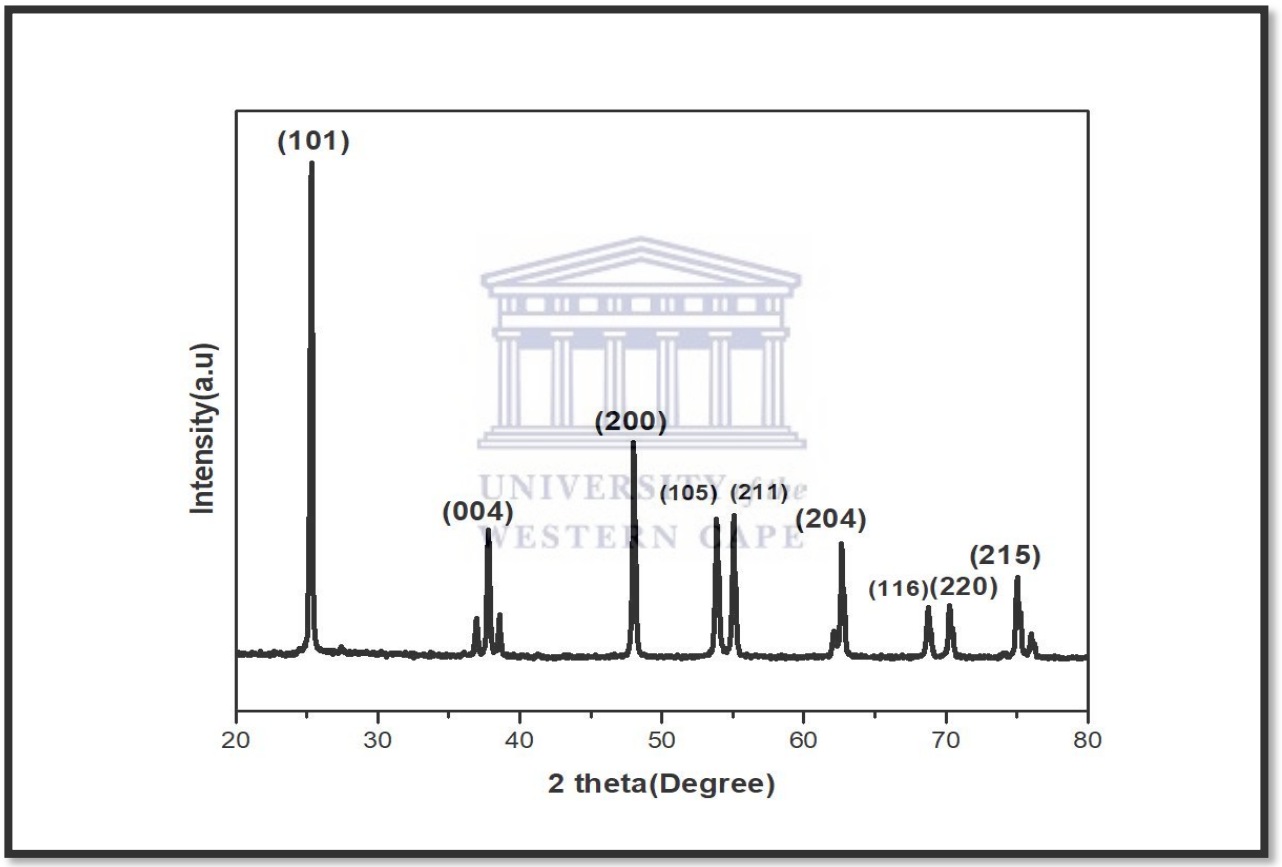

Figure 4.12: The diffraction pattern of TiO_2 nanowires.

The XRD pattern of TiO_2 exhibited several peaks located at 25.30°, 37.80°, 48.07°, 53, 72°, 55.09°, 62.80°, 68.96°, 70.49° and 75.12°, corresponding to crystal phases of (101), (004), (200), (105), (211), (204), (116), (220), (215) respectively. All the peaks in the XRD pattern correspond to the anatase phase of TiO_2, according to the JCPDS card: 00-064-0863. (74) The diffraction pattern of the TiO_2 sample is shown in **Figure 4.12.** The highly intense and sharp peaks observed on the diffraction pattern indicates that TiO_2 nanowires are highly crystalline in nature.

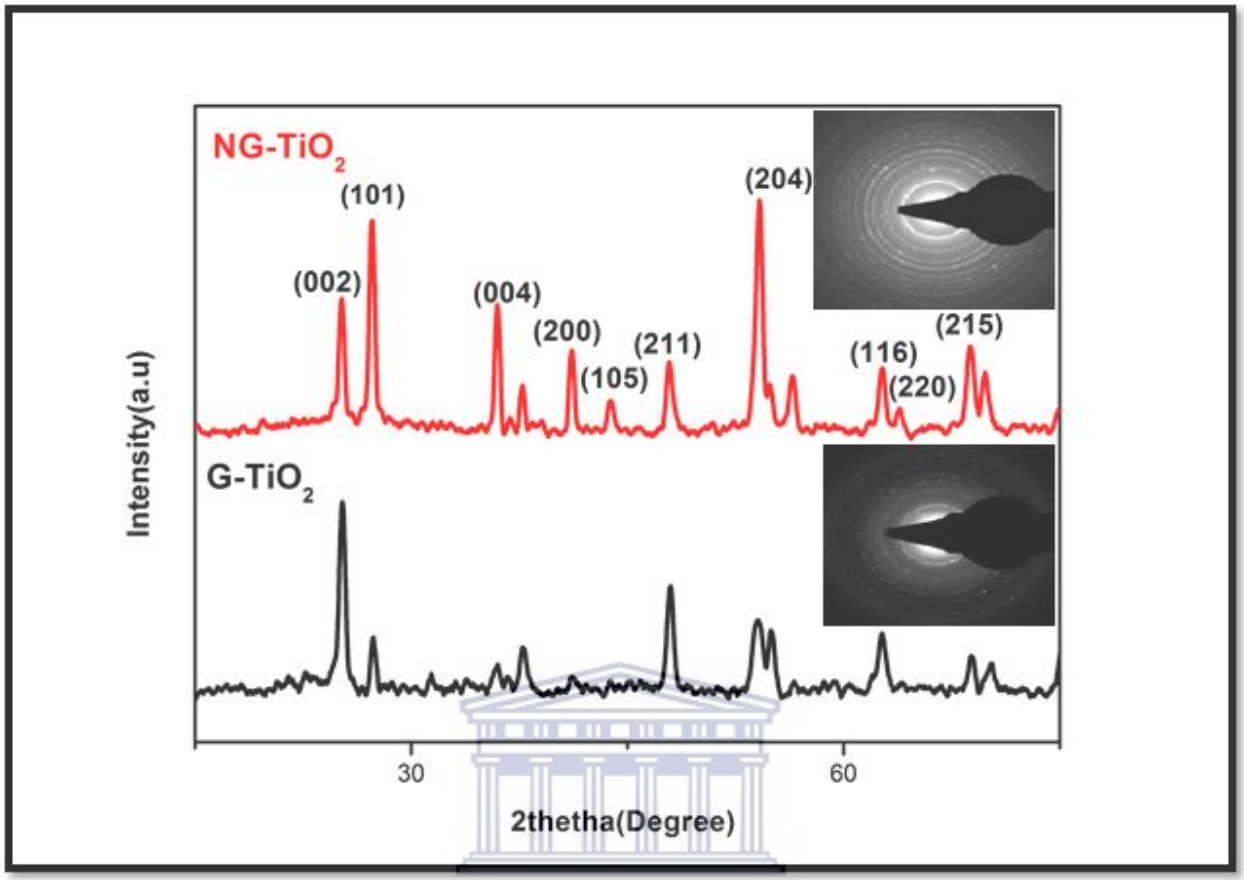

Figure 4.13: The diffraction pattern of TiO_2 nanocomposites,(a) NG-TiO_2 and (b) G-TiO_2 and SAED diagrams.

The XRD pattern of photocatalysts is shown in **Figure 4.13**, TiO_2-G and TiO_2-nG composites exhibit a similar XRD pattern to that of TiO_2 nanowires(JCPDS card: 00-021-1272). The diffraction peak of graphene at 25, 08° corresponds with the (002) reflection plane, which confirms the formation of the composites. The SAED diagrams show the crystanillity of the materials respectively, the diagram of NG-TiO_2 shows more crystals formed than that of G-TiO_2.

4.2.3 SURFACE AREA ANALYSIS OF TIO_2 NANOWIRES

Morphological analysis is a useful characterization technique that is used in this research to determine the crystallinity of nanoparticles and nanowires, these include SEM and TEM. The physical properties of TiO_2 nanomaterials were determined and compared for effectiveness. The surface area to volume ratio for the nanomaterials was analyzed to determine which morphology has a better photocatalytic activity.

4.2.3.1 SCANNING ELECTRON MICROSCOPY

The elemental compositions and morphologies of the TiO_2 samples were investigated using SEM analysis. **Figure 4.12** and **4.13** shows information for TiO_2-G and TiO_2-NG respectively, where **(A), (B)** represent the images of TiO_2 composites.

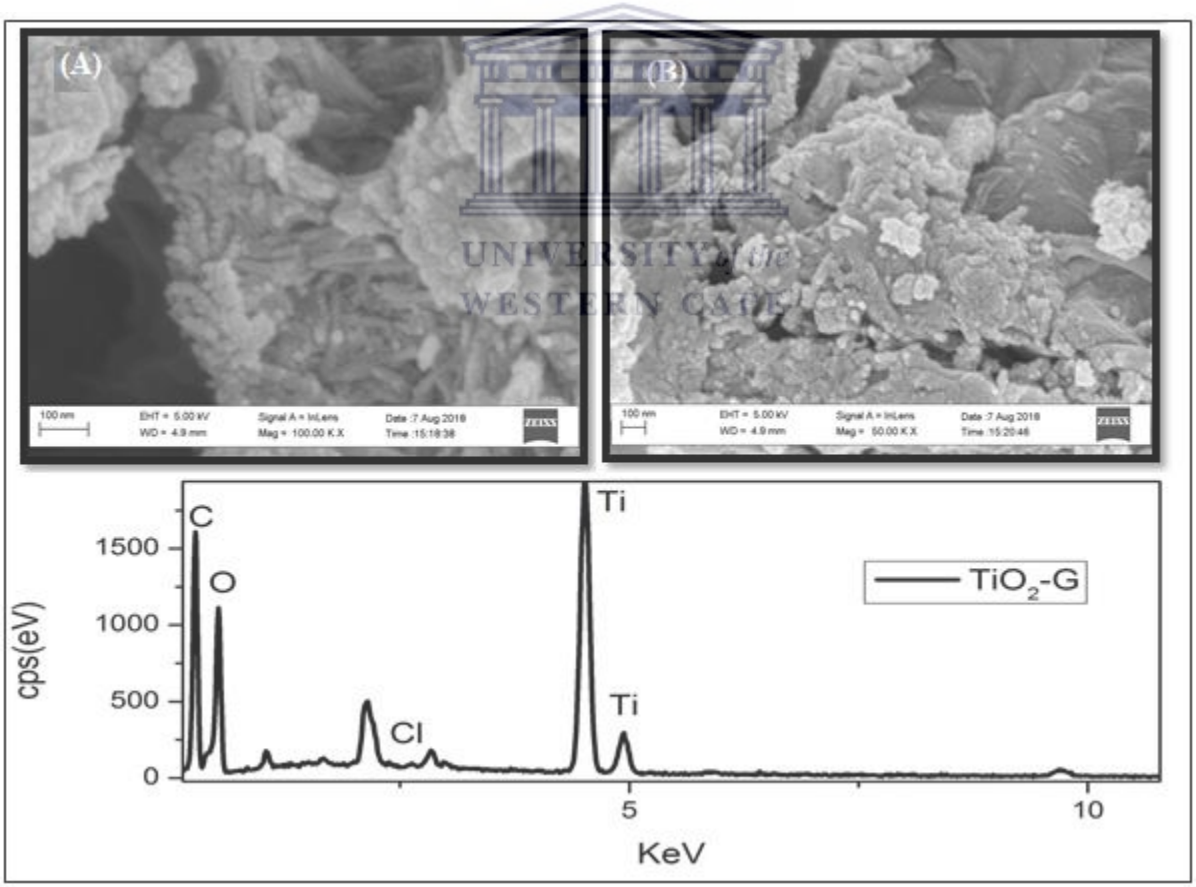

Figure 4.14: SEM images and EDS graph of TiO_2-G

From **Figure 4.14**, Images **(A)** and **(B)**, show nanowires of TiO_2 on the graphene template, the EDS spectrum exhibit peaks attributed to Ti, O, and C, which confirms the success formation of the TiO_2-G nanocomposite.

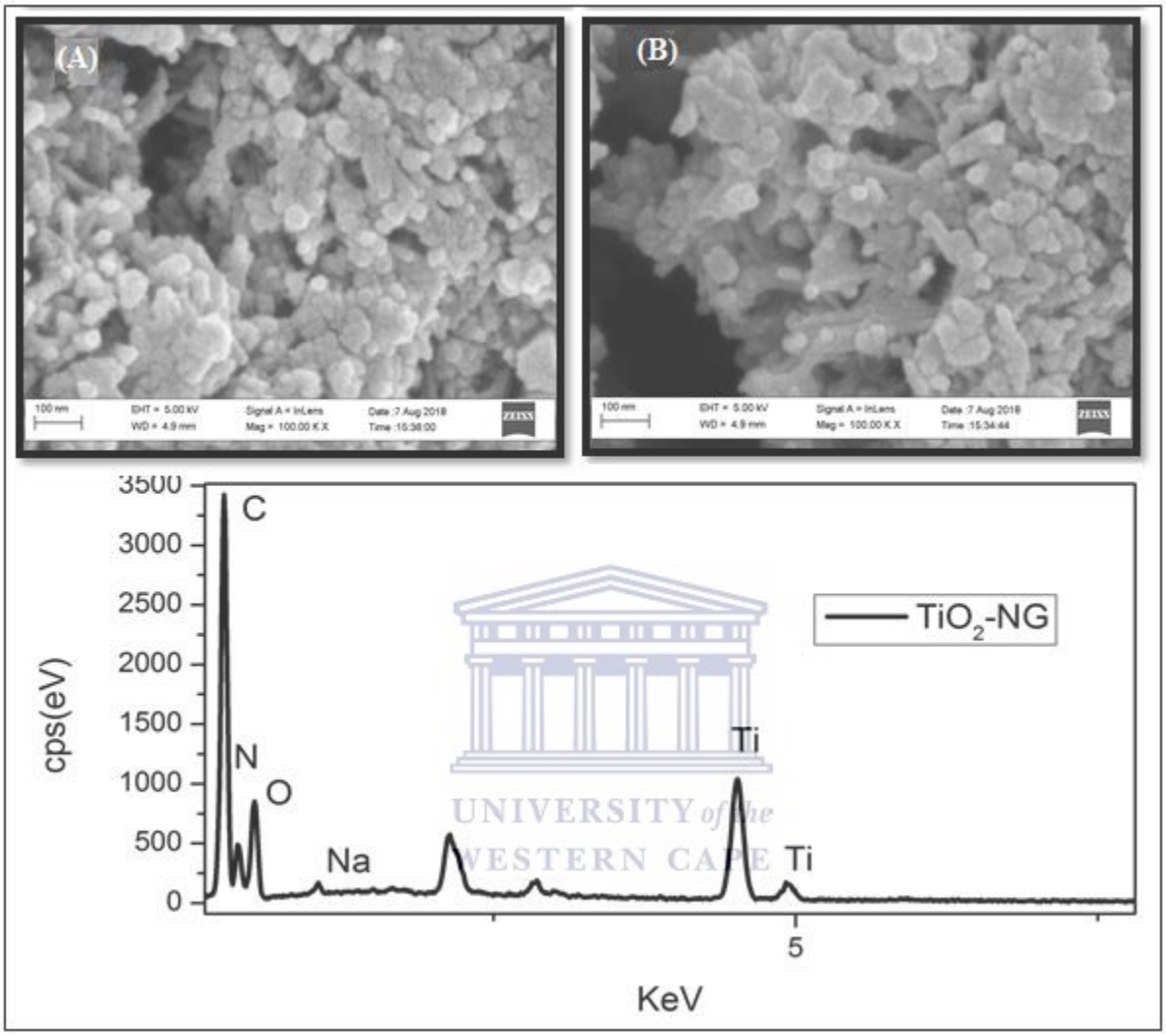

Figure 4.15: SEM images and EDS graph of TiO_2-NG

Figure 4.15 A and **B,** exhibit a longitudinal, rod-like structures which can be attributed to the TiO_2 nanowires, supported on N-graphene. The DS spectrum exhibits peaks attributed to Ti, O, N and C, which confirms the success formation of the TiO_2-NG nanocomposites.

4.2.3.1 TRANSMISSION ELECTRON MICROSCOPE

TEM was used determine the surface structure of the nanomaterials synthesized, the TiO_2 materials exhibit a nanoparticle and a nanowire morphology as shown in the TEM images. **Figure 4.13** illustrates the surface structure of pure TiO_2**, Figure 4.14** illustrates the morphology of TiO_2-G and **Figure 4.15** illustrates that of TiO_2-NG, respectively.

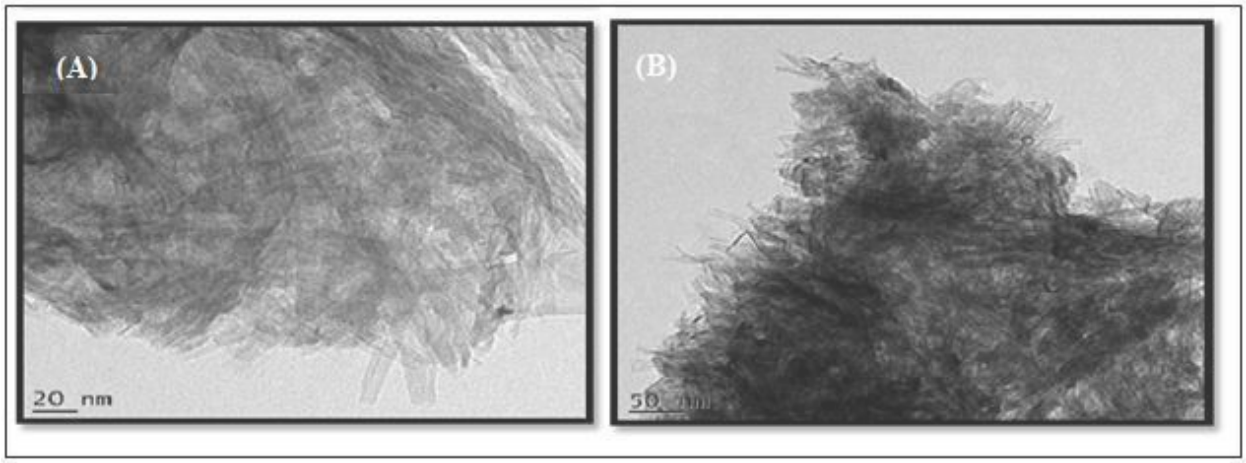

Figure 4.16: TEM images of TiO_2

Figure 4.16 shows the TEM images of TiO_2 nanowires, A and B show needle-like structures, the materials seemed to be stacked on top of each other, in image B the scale is increased from 20 nm to 50 nm, which shows agglomeration of the TiO_2 material

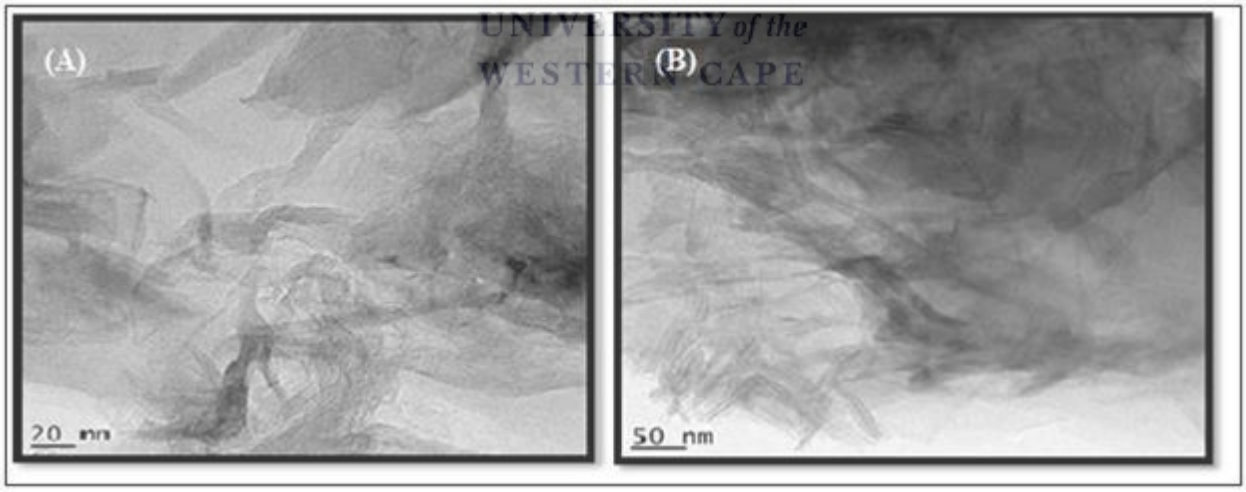

Figure 4.17: TEM images of TiO_2-G at (A) 20 nm and (B) 50 nm magnifications

In **Figure 4.17** and **4.18**, the graphene and nitrogen doped graphene material are distributed on the surface of the TiO_2 nanowires, respectively. The morphology of TiO_2 supported on graphene is shown in **Figure 4.17.** The TEM images of TiO_2-G nanowires show success in incorporation of TiO_2 material on the graphene support. In Images **(A)** and **(B)** the TiO_2 sample appears to be well dispersed across the graphene sheets, with some sites showing presence of agglomeration.

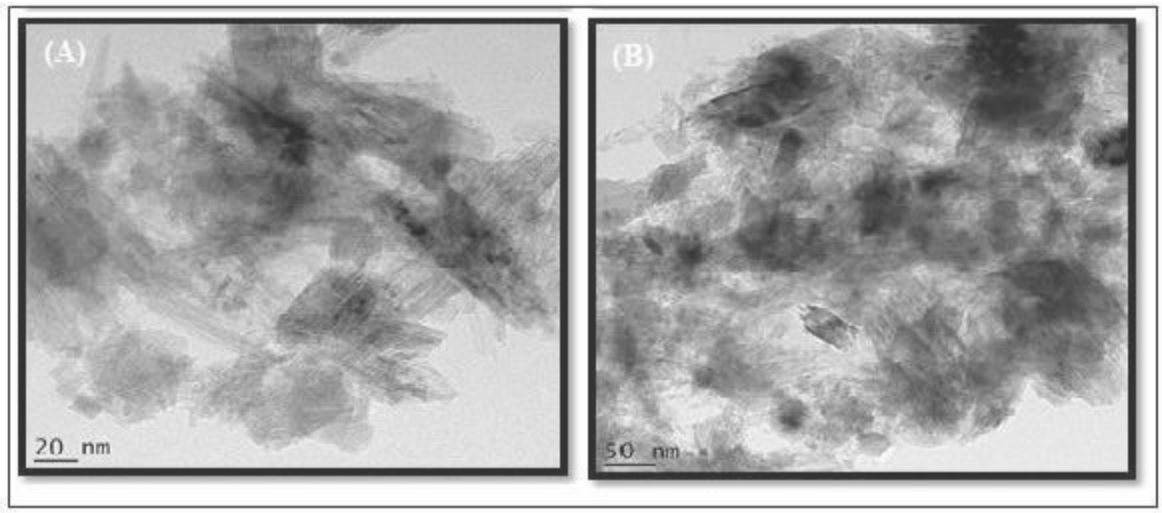

Figure 4.18: TEM images image of TiO_2-NG

The morphology of the synthesised nanomaterial in **Figure 4.18** has similarities to that of TiO_2 supported on graphene, in **Figure 4.17**. The TEM images of TiO_2-G nanowires show success in incorporation of TiO_2 material on the graphene support. The TiO_2 material is well distributed throughout the N-graphene support, which suggest that the nanocomposite has more active sites available for photocatalysis of the materials of interest. Agglomeration is seen on certain sites which may be the result of the synthesis method used in preparing the materials.

4.2.4 UV-VIS SPECTRUM OF TIO_2 NANOCOMPOSITES

The UV-Vis spectrums of TiO_2 nanocomposites were determined, **Figure 4.19** shows the absorbance spectrum of TiO_2,TiO_2-G and TiO_2-NG.

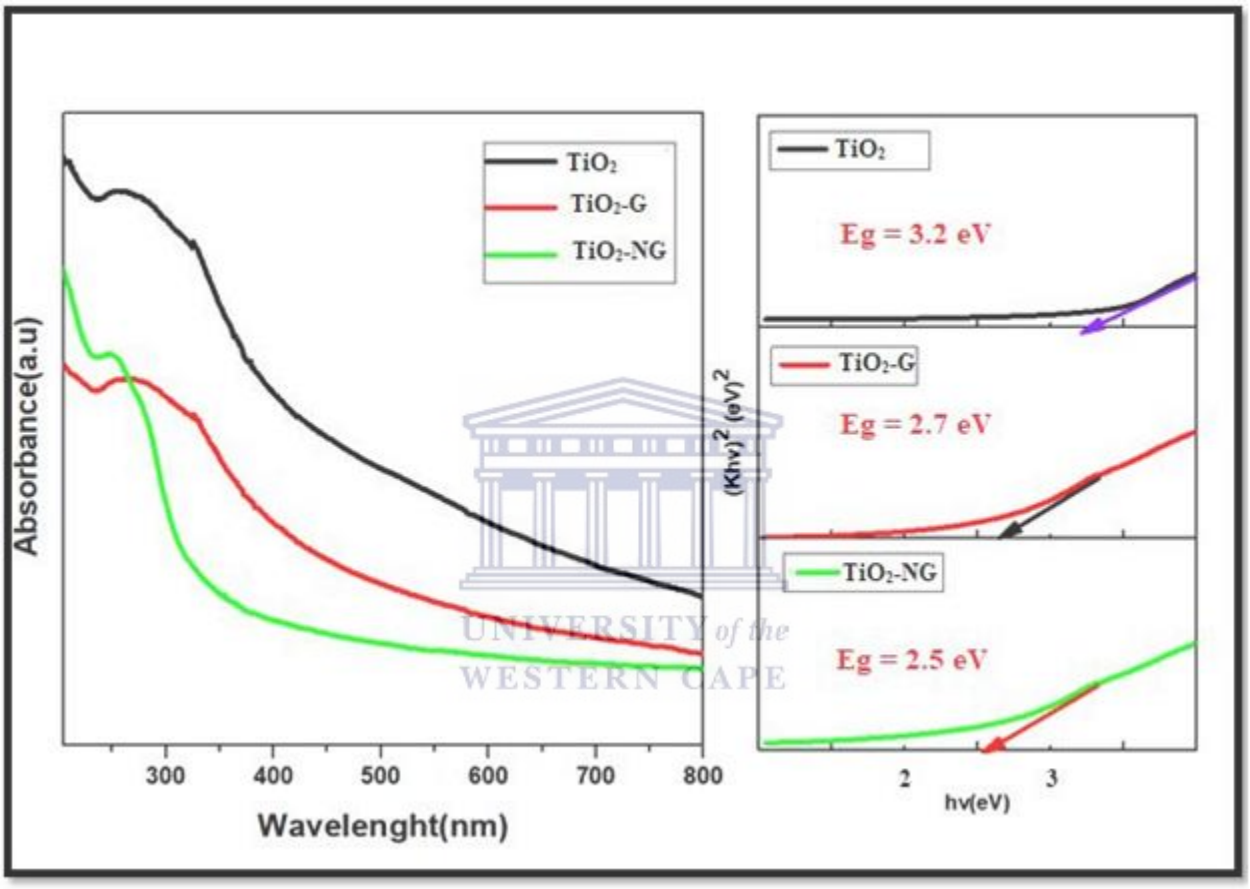

Figure 4.19: UV sprectrum of TiO_2 nanocomposites.

The absorption spectrum of TiO_2 nanocomposites is shown above. TiO_2 shows the absorbance maxima at 315 nm. Incorporation of the reduced graphene oxide to TiO_2 induced a blue-shift in the absorption wavelength of TiO_2 to 310 nm as observed on the TiO_2-G composite. Introduction of the nitrogen doped graphene to TiO_2 nanowires further reduced the absorption maxima of TiO_2 to 270 nm, indicating a decrease in particle size and therefore increase in surface area favourable for catalytic reactions. The photocatalytic reduction of GO to rGO can be represented by the below equations, where the electrons accumulated within the TiO_2 reduces epoxy and carboxylate functional groups in the GO sheets.

The optical band gaps (Eg) of the TiO_2-NG nanocomposites were extrapolated from the graphs where $(Khv)^2$ equals zero, as presented in **Figure 4.19**. The optical band gap of TiO_2-NG nanowires was found to be 2.5 eV, while that of TiO_2-G has a band gap of 2.7 eV and TiO_2 has an energy band gap of 3.2 eV.

$$TiO_2 + hv \rightarrow TiO_2(e_{CB^-} + h_{VB^-}) \quad (4.1)$$

$$TiO_2(e_{CB^-} + h_{VB^-}) + C_2H_5\mathrm{OH} \rightarrow TiO_2(e_{CB^-}) + C_2H_5O^{\bullet} + H^+ \quad (4.2)$$

$$TiO_2(e_{CB^-}) + GO \rightarrow TiO_2 - Gr \quad (4.3)$$

4.2.5 Electrochemical Analysis

4.2.5.1 CYCLIC VOLTAMMETRY OF TIO_2-G COMPOSITES

4.2.5.1.1 Effects of Scan Rates

Scanning the potential in both directions provides with the opportunity to explore the electrochemical behaviour of species generated at the electrode. **Figure 4.17** shows the cyclic voltammogram for TiO_2-NG at different scan rates.

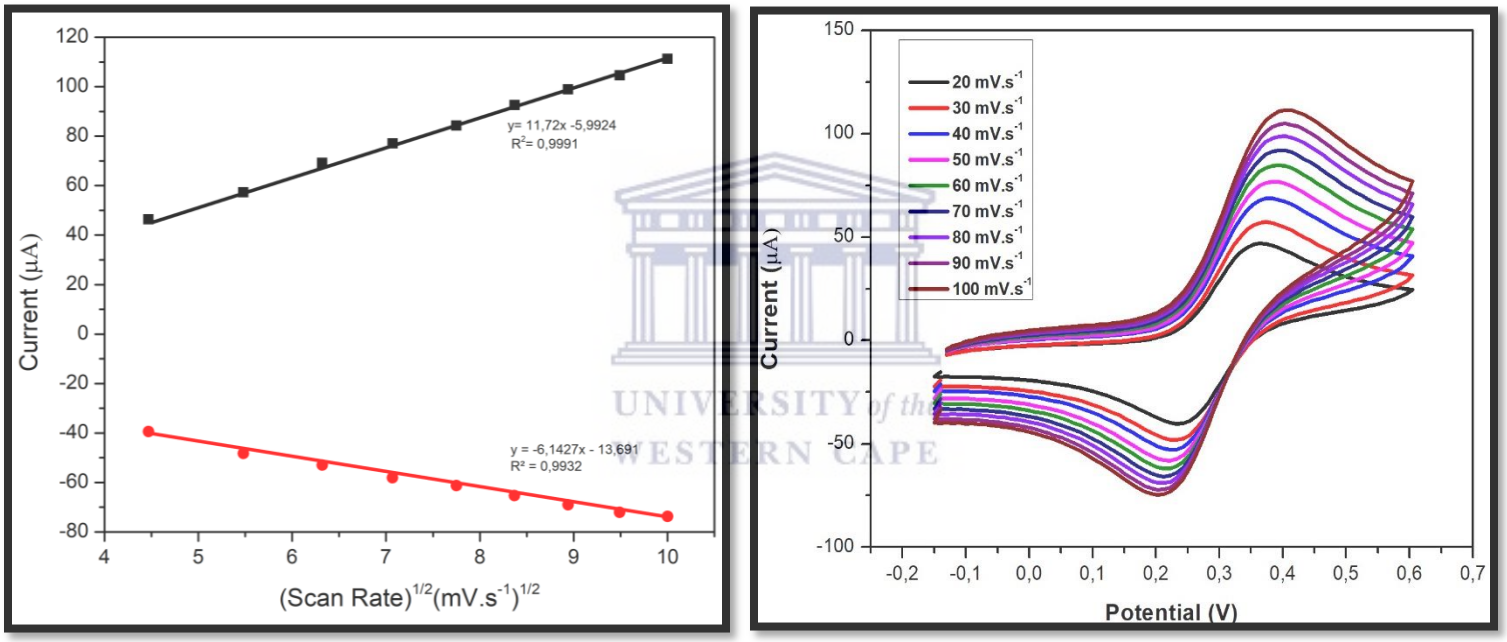

Figure 4.20:Scan rates of TiO_2-NG in K_3[Fe(CN)6]

In **Figure 4.14, 4.15 and 4.16**, the reduction process occurs from the initial potential of -0,2 to the switching potential at 0,6. In this region the potential is scanned negatively to cause a reduction, resulting in a cathodic current (i_{pc}) with a corresponding cathodic peak potential (E_{pc}). The Epc is reached when all of the substrate at the surface of the electrode has been reduced. After the switching potential has been reached, the potential scans positively. This results in anodic current (I_{pa}) and oxidation to occur, which results to an anodic peak potential (E_{pa}), and is reached when all of the substrate at the surface of the electrode has been oxidized (78). The change in Ep was determined for TiO_2, TiO_2-G, and TiO_2-NG.

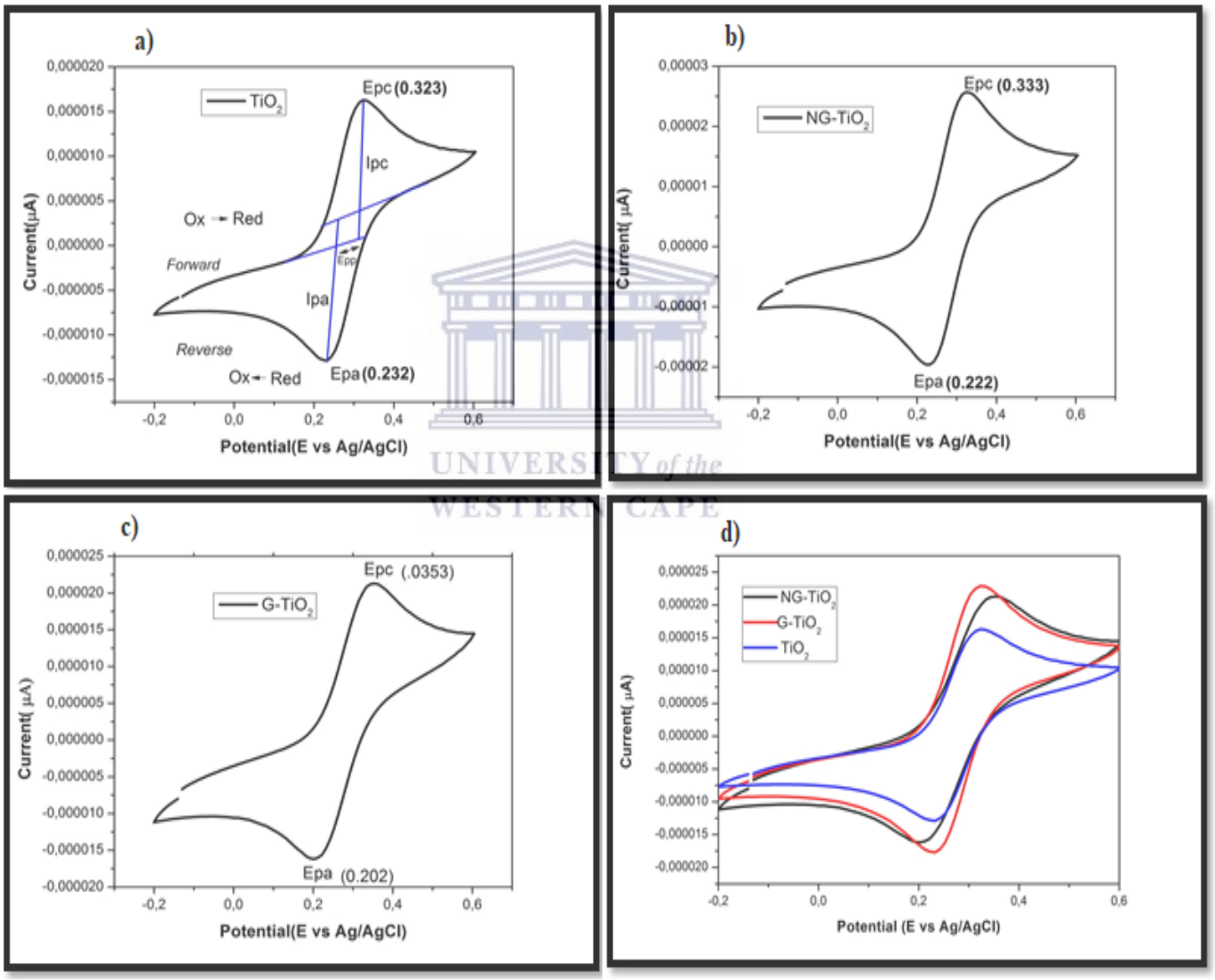

Figure 4.21: Cyclic voltammograms of TiO_2, G-TiO_2 and NG-TiO_2 in K_3[Fe(CN)6] at 30 mV/s.

In **Figure 4.21**, the voltammograms show clear anodic and cathodic peaks for each electrode and overlaid on **Figure 4.21** (**D**). The peak at positive potentials on the anodic (forward) sweep around 0.3 V, which represents the oxidation of Ti(III) to Ti(IV) with the loss of one electron. The composites of G-TiO_2 and NG-TiO_2 displayed large current density. The increase in the redox peak current observed for the rGO/TiO_2 and NG-TiO_2 suggests that these nanocomposites exhibit better electrical conductivity between the electrode and the electrolyte interface induced by the surface modification of graphene oxide. The change in Ep of the TiO_2, TiO_2-G and TiO_2-NG materials was determined to be 91 mV, 111 mV, and 151 mV respectively. The lower separation in potential difference indicates fast electron kinetics.

4.2.5.2 IMPEDANCE SPECTROSCOPY ANALYSIS

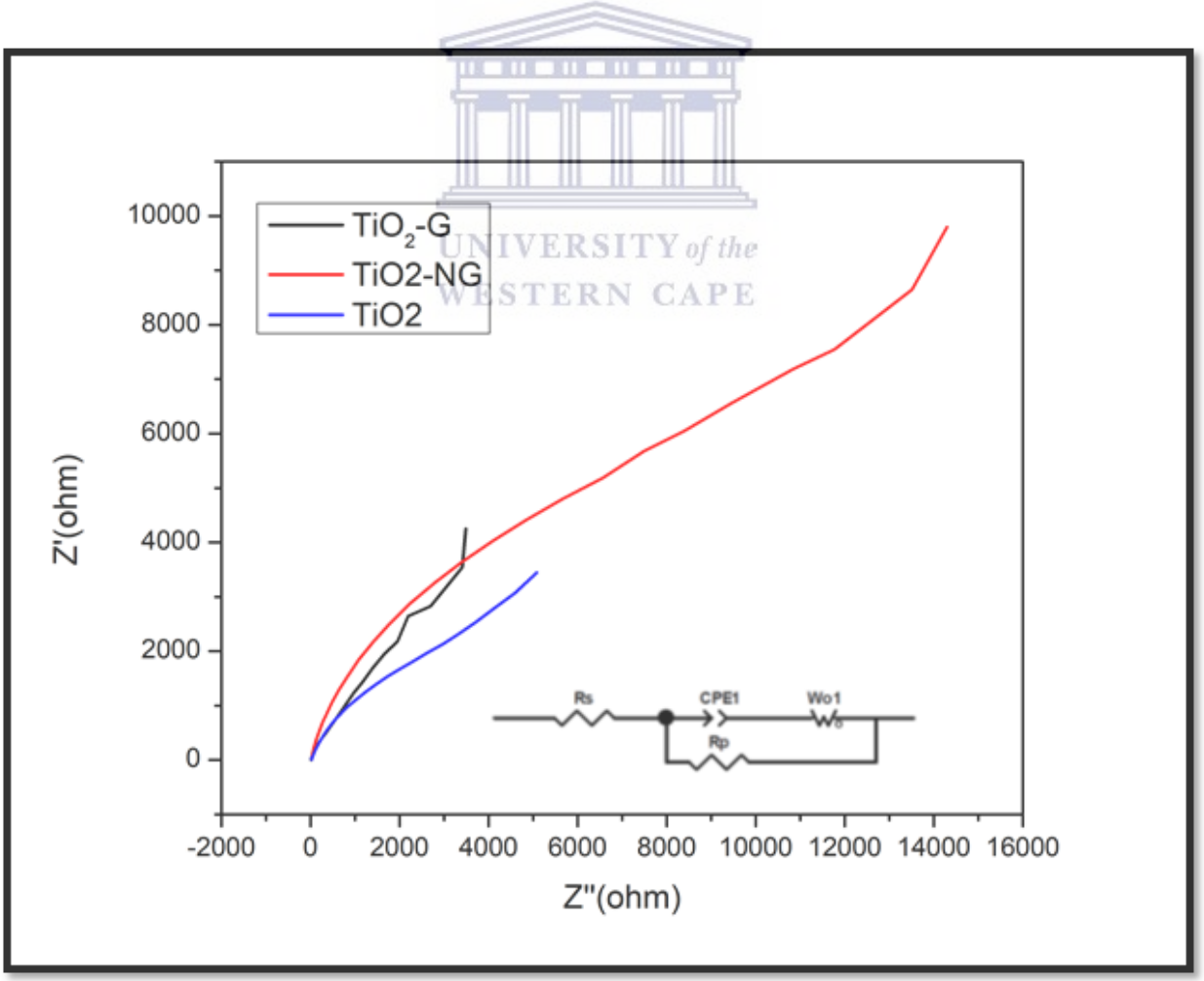

Figure 4.22: Nyquist plots of the impedance data of TiO_2, G-TiO_2 and nG-TiO_2 at 0.2 potential.

Electrochemical impedance spectroscopy (EIS) was used to characterize the charge-carrier migration. EIS characterization was carried out for TiO_2, TiO_2-G, and TiO_2-NG based electrodes at potential -0.2 V. **Figure 4.22** shows the EIS measurement in Nyquist plots. The TiO_2 EIS curve shows lower charge transfer resistance hence faster electron kinetics compared to TiO_2-G and TiO_2-NG. TiO_2-NG has a higher charge transfer resistance compared to the other nanomaterials due to a decreased band gap, which renders it a better photocatalyst for dye degradation in waste water.

CHRONOPOTENTIOMETRY

For practical applications, the production of hydroxyl radicals of the materials was determined using chronopotentiometry, which monitors the current at the electrode as the function of potential and time. When the current is applied at 5 mA, the measured potential is changed due to the voltage loss, which gradually changes after that, because of a concentration overpotential that is developed as the concentration of the reactant is exhausted at the electrode surface. Chronopotentiometry measurements were carried out for TiO_2, TiO_2-NG and TiO_2-G.

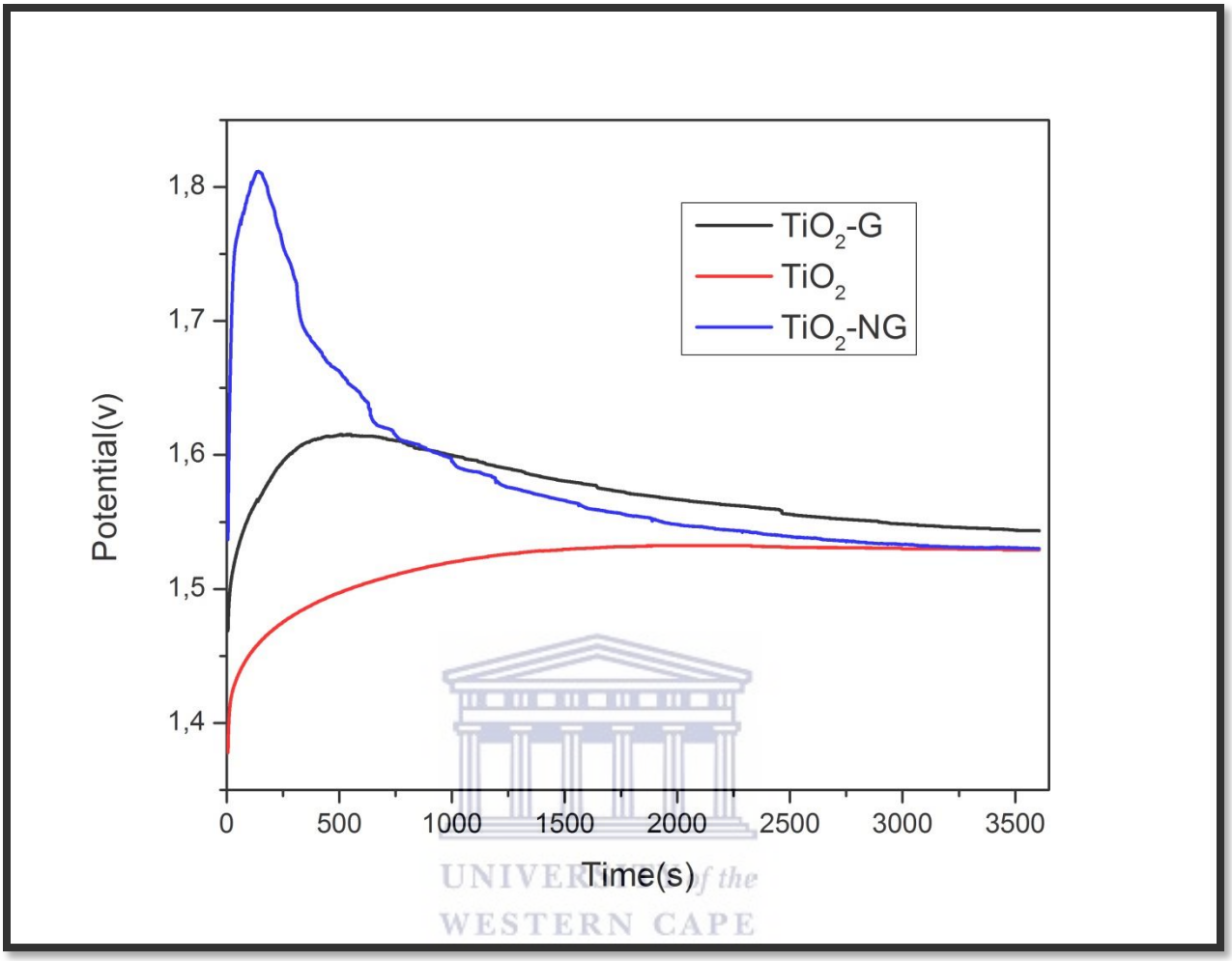

Figure 4.23: Choronoamperometry plot of TiO_2,TiO_2-G and TiO_2-NG in $K_3[Fe(CN)6]$ at 5mA.

The Chronoamperometry of the materials was conducted at 5 mV/s for 3600 seconds in $K_3[Fe(CN)_6]$. From **Figure 4.23**, the chronopotentiometry response of TiO_2 shows an increase in potential to a constant potential of 1.5 V. TiO_2-G exhibited the highest potential of 1.6 V and declined to 1.55 V from 480 seconds to 3600 seconds. The results obtained indicate that TiO_2-G experiences higher potentials for a longer period compared to TiO_2, hence a higher anodic potential. The graph of TiO_2-NG shows an abrupt increase in potential to 1.82 V for 250 seconds. The higher anodic potential indicate higher production of hydroxyl radicals from water for the decomposition of organic pollutants. The high production of hydroxyl radicals lead to effective trapping of organic pollutants.

CHAPTER FIVE

CONCLUSION AND RECOMMENDATION

5 INTRODUCTION

This chapter summarizes the findings of the research project by presenting an overview of the achievements of the research objectives, a discussion of the importance and contributions of the results is presented. The recommendations of future work and research based on the concept of photocatalysis is highlighted.

5.1 CONCLUSION

TiO2 photocatalyst is considered photocatalytically superior in advanced oxidation processes as compared to the other catalyst reported in literature. However, the use of high energy UV radiation in the application of TiO2 due to its high energy gap has commanded a lot of research effort to shift the energy gap to the low energy visible region of the spectrum. Therefore, the aim of this study was to shift the energy gap of TiO2 from the UV region to the visible region. This was done by introducing nitrogen doped graphene to the TiO2 nanowires in efforts to reduce the band gap. The nitrogen doped graphene was prepared by chemically doping with nitrogen and subsequently reducing graphene oxide. FTIR results confirmed the presence of nitrogen in the system by the appearance of C-N and N-H groups on the spectra. When the nitrogen doped graphene was grafted on TiO2 nanowires, the XRD results showed the fingerprint patterns of both TiO2 and N-doped graphene in the system. These results substantiated the successful incorporation of N-doped graphene on TiO2 nanowires. The optical band gap of TiO2-NG from UV-vis was reduced to 2.5 eV by introduction of the N-doped graphene to the system from 3.2 eV of pristine TiO2. Electrochemical characterisation of the materials prove TiO2-NG a better catalyst for advanced oxidation reactions due to the increased electron kinetics observed on cyclic voltammetry and impendence spectroscopy. The aim of this research project was successfully achieved and the AOP catalyst prepared in this study have a greater potential for application in water purification. A successful application of the materials synthesised promise a complete mineralisation of persistent organic pollutants in the environment, which will increase the availability of fresh drinking water in the world.

5.2 RECOMMODATIONS AND FUTURE WORK

For recommendations and future work, the application of the prepared TiO2-NG catalyst in waste water for demineralisation of organic pollutants needs to be explored. Greater research based on advanced oxidation processes need to be done, as there remains a significant amount of uncertainty regarding the effectiveness of total degradation of persistent organic pollutants. Most research on removal of organic pollutants from wastewater have been based on an individual treatment process, while these single treatment technologies have accumulated challenges with respect to efficiency. Literature shows that the application of combined AOP treatment methods could result in greater productivity, with respect to the removal of organic pollutants in wastewater systems.

REFERENCES

1. WaterWise .(2018). Water Situation in South Africa. Available from http://www.waterwise .co.za/water/environment/situation.html.
2. NASA. Earth's Water. (2017). Available from http://appsolutelydigital.com/Nasa/chapter1.html.
3. Hannah, R. (2018) Water Use and Sanitation. Available from https://www.ourworldindata.org/water-use-sanitation
4. Stephen, M.K. (2003) Development Challenges of Water Resource management in Africa. African Water Journal, 3, 7-17.
5. City of Cape Town. (2018). Water Dashboard. Available from https://www.resource.capetown.gov.za/documentcentre/Documents/City%20research%20reports%20and%20review/damlevels.pdf
6. Petersen,T. (2017, April,2) Cape Town water is 'safe to drink'. Weekend Argus. Available from https://www.iol.co.za/news/south-africa/western-cape/cape-town-water-is-safe-to-drink-8460152
7. Bartram J, & Balance R. (1996). A Practical Guide to the Design and Implementation of Freshwater Quality Studies and Monitoring Programmes. Water Quality Monitoring, 1-22. Available from http://apps.who.int/iris/handle/10665/41851.
8. Damstra T, & Pronczuk J. (2008). PERSISTENT ORGANIC POLLUTANTS (POPs). Children's Health and the Environment, 1-29. Available from http://www.who.int/ceh/capacity/Lead.pdf
9. Ashraf M.A. (2017) Persistent organic pollutants (POPs). Environmental Science Pollution Research, 24, 4223-4227.
10. Ekevwe A.E, Isaacl A, Baertholomew G, Aroh O. (2018). Review of Organic Pollutants in Wastewater along the Course of River Gwagwarwa and River Rafin Malam in Kano State-Nigeria. Journal of Biotechnology and Bioengineering, 2(2), 36-39
11. Miklos D.B, Remy C , Jekel M, Linden C.G , Drewes J.E, Hübne U. (2018) Evaluation of advanced oxidation processes for water and wastewater treatment. Water Research, 139, 118-131.

12. Saravanam R, Gracia F, Stephen A. (2017) Basic Principles, Mechanism, and Challenges of Photocatalysis. Polymer and Composite Materials. Available from https://www.springer.com/cda/content/document/cda_downloaddocument/9783319624457-c2.pdf?SGWID=0-0-45-1616582-p180992849.
13. Mullins T. (2007) The Chemistry of Water Pollution. Environmental Chemistry. Available from https://doi.org/10.1007/978-1-4615-6921-3_12.
14. Ranjan S, Dasgupta N, Lichtfouse E. (2017) Nanoscience in Food and Agriculture 5. Sustainable Agriculture Reviews. 26, 338-453.
15. Anderson M.G, McDonnell J.J. (2005) Point and NonPoint Source Pollution. Enclopedia of Hydrological Sciences. Available from doi:10.1002/0470848944.hsa097.
16. Mehta V. (2018) Types of Environmental Pollution & their Harmful Effects. Available from https://www.toppr.com/bytes/environmental-pollution/.
17. Bradford A. (2018) Pollution Facts & Types of Pollution. Live Science Contributor. Available from https://www.livescience.com/22728-pollution-facts.html.
18. Alvarez-Benedi J, Munoz-Carpena R. (2013) Mutlidisiplinary Approach for Assessing Subsurface Non-Point Source Pollution. Soil Water Solute Process Characterization.4-11
19. Ene A (2014) Persistent Organic Polltants: Environment Persistence and Bioaccumulation Potential. Scientific Research,17(2), 115-122.
20. Umar M, Aziz H.A (2013) Phtotocatalytic Degradation of Organic Pollutants in Water. Organic Pollutants - Monitoring, Risk and Treatment. Available from https://www.intechopen.com/books/organic-pollutants-monitoring-risk-and-treatment/photocatalytic-degradation-of-organic-pollutants-in-water.
21. Pronczuk, J, Damstra, T(2013) Persistent organic pollutants (POPs): Children's health and the environment. World Health Organisation. Available from https://www.who.int/ceh/capacity/POPs.pdf.
22. Abdallah M.A (2015) Persistent Organic Pollutants. Issues in Environmental Sciences and Technology. Available from https://pubs.rsc.org/en/content/chapter/bk9781782620761-00150/978-1-78262-076-1.

24. Environmental Affairs (2011) National Implementation Plan for the Stockholm Convention of Persistent Organic Pollutants. Available from https://www.environment.gov.za/sites/default/files/docs/national_implementation_plaun_organic_pollutants.pdf.
25. WHO (2003) Aldrin and Dieldrin in Drinking-water. Guidelines for Drinking-water quality.Available from https://www.who.int/water_sanitation_health/water-quality/guidelines/chemicals/adrindieldrin.pdf.
26. WHO (1989) Aldrin and Dieldrin Health and Safety Guide. Environmental Health Criteria. Available from http://apps.who.int/iris/bitstream/handle/10665/39358/9241543434-eng.pdf?sequence=1&isAllowed=y.
27. Jorgenson J.L (2001) Aldrin and Dieldrin: A Review of Research on Their Production, Environmental Depositionand Fate, Bioaccumulation, Toxicology, and Epidemiology in the United States. Environmental Health Perspectives. 109,133-139.
28. Mo A.S.P, Nawfa R, Martak F, Shimizu K (2017) Biodegradation of Aldrin and Dieldrin bytge White-Rot Fungus *Pleurotus ostreatus*. Current Microniology. 74, 320-324.
29. WHO (2004) Chlordane in Drinking-water. Guidelines for Drinking-water Quality. Available from https://www.who.int/water_sanitation_health/dwq/chemical s/chlordane.pdf.
30. New Jersey Department of Health and Senior Services (2005). Hazardous Substance Fact Sheet. Available from http://nj.gov/health/eoh/rtkweb/documents/fs/0683.pdf.
31. WHO (2011) The Use of DDT in Malaria Vector Control. Global Malaria Programme. Available from https://www.who.int/malaria/publications/atoz/who_htm_gmp_2011/en/
32. WHO (2004) DDT and its Derivatives in Drinking-water. Guidelines for Drinking-water Quality. Available from https://www.who.int/water_sanitation_health/dwq/chemicals/ddt.pdf.
33. WHO (2004) Endrin in Drinkin-water. Guidelines for Drinking-water Quality. Available from http://www.who.int/water_sanitation_health/dwq/chemicals/endrin.pdf.
34. WHO (2004) Heptachlor and Heptachlor Epoxide in Drinking–water. Guidelines for Drinking-water Quality. Available from http://www.who.int/water_sanitation_health/dwq/chemicals/heptachlor.pdf.

35. Keilhorn J, Schmidt S, Mangelsdorf (2006) Heptachlor. Concise International Chemical Assessment Document. Available from http://www.who.int/ipcs/publications/cicad/cicad70.pdf
36. WHO (2004) Hexachlorobenzene in Drinking-water. Guidelines for Drinking-wate Quality. Available from http://www.who.int/water_sanitation_health/dwq/chemicals/hexachlorobenzene.pdf
37. WHO (2004). Guidelines for Drinking-water Quality. 1(3), 364-476.
38. Lewandowski M, Levi P, Hodgson E (1989). Induction of cytochrome P-450 isozymes by mirex and chlordecone. J Biochem Toxicol 4(3):195-199.
39. Mehendale H.M(1981). Onset and recovery from chlordecone- and mirex-induced hepatobiliary dysfunction. Toxicol Appl Pharrnacol 58(1):132-139.
40. Jongbloed R.H, Visschedijk A.J.H, Laane R.W.P.M (200) Toxaphene an Analysis of Possible Problems in the Aquatic Environment. Available from http://edepot.wur.nl/174237.
41. Muir D.C.G, de Boer J (1995) recent developments in the analysis and environmental chemistry of Toxaphene with emphasis on the marine environment. Trends in Analytical Chemistry, 14(20), 56-68.
42. Faroon O.M, Keith L.S, Smith-Simon C, De Rosa T (2003) Polychlorinated biphenyls:Human health aspects. Concise International Chemical Assessment. Available from http://www.who.int/ipcs/publications/cicad/en/cicad55.pdf.
43. WHO (2003) Polychlorinated Biphenyls: Human Health Aspects. 56,32-58.
44. WHO (2016) Dioxins and their effects on human health. Available from http://www.who.int/news-room/fact-sheets/detail/dioxins-and-their-effects-on-human-health
45. Rappe C (1993) Environmental concentrations and ecotoxicological effects of PCDDs, PCDFs and related compounds. Organohalogen Compounds. 12. 163–170.
46. Ball M (1990) Polychlordibenzodioxine and Polychlordibenzofurane in Zigarettenrauch. Beitrog Tabakforschung International.14, 393–402 (1990).
47. Azubuike C.C, Chikere C.B (2016) Bioremediation techniques-classification based on site of application. World Journal of Microbiology & Biotechnology. 32(11),180.
48. Abatenh E, Gizaw B, Tsegaye Z (2017) Application of microorganisms in bioremediation-review. Journal of Environmental Microbiology December.1(1):02-09.

49. Lui Ang E, Zhao H, Obbard J (2005) Recent Advances in the Bioremediation of Persistent Organic Pollutants Via Biomolecular Engineering. Enzyme and Microbial Technology. 32(5), 487-496.
50. Pariatamby, A. Ling Kee Y (2016) Persistent organic pollutants management and remediation. The Tenth International Conference on Waste Management and Technology. 842-848.
51. Litter M.I, Candal R.J, Meichtry M (2013) Advanced Oxidation Technologies-Sustainable Solutions for Environmental Treatments. Sustainable Energy Developments. 9,54-78.
52. Miklos D.B, Remy C, Jekel M, Linden K.G, Drewes J.E (2008) Evaluation of advanced oxidation processes for water and wastewater treatment. Water Research. 118-138.
53. Mehmet A. Oturan & Jean-Jacques Aaron (2014) Advanced OxidationProcesses in Water/Wastewater Treatment: Principles and Applications. A Review,Critical Reviews in Environmental Science and Technology. 44(23), 247-261.
54. Atalay S, Ersoz G (2016) Novel Catalyst in Advanced Oxidation of Organic Pollutants. Green Chemistry for Sustainability. 43-69.
55. Castellote M, Bengtsson N (2011) Principles of TiO_2 Photocatalysis. Available from DOI:10.1007/978-94-007-1297-3_2
56. Pichat P (2013) Photocatalysis and Water Purification. Fundamentals to Recent Applications. Available from ISBN : 978-3-527-64542-8.
57. Ameta R, Ameta S.C (2017) Photocatalysis principles and applications Available from Book Number-13: 978-1-4822-5493-8.
58. Bignozzi C.A (2011) Photocatalysis. Topics in Current Chemistry.303, 17-54.
59. Oyama S.T (2008) Mechanism in Homogeneous and Heterogeneous Epoxidation Catalysis. 1, 104-110.
60. Pelizzetti E, Serpone (1985) Homogeneous and Heterogeneous Photocatalysis.Mathematical and Physical Sciences. 174, 453-534.
61. Rajendra C, Sungyong Lee P, Sungyong Lee C (2015) Heterogeneous Nanocomposite-Photocatalysis for Water Purification. Available from ISBN: 978-0-323-39310-26.
62. Ibhadon A.O, Fitzpatrick P (2013) Heterogeneous Photocatalysis: Recent Advanced and Applications.Catalysts.3, 189-218.

63. Hermann (1999) Heterogeneous Photocatalysis: Fundamentals and Applications to the removal of various types of aqueous pollutants. Catalysts.53, 115-129.
64. Fox M.A, Dulay M.T (1993) Heterogeneous Photocatalysis. Chemistry Revision.93, 341-357.
65. Kim S, Park H, Choi W (2004)Comparative Study of Homogeneous and Heterogeneous Photocatalytic Redox Reactions. Journal of Physical Chemistry. 108, 6402-6411.
66. Hajjaji A, Amlouk M, Gaidi M, Bessais B, El Khakani M.A (2015) Chromium Doped TiO_2 Sputtered Thin Films Synthesis, Physical Investigations and Applications. Available from DOI 10.1007/978-3-319-13353-9.
67. Li X, Yu J, Wageh S, Al-Ghamdi A.A, Xie J (2016) Graphene in Photocatalysis. Available from DOI: 10.1002/smll.201600382.
68. Georgakilas, V (2014) Functionalization of Graphene. Available from ISBN : 978-3-527-67278-3.
69. Choi W, Lee Jo-won (2011) Graphene Synthesis and Applications. Nanomaterials and Their Applications. Available from ISBN-13: 978-1-4398-6188-2.
70. Enoki T, Ando T (2014) Physics and Chemistry of Graphene. Graphene to Nanographene. Available from ISBN-13: 978-981-4241-49-6.
71. Morales-Torres S, Pastrana-Martinez L.M (2012) Design of graphene-based TiO_2 photocatalyst. Environmental Science Pollution Research.19,3676-3687.
72. Khataee A, Mansoori G,A.(2012) Nanostructured Titanium Dioxide Materials: Properties , Preparation and Application. Available from ISBN-13 978-4374-72-9.
73. Khataee A.R, Kasiri Masound B (2010) Photocatalytic degradation of organic dyes in the presence of nanostructured titanium dioxide: Influence of the chemical structure of dyes. Jounrnals of Molecular Catalysis. 328(1-2), 342-421.
74. Prasai B, Cai B, Underwood J.K, Lewis J, Drabold D.A (2012) Properties of amorphous and crystalline titanium dioxide from first principles. Journal of Material Science. Available from DOI 10.1007/s10853-012-6439-6.
75. Cheng Z, Yao F, Yuan-wang L, Hui-qing C, Zhaon-jun L, Jain-ming X (2017) Uptake and translocation of organic pollutants in plants. Journal of Integrative Agriculture, 16(8), 1659-1668.

76. Rodrigues C.P, Ziolli R.L, Guimaraes J.R (2007) Inactivation of Escherichia coli in water by TiO_2-assisted disinfection using solar light. Journal of the Brazillian Chemical Society. 18(1).,353-365.
77. Huang Y, Chen D, Hu X, Qian Y (2018) Preparation of TiO_2/Carbon Nanotubes/Reduced Graphene Oxide Composites with Enhanced Photocatalytic Activity for the Degradation of Rhodamine B. Nanomaterials. 8(6), 431.
78. Jafari T, Moharreri E, Amin A.S, Miao R, Song W, Suib S.L (2016) Photocatalytic Water Splitting—The Untamed Dream: A Review of Recent Advances. Molecules. 21(7),900.
79. Bozzola J.J, Russel L.D (1992)Electron Microspopy: Principles and Techniques for Biologists. 148-202. Available from ISBN 0-7637-0192-0.
80. Yarwood J, Douthwaite R (2010)Spectroscopic Properties of Inorganic and Organometallic Compounds. 41,22-71.
81. Kumar C.S.S.S.R (2013) UV-VIS and Photoluminescence Spectroscopy for Nanomaterials Characterization. Available from ISBN 978-3-642-27593-7.
82. Magini M, Licheri G, Pashchina G, Piccaluga G, Pinna G (2018) X-Ray Diffraction of Ions in Aqueous Solutions: Hydration and Complex Formation. Available from ISBN 9781315898674.
83. Sasic S (2008)Pharmaceutical Applications of Raman Spectroscopy.Technology for the Pharmaceutical Industry. Available from ISBN 978-0-8138-1013-3.
84. Nicholson R.S (1965) Theory and Application of Cyclic Voltammetry for Measurement of Electrode Reaction Kinetics. 37(11). Available from https://pubs.acs.org/doi/pdf/10.1021/ac60230a016.
85. Orazem M.E, Tribollet B (2017) Electrochemical Impedance Spectroscopy. The Electrochemical Society. 2,80-94.
86. Sun W, Chenthamarakshan C.R, Rajeshwar K (2002) Chronopotentiometry of Titania Film Electrodes in Aqueous Media. Journal of Physical Chemistry. 11531-11538.
87. Park S, An J, Potts J.R, Velamakanni A, Murali S, Ruoff R.S (2011) Hydrazine-reduction of graphite- and graphene oxide.Carbon 49, 3019-3023

88. Rajeshwar K, Osugi M.E, Chanmanee W, Chenthamarakshan C.R, Zanoni M.V.B (2008) Heterogeneous photocatalytic treatment of organic dyes in air and aqueous media. Journal of Photochemistry and Photobiology C: Photochemistry Reviews. 9, 171-192.
89. Pariatamby A, Kee Y.L (2016) Persistent organic pollutants management and remediation. Procedia Environmental Sciences.31, 842-848.